UNIVERSIDADE
BEIRA INTERIOR

Modeling the Envelope Curves of Reinforced Concrete Membrane Elements under Cyclic Shear

Saffana Sadieh

Dissertação para obtenção do Grau de Mestre em

Engenharia Civil: Estruturas e Construção

(Mestrado integrado)

Orientador: Prof. Doutor Luís Filipe Almeida Bernardo

junho de 2023

Declaração de Integridade

Eu, Saffana Sadieh, que abaixo assino, estudante com o número de inscrição 36697 do Mestrado Integrado em Engenharia Civil da Faculdade das Engenharias, declaro ter desenvolvido o presente trabalho e elaborado o presente texto em total consonância com o **Código de Integridades da Universidade da Beira Interior**.

Mais concretamente afirmo não ter incorrido em qualquer das variedades de Fraude Académica, e que aqui declaro conhecer, que em particular atendi à exigida referenciação de frases, extratos, imagens e outras formas de trabalho intelectual, e assumindo assim na íntegra as responsabilidades da autoria.

Universidade da Beira Interior, Covilhã 09 /06/2023

Dedication

To my parents,

To my aunt, brothers, and sisters,

To my family and friends

To the Global platform of Syrian students.

Acknowledgments

This dissertation represents the culmination of several years of dedicated effort and numerous challenges, which would not have been accomplished without the continuous assistance and support that I have been privileged to receive.

Firstly, I would like to express my deepest gratitude to my supervisor, Professor Dr. Luís Filipe Almeida Bernardo, for his unwavering support, guidance, and invaluable advice, without which this dissertation would not have been possible. His expertise and insights have been instrumental in shaping my research and refining my approach. I am also thankful for his patience and encouragement during times of doubt and difficulty.

I would also like to extend my great appreciation to all my professors and to UBI for receiving me very well. Moreover, I would like to thank my friends who were like a second family to me, and made this journey possible with their great support in my difficult moments. I will be grateful forever for your love.

Most importantly, I would like to express my sincere gratitude to the Global Platform for Syrian Students, its founder His Excellency Dr Jorge Sampaio (peace be upon him), and his former diplomatic adviser, Dr. Helena Barroco. In addition to the new board of directors of the platform for the generous opportunity they have given me to pursue my studies in Portugal. Without their immense support, my educational endeavors would not have been attainable.

Finally, I must express my profound gratitude to my family for providing me with unfailing support and continuous encouragement throughout my years of study and through the process of researching and writing this thesis. This accomplishment would not have been possible without them.

Resumo

As paredes de corte e as estruturas de betão armado do tipo casca podem ser vistas como uma combinação de elementos de membrana bidimensionais mais pequenos, ou painéis. É possível prever o comportamento global das referidas estruturas sob cargas cíclicas através da previsão do comportamento individual dos elementos de membrana (elementos de painéis).

Para prever a resposta completa de elementos de painéis de betão estrutural sob estados planos de tensão monotónicos, foi proposto em estudos anteriores um modelo de treliça com amolecimento baseado numa versão modificada do modelo de treliça com amolecimento e com ângulo rotativo (RA-STM: *rotating-angle softened truss model*). Conhecido como o "procedimento RA-STM eficiente", este modelo foi validado com base em resultados experimentais envolvendo vários tipos de painéis de betão armado e pré-esforçado, tendo-se provado que proporciona uma elevada eficiência e estabilidade numérica.

O modelo incorpora equações de equilíbrio e de compatibilidade, para além de leis constitutivas médias para os materiais. As equações foram implementadas com um algoritmo eficiente para o procedimento de cálculo e para calcular os pontos solução sem utilizar a técnica clássica de tentativa e erro. Neste estudo, o procedimento RA-STM eficiente é revisto e as suas previsões são comparadas com um estudo experimental encontrado na literatura. O estudo envolve um conjunto de painéis de betão armado ensaiados sob corte cíclico até à rotura.

As previsões do modelo são comparadas com as envolventes das curvas experimentais tensão de corte-distorção relativas aos *loops* histeréticos. Foi demonstrado que as previsões para a forma das curvas envolventes (pelo menos até ser atingido o pico de carga) e para as tensões de corte características consideradas importantes (nomeadamente, tensões de corte de fendilhação, de cedência e máxima) estão em concordância razoável com as envolventes experimentais.

Com base nestes resultados, pode concluir-se que o procedimento RA-STM eficiente pode ser considerado um modelo adequado e fiável para prever uma série de características significativas da resposta de painéis em betão armado sob corte cíclico, pelo menos até ser atingido o pico de carga, e pode ser utilizado para pré-dimensionamento ou para análises preliminares de verificação.

Palavra-chavas:

Betão armado; elemento de painel; Rotating angle-softened truss model (RA-STM); procedimento de solução eficiente; corte monotónico; corte cíclico; tensão de corte; distorção; envolvente

Abstract

Shear walls and shell type reinforced concrete structures can be viewed as a combination of smaller two-dimensional membrane elements, or panels. It is possible to predict the global behavior of the referred structures under cyclic loadings by predicting the individual behavior of the membrane elements (panel elements).

To predict the full response of structural concrete panel elements under in-plane monotonic stresses, a smeared truss model based on a modified version of the rotating-angle softened truss model (RA-STM) was proposed in earlier studies. Known as the "efficient RA-STM procedure", this model was validated against experimental results of various types of reinforced and prestressed concrete panels, and was proven to provide high numerical efficiency and stability.

The model incorporates equilibrium and compatibility equations, in addition to smeared constitutive laws for the materials. The equations were implemented with an efficient algorithm to carry out the calculation procedure, and compute the solution points without using the classical trial-and-error technique. In this study, the effective RA-STM procedure is revised, and its predictions are compared to an experimental study found in literature. The study involves a set of reinforced concrete panels tested under in-plane cyclic shear until failure.

The predictions from the model are compared against the experimental envelope curves of the hysteretic shear stress-shear strain loops. It was shown that the predictions for the shape of envelope curves (at least until the peak load is reached), and for the important key shear stresses (namely, cracking, yielding, and maximum shear stresses) are in a reasonably good agreement with the experimental envelopes.

Based on these results, it can be concluded that the efficient RA-STM procedure can be considered a good and reliable model to predict a number of significant characteristics of the response of reinforced concrete panels under cyclic shear, at least up until the peak load Is reached, and can be used for predesigning or precheck analysis.

Keywords

Reinforced concrete; panel element; Rotating angle-softened truss model (RA-STM); efficient solution procedure; monotonic shear; cyclic shear; shear stress; shear strain; envelope curve.

Index

List of Figures

List of Tables

List of Acronyms

cv	Coefficient of variation
Ec	Young's modulus for concrete
E_s	Young's modulus for steel
f	Normal stress in steel reinforcement
f'_c	uniaxial compressive strength of concrete
f_{cr}	Tensile strength of concrete
f_L	Tensile stress in the longitudinal reinforcement
f_{Ly}	Uniaxial yielding stress of the longitudinal reinforcement
f_S	Average tensile stress in the steel bars
f_{Sy}	Uniaxial yielding stress for steel
f_T	Tensile stress in the transverse reinforcement
f_{Ty}	Uniaxial yielding stress of the transverse reinforcement
k	Index of the step
D	Damage coefficient
ψ	Damage parameter
m_L	Longitudinal proportionality coefficient
m_{LT}	Shear proportionality coefficient
m_T	Transverse proportionality coefficient
η	Ratio of the transverse to the longitudinal tensile strength
$RF^{(1)}{}_{RA-STM}$	First residual function for the efficient RA-STM procedure
$RF^{(2)}{}_{RA-STM}$	Second residual function for the efficient RA-STM procedure
RF_{START}	Residual function for the initial estimates
s	Standard deviation
$\bar{x}$	Mean
α_D	Angle of the principal compressive stress in the concrete membrane element

$\Delta\varepsilon_D$	Path increment for ε_D
ε	Strain
ε_0	Strain corresponding to the concrete compressive peak stress
ε_{cr}	Strain corresponding to the tensile strength of concrete
ε_{cu}	Ultimate strain for concrete in compression
ε_D	Principal average compressive strain
ε_L	Longitudinal average strain
ε_{Ly}	Yielding strain for the longitudinal reinforcement
ε_R	Principal average tensile strain
ε_S	Average strain in the steel bars
ε_{Sy}	Yielding strain for steel
ε_T	Transverse average strain
ε_{Ty}	Yielding strain for the transverse reinforcement
γ	Shear strain
γ_{LT}	Average shear strain in the L-T coordinate system
γ_y	Yielding shear strain
$\gamma_{y,exp}$	Experimental yielding shear strain
$\gamma_{y,th}$	Theoretical yielding shear strain
γ_u	Ultimate shear strain
$\gamma_{u,exp}$	Experimental ultimate shear strain
$\gamma_{u,th}$	Theoretical ultimate shear strain
ζ	Softening coefficient
ρ_L	Longitudinal reinforcement ratio
ρ_T	Transverse reinforcement ratio
σ	Stress
σ_1	Principal tensile stress in the RC membrane element
σ_2	Principal compressive stress in the RC membrane element
σ_D	Principal compressive stress in the concrete membrane element

σ_L	Longitudinal normal stress in the RC membrane element
σ_L^c	Longitudinal normal stress in the concrete membrane element
σ_R	Principal tensile stress in the concrete membrane element
σ_T	Transverse normal stress in the RC membrane element
σ_T^c	Transverse normal stress in the concrete membrane element
τ_{cr}	Cracking shear stress
$\tau_{cr,exp}$	Experimental cracking shear stress
$\tau_{cr,th}$	Theoretical cracking shear stress
τ_{LT}	shear stress in the RC membrane element in the L-T coordinate system
${\tau_{LT}}^c$	Shear stress in the concrete membrane element in the L-T coordinate system
τ_{max}	Peak shear stress
$\tau_{max,exp}$	Experimental shear stress
$\tau_{max,th}$	Theoretical shear stress

1 Introduction

1.1 Research Significance and Problem Definition

Reinforced concrete (RC) structures, including walls, panels, and shells, such as containers or curved shell roofs, are widely used in construction projects worldwide. For various reasons and advantages, they allow to construct more complex units, give freedom in design while maintaining the safety.

For instance, shear walls provide strength and rigidity, minimize earthquake damage. Shell roofs have high stiffness, more strength when compared to other types of structures, and can cover very large areas.

A logical way to analyze these structures is to consider them as the combination of small, two-dimensional (2D) RC membrane or panel elements that are subjected to in-plane stresses.

Since the stress field is considered uniformly zero in the perpendicular direction of the middle plane for these elements, the material is described as being under plane stress.

Subsequently, simplified models can be developed to study these RC panel elements before integrating them into more general models [1].

Simplified bidimensional RC models, in particular, offer several benefits in the analysis and design of concrete structures. They reduce the computational resources required in comparison to more complex models. Moreover, simplified models are useful in providing preliminary design information for the early stages of a project, where a more in-depth analysis may not yet be required.

In the past thirty years, multiple models have been created to investigate RC panel elements using the smeared-crack concept. These models take the form of plain stress field, or plain truss, approaches and have demonstrated ample reliability and ease of implementation for computer-based analyses. These models are introduced in the upcoming subsection 1.2.

While certain cyclic smeared truss models such as the Cyclic Softened Membrane Model (CSMM) and Fixed Strut Angle Model (FSAM) (subsection 1.2) have been demonstrated to accurately predict the global hysteretic response of RC panels subjected to cyclic shear (references [2] [3]), their implementation can be challenging due to the use of smeared cyclic constitutive laws for the materials. Such laws have a complex development to account for the possibility of several loading–unloading cycles at different points and, also, for the damage of concrete during the loading history.

Therefore, there is a need for a simple model that can be easily implemented and can accurately predict the behavior of RC panel elements subjected to cyclic shear.

It is recognized that computing the envelope of the hysteretic behavioral curves, for the shear stress (τ) and shear strain (γ), such as for the $\tau - \gamma$ loops of the RC panels under cyclic shear, is typically adequate for a precheck study or a predesign.

Previous research has demonstrated that, for this purpose, a monotonic smeared truss model can reasonably capture the key characteristics of such envelope curves, at least up to the peak load. This is also true for other referenced monotonic models, such as the rotating angle softened truss model (RA-STM), the fixed angle softened truss model (FA-STM), and the softened membrane model (SMM).

1.1.1 Objective of dissertation

The latest version of the RA-STM, referred to as the "efficient RA-STM procedure," has been demonstrated to be highly stable and numerically efficient. Furthermore, it has proven to be a reliable tool for predicting the complete response of RC panels under monotonic shear [4].

Additional information about these models can be found in the forthcoming chapter.

To date, there has been very little comprehensive study of the applicability of a simpler monotonic smeared truss model for predicting the primary characteristics of RC panels' response under cyclic shear.

Therefore, in this study, the monotonic efficient RA-STM procedure validated for RC panels under monotonic shear, is used to predict the envelope $\tau - \gamma$ curves of RC panels under cyclic shear.

This study aims to examine the possibility of using a simpler monotonic smeared truss model to predict the behavior, key features, and characteristics of the envelope $\tau - \gamma$ curves of RC panels subjected to cyclic shear. Among the various models that use the monotonic smeared concept, the RA-STM has shown to demonstrate one of the simplest calculation procedure.

These attributes of the model support its continued application as a foundational model, including its extension to examine structural elements other than RC panels.

Additionally, the RA-STM has been expanded and improved over the past few years in order to deliver more accurate predictions, as well as improve the effectiveness and stability of the numerical calculation process.

Therefore, in this study, the monotonic efficient RA-STM procedure validated for RC panels under monotonic shear, is used to predict the envelope $\tau - \gamma$ curves of RC panels under cyclic shear.

1.1.2 Followed Procedure

In order to accomplish the aim of this study, the subsequent steps were followed:

- The monotonic efficient RA-STM procedure was revised to account for the cyclic attribute of the load, in order to predict the envelope response of RC panels under cyclic shear. This was done by incorporating a damage coefficient to the smeared constitutive law;
- The model was then used to predict the envelope response of some RC panels that were subjected to proportional cyclic shear using the Universal Panel Tester at the University of Houston;
- To validate the model, a comparison was made between the predictions from the monotonic efficient RA-STM procedure and the experimental envelop curves and key points for the tested RC panels.

1.1.3 Outline of dissertation

This dissertation is divided into 4 chapters, a brief description of each chapter is presented below:

Chapter 1 provides an introduction of the research, highlights the objectives, and summarizes the evolution of the most relevant shear models for RC plate members with interest for this work.

Chapter 2 presents an overview, the equations, calculation procedure and algorithm of the efficient RA-STM, which is the model used in this work.

Chapter 3 presents a summary of a previous experimental study involving RC panels under cyclic in-plane loading. It describes the test specimens and presents the main results. It also presents the predictions from the efficient RA-STM, and compares the experimental with the theoretical results.

Chapter 4 states the conclusion of the research and gives recommendations for future studies.

1.2 Literature research

This section provides an overview of the evolution of shear theories for RC members, and summarizes the existing models for shear:

Ritter in 1899 and Morsch in 1902 [5] developed a truss model over a century ago to simulate the post-cracking behavior of reinforced concrete members subjected to shear and bending.

The model assumed that under shear and bending, the concrete in a RC member would develop diagonal cracks, effectively dividing the concrete into a series of concrete struts.

The RC beams' shear resistance was assumed to be achieved through an internal truss mechanism that consisted of two longitudinal parallel chords connected to a composite web made of web steel bars and diagonal concrete struts.

The diagonal concrete struts were considered to experience direct axial compression, whereas the web steel bars were modeled as the tensile web members of the truss, in order to provide the shear resistance of the RC beams.

The model was referred to as the "45-degree truss model" since the cracks were assumed to be inclined at 45 degrees with respect to the longitudinal reinforcement.

In 1968, Robinson and Demorieux [5] observed that when a RC element is under shear stress, it experiences biaxial compression-tension stresses in the 45-degree direction.

By considering the shear action as a two-dimensional problem, they found that the tension in the perpendicular direction caused cracking, which reduced the compressive strength in the other direction.

By taking into account this softening effect of concrete struts on the webs of eight tested I-section beams, they were able to provide an explanation for the stress equilibrium in the webs based on the truss model.

Although, they could explain the reduction of strength in the concrete struts, they were unable to measure or quantify this reduction.

In 1981 Vecchio and Collins [6], Vecchio and Collins constructed a "shear rig" to measure a softening coefficient for the compressive stress-strain curve of concrete under biaxial compression-tension stresses. They then developed the Compression Field Theory (CFT), which could be used throughout the post-cracking range up to the ultimate state.

The CFT made the assumption that the orientation of the principal compressive stress in concrete is the same as the orientation of the principal compressive strain, and that cracks developed along the principal direction of concrete stress, which is known as the rotating-crack model.

The CFT was a significant advancement in predicting the shear behavior of RC elements as it fulfilled the three fundamental principles of mechanics of materials (stress equilibrium, strain compatibility and constitutive laws).

However, the theory had a limitation in that it assumed that concrete did not bear any tensile stress once it had undergone cracking.

Later on, this assumption has been refuted by many tests, which have shown that concrete tensile stresses can significantly enhance the stiffness of cracked reinforced concrete structures.

Vecchio and Collins in 1986 [7], extended the CFT by considering the tensile strength of concrete, resulting in the Modified Compression Field Theory (MCFT). This theory was developed to predict the post-cracking stiffness.

The MCFT showed to have two notable deficiencies. Firstly, it violated a fundamental principle of mechanics by imposing concrete shear stresses in the principal directions. Secondly, it relied on the local stress-strain curve of the steel bars that were embedded in concrete, instead of using smeared (average) stress-strain curves to account for the tensile concrete between cracks (stiffening effect).

Balakrishnan and Murray in 1988 [8], employed their own constitutive relationships to apply a rotating crack model for predicting the monotonic behavior of shear panels and deep beams. At the beginning of concrete cracking, the Poisson's ratio was set as zero. The model was utilized to predict the behavior of several RC panels that were tested by Vecchio and Collins [9].

Crisfield and Wills in 1989 [10], conducted an analysis on various RC panels that were tested by Vecchio and Collins [9] - [11], using different material models. These models included the following ones:

- In the fixed crack model, the directions of orthogonal cracks were governed by the direction of the first principal stress that exceeded the tensile stress of the uncracked concrete;
- The swing-crack model was a rotating crack model;
- The plasticity model incorporated a square yield surface in compression in which no tension was allowed.

The authors carried out comprehensive investigations on the three suggested models on the panels and compared the analytical results with the experimental results [12]. Additionally, they demonstrated the differences between the fixed crack and the rotating crack models.

Later at the University of Houston, **Belarbi and Hsu, 1994 and 1995; Pang and Hsu, 1995** [13]–[15], Hsu and collaborators developed the Rotating-Angle Softened Truss Model (RA-STM) which is capable of treating cracked RC as a consistent smeared material. The model proposed a new average stress-strain curve for steel bars that are embedded in concrete. This curve was smeared, meaning that it represents an average over a range of possible stress-strain values.

Furthermore, a new algorithm was created to enhance the iteration process for resolving the equilibrium, compatibility, and constitutive equations. This new algorithm led to a significant improvement in the efficiency of the solution procedure.

The model has two distinct advantages. Firstly, it generates a unique solution, unlike the modified compression field theory that produces multiple solutions. Secondly, it eliminates the requirement for a "crack check," which is challenging to execute with finite element methods.

These studies revealed that theories based on rotating-angle are unable to logically generate the "concrete contribution" due to the absence of shear stresses along the rotating-angle cracks.

In the following years, **Pang and Hsu in 1996; Hsu and Zhang in 1997; Zhang and Hsu in 1998** [16]–[18], in an attempt to predict the "concrete contribution", Hsu and collaborators proposed the Fixed-Angle Softened Truss Model (FA-STM). This model assumes that the direction of cracks is perpendicular to the principal tensile stresses at the point of initial cracking, rather than following the rotating cracks.

The constitutive laws of concrete were established based on the principal coordinate of the applied stresses at initial cracking. The primary limitation of the FA-STM is its complexity compared to the RA-STM due to the intricate stress-strain relationship of concrete in shear.

Ayoub and Fillippou in 1998 [19], introduced a rotating crack model in 1998, which extended the orthotropic models proposed by Vecchio in 1990 [20], and Balakrishnan and Murray in 1988 [8].

The panels tested by Vecchio and Collins in 1982 [9] were used in correlation studies. The results of the analytical and experimental investigations demonstrated a reasonable level of agreement.

In 1998 Kaufmann and Marti [21] introduced the Cracked Membrane Model (CMM), which incorporated a concrete tension stiffening model along with the CFT proposed by Vecchio and Collins [6].

A stepped, rigid-perfectly plastic bond slip relationship between the cracks of concrete and steel was used to model the tension stiffening of concrete while ensuring equilibrium at the crack faces.

Foster and Marti in 2003 [22], integrated the Cracked Membrane Model (CMM) into a finite element formulation and assessed its accuracy by comparing its predictions with the experimental data obtained from the shear panel tests conducted by Meyboom and Zhang.

Based on the rotating crack model, **Vecchio in 2000** [23] **and 2001** [24], developed and implemented the Disturbed Stress Field Model (DSFM).

The DSFM was a partially smeared model that incorporated shear slips along crack surfaces and required a "crack check" similar to the modified compression field theory (MCFT).

Compared to the MCFT (Vecchio and Collins [7]), the DSFM was more complex.

DSFM's predictions were compared to the experimental results of their panels, as well as to the analytical results obtained by MCFT. The predictions obtained from the DSFM and MCFT were mostly similar.

Belletti et al in 2001 [25], proposed a fixed crack model that adopts the stress-strain relationships of concrete and steel, incorporates aggregate interlock and the dowel action.

The model adopted the softening coefficient (ζ), proposed by Pang and Hsu [13], which accounted for the softening effect of tensile strains on the perpendicular compression behavior of concrete.

An analysis was conducted on the panels that were tested at the University of Toronto (Vecchio and Collins [9] and [7]) and the panels tested at the University of Houston (Belarbi and Hsu [14]; Pang and Hsu [13] and [17]).

The test results were found to be in good agreement with the predictions of the proposed model.

Despite being able to predict the pre-peak behavior of shear elements, none of the rational models mentioned above could accurately account for the presence of the post-peak load-deformation curves.

Therefore, **Hsu and Zhu in 2002** [26] developed the softened membrane model (SMM) in 2002 to predict the complete monotonic shear stress-strain curves of RC panels, including the descending branches.

SMM's ability to predict the descending branches was achieved by considering the Poisson effect, which accounts for the mutual influence of the two normal strains in cracked RC.

Two Hsu/Zhu ratios were used to characterize the Poisson effect of cracked RC, allowing the SMM to predict the descending branches. Furthermore, a basic stress-strain equation for concrete in shear was derived through the use of equilibrium and compatibility equations and incorporated into the model by Zhu, Hsu, and Lee in 2001 [27].

The introduction of this new shear modulus led to a significant simplification of the solution algorithm of fixed model theories, such as SMM and FA-STM. It also increased the accuracy of these models.

So far, the SMM has demonstrated its capability to accurately predict the complete behavior of RC panels subjected to monotonic pure shear.

Later **in 2005 Mansour and Hsu** [3], [28] proposed a cyclic softened membrane model (CSMM) for predicting the load-deformation behavior of reinforced concrete (RC) membrane elements under reversed cyclic shear stresses, with the goal of designing RC structures in earthquake regions. This model presented an extension of the SMM, which was originally developed for monotonic shear behavior. Both models satisfy Navier's principles of mechanics of materials (stress equilibrium, strain compatibility, and constitutive laws of materials). Developing CSMM required three new components of material laws: (1) stress-strain relationships for concrete and steel in the unloading and reloading regions, (2) modifications of the envelope curve for compressive concrete, and (3) the Hsu/Zhu ratios for cyclic loading.

Mansur and Hsu conducted a comparison between the predictions of CSMM and actual test results in order to validate the theoretical model. After comparing the predictions of the CSMM

with actual test results, Mansur and Hsu concluded that the model is capable of predicting the hysteretic loops and their pinched shapes. Furthermore, they found that the "pinching effect" was caused by the deviation of the steel bar direction from that of the principal stresses. They provided a logical explanation for the "pinching mechanism" and the "failure mechanism" using Mohr's circles of stresses and strains.

Orakcal, Massone, and Ulugtekin[2] proposed the "Fixed Strut Angle Model" (FSAM) as a simple and efficient constitutive model to simulate the nonlinear axial/shear behavior of RC membrane (panel) elements under reversed and generalized cyclic loading conditions.

The FSAM formulation calculates normal stresses in cracked concrete along fixed directions of cracks or struts.

The total stress field in concrete in the FSAM is obtained by superimposing the concrete stresses along the struts, with the shear stresses developed along crack surfaces using a friction-based constitutive relationship.

The performance of the model was evaluated by comparing its predictions with experimental results. The results indicated that the model was able to reasonably replicate the overall response characteristics of the panels, including hysteretic shear stress vs. strain behavior, shear stress capacity, hysteretic shear stiffness attributes, ductility, pinching behavior, governing failure mode, principal strain and stress directions, and local deformations.

2 Efficient RA-STM Procedure

In the last decades, truss models have been proven to well predict the behavior of RC structures, namely after concrete cracking. Among the many previously mentioned models in Chapter 1, the efficient RA-STM model for RC panels under monotonic shear has been widely used [4], [29].

The reason behind choosing this particular model for this study is that it constitutes somewhat a simpler analytical model to implement in the computer when compared to other models like FA-STM or SMM. In spite of its simplicity, this model was also proven to be a very reliable model for monotonic shear.

As briefly mentioned, the STM model was developed and modified, and renamed as the RA-STM to account for the rotation of the principal compressive stresses in the concrete member. This rotation occurs as a result of the internal redistribution of stresses and compatibility conditions after cracking.

This section presents a summary of the fundamental equations and derivations, further details about the hypothesis, and the numerical solution procedure. More details about the description of the efficient numerical calculation procedure to compute the solution points can be found in the literature [30], [31], [32].

Since the monotonic nature of this model is preserved for the objectives of this study, no changes were made to the equations and numerical solution procedure. However, as the model is used for cyclic shear in this study, a new damage factor is introduced in the smeared constitutive law for concrete in compression. The relevance of implementing this parameter is discussed later in chapter 3.

2.1 Equilibrium Equations

Figure 1 represents a 2D membrane element subjected to in-plane normal stresses, in the longitudinal (σ_L) and transversal directions (σ_T), and shear stresses (τ_{LT}); the longitudinal and transversal reinforcement grid establish the L-T coordinate system.

The in-plane stresses (σ_L, σ_T and τ_{LT}) are divided into the following components: concrete stresses and steel stresses. (σ_L^c, σ_T^c and τ_{LT}^c)

The RC panel element can be viewed as the overlap or superposition of a concrete element with in-plane stresses (σ_L^c, σ_T^c and τ_{LT}^c), and a steel grid element (the reinforcement bars) with normal tensile stresses ($\rho_L f_L,\ \rho_T f_T$). The parameters ρ_L, and ρ_T, stand for the reinforcement ratio, where as f_L , f_T are the normal stresses in steel reinforcement for the longitudinal and transverse direction, respectively.

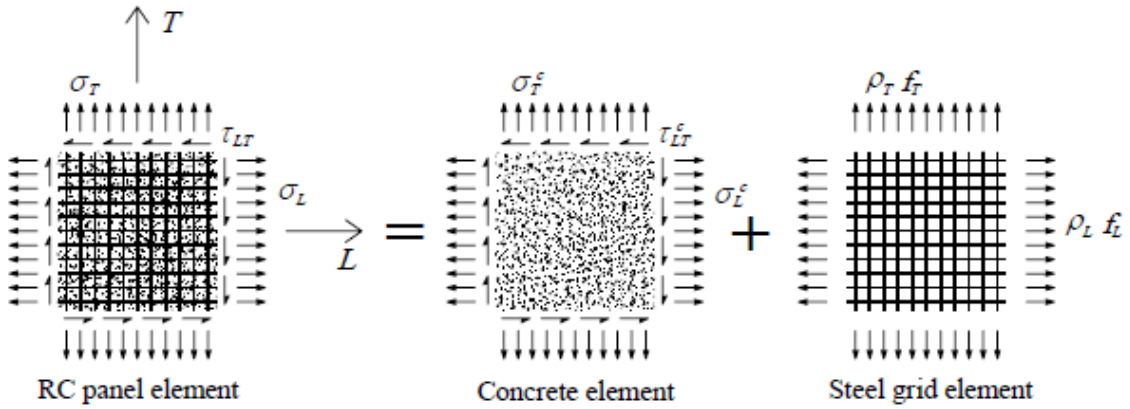

Figure 1. RC plate element under in-plane stresses

The dowel action in the steel bars is neglected for simplicity (the steel bars only withstand tensile forces) and perfect bond is assumed between concrete and steel [1].

From Figure 1 the following matrix equilibrium equation for stresses in the L-T reference frame can be stated:

$$\begin{bmatrix} \sigma_L \\ \sigma_T \\ \tau_{LT} \end{bmatrix} = \begin{bmatrix} \sigma_L^c \\ \sigma_T^c \\ \tau_{LT}^c \end{bmatrix} + \begin{bmatrix} \rho_L f_L \\ \rho_T f_T \\ 0 \end{bmatrix} \tag{1}$$

Figure 2 illustrates the principal stresses (σ_D and σ_R) and the variable angle α_D, which are used to compute the stress components in concrete.

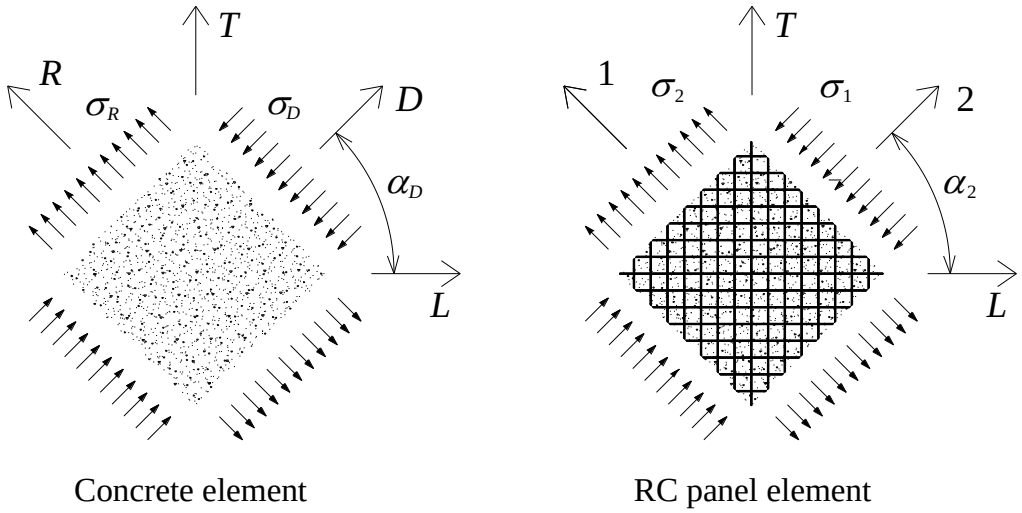

Figure 2. Principal directions and principal stresses.

The coordinate systems L-T and R-D are related through the angle α_R (see Figure 3), which coincides with the principal direction of stresses in concrete, it also varies as external stresses in the RC membrane element increase proportionally, hence why it is called the variable angle.

Figure 3 illustrates the coordinate system R-D (principal directions), in which the shear stress is considered null ($\tau_{RD} = 0$).

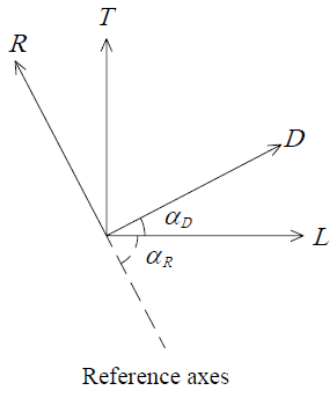

Figure 3. Reference axes and variable angle

It was assumed for the RA-STM that the crack direction of the RC membrane element is perpendicular to the principal direction of tensile stresses in concrete σ_R, and the complement of the variable angle, α_D (Figure 3), defines the direction of cracks. For this reason, in this study the equations will be written in terms of α_D, instead of α_R. To relate the stresses between the two-coordinate systems L-T and R-D, Mohr's circle for stresses was used and the following equation is introduced:

$$\begin{bmatrix} \sigma_L^c \\ \sigma_T^c \\ \tau_{LT}^c \end{bmatrix} = \begin{bmatrix} cos^2(\alpha_D) & sin^2(\alpha_D) & 2sin^2(\alpha_D)cos^2(\alpha_D) \\ sin^2(\alpha_D) & cos^2(\alpha_D) & -2sin^2(\alpha_D)cos^2(\alpha_D) \\ -\sin(\alpha_D)\cos(\alpha_D) & \sin(\alpha_D)\cos(\alpha_D) & cos^2(\alpha_D) - sin^2(\alpha_D) \end{bmatrix} \begin{bmatrix} \sigma_D \\ \sigma_R \\ 0 \end{bmatrix} \quad (2)$$

2.2 Equations from Compatibility Conditions

To obtain the compatibility equations, similarly to the method used for equilibrium equations, Mohr's circle was applied, except for strains instead of stresses, through the Eq.(3). the average strain components ($\varepsilon_L . \varepsilon_T$ and γ_{LT}) were related with the principal strains (ε_R and ε_D) and the variable angle α_D, between the coordinate systems L-T and R-D.

$$\begin{bmatrix} \varepsilon_L \\ \varepsilon_T \\ \gamma_{LT} \end{bmatrix} = \begin{bmatrix} cos^2(\alpha_D) & sin^2(\alpha_D) & 2\sin(\alpha_D)\cos(\alpha_D) \\ sin^2(\alpha_D) & cos^2(\alpha_D) & -2\sin(\alpha_D)\cos(\alpha_D) \\ -2\sin(\alpha_D)\cos(\alpha_D) & 2\sin(\alpha_D)\cos(\alpha_D) & 2cos^2(\alpha_D) - 2sin^2(\alpha_D) \end{bmatrix} \begin{bmatrix} \varepsilon_R \\ \varepsilon_R \\ 0 \end{bmatrix} \quad (3)$$

From Eq.(3) the following invariant equation was obtained, by adding, and then simplifying, the first two lines utilizing trigonometric identities. This equation will be used further in the solution procedure.

$$\varepsilon_R = \varepsilon_L + \varepsilon_T - \varepsilon_D \tag{4}$$

The third line of Eq.(3) can be simplified as follows:

$$\gamma_{LT} = 2(\varepsilon_R - \varepsilon_R)\sin(\alpha_D)\cos(\alpha_D) \tag{5}$$

2.3 Smeared Constitutive Laws

Based on the principle of mechanics, the stresses (σ) in equilibrium equations need to be related to the strains (ε) in the compatibility equations, through the constitutive laws of materials.

In this study three different $\sigma - \varepsilon$ relationships or smeared constitutive laws, were used- namely, concrete in compression, concrete in tension and embedded steel reinforcement in tension.

These laws are the same ones that have been applied and justified by an earlier research study for RC membrane elements under monotonic shear loading [30].

Although this research revolves around cyclic shear, the option of using the same referred laws can be considered valid due to a previous research by Mansour and Hsu in 2005 [3]. This study showed that, for concrete and steel specimens under uniaxial cyclic loading, the hysteretic loops of the $\sigma - \varepsilon$ curves generated an envelope curve almost identical to the curve produced under monotonic loading.

Hence, these laws can apply as the objective of this study is to compute the envelope $\tau - \gamma$ curves of RC panels under cyclic shear.

The same observation has been concluded by other researchers, such as Mansour et al. in 2001 [33]. The authors compared the experimental envelope curves for cyclic loading with the monotonic curves by Belarbi and Hsu in 1994 [15], and 1995 [14].

2.3.1 Concrete

2.3.1.1 Concrete in Compression

Belarbi and Hsu in 1995 developed a smeared softened $\sigma - \varepsilon$ relationship to model the behavior of concrete in compression in struts [14], and Eq.(6) to (10) were proposed (see also Figure 4)

When a RC panel is subjected to cyclic shear loading, important phenomenon should be taken into consideration in defining the constitutive relationships of concrete in compression.

As the concrete is subjected to compression, cracking is induced due to tension in the perpendicular direction, this results in concrete softening. Consequently, a softening coefficient ζ must be incorporated in the $\sigma - \varepsilon$ relationships.

Another coefficient to take into consideration, is the damage coefficient D, that is caused by the history of tensile and compressive stress reversal normal to compression direction being considered.

Eq.(7) represents the damage coefficient. While Eq.(8) gives the softening coefficient ζ, which was proposed by Zhang and Hsu in 1998 [18], and later refined by Zhu et al. in 2001 [27].

$$\begin{cases} \sigma_D = D\zeta f'_c \left[2\left(\frac{\varepsilon_D}{\zeta\varepsilon_0}\right) - \left(\frac{\varepsilon_D}{\zeta\varepsilon_0}\right)^2\right] & if\ \varepsilon_D \le \zeta\varepsilon_0 \\ \sigma_D = D\zeta f'_c \left[1 - \left(\frac{\left({}^{\varepsilon_D}/_{\zeta\varepsilon_0}\right) - 1}{\left({}^{4}/_{\zeta}\right) - 1}\right)^2\right] & if\ \varepsilon_D > \zeta\varepsilon_0 \end{cases} \quad (6)$$

$$D = 1 - \psi\frac{\varepsilon'_D}{\varepsilon_0} \le 1 \quad (7)$$

$$\zeta = \left(\frac{5.8}{\sqrt{f'_c(\mathrm{MPa})}} \le 0.9\right).\frac{1}{\sqrt{1 + \frac{400\varepsilon_R}{\eta'}}} \quad (8)$$

$$\eta = \frac{\rho_T f_{Ty} - \sigma_T}{\rho_l f_{Ly} - \sigma_L} \quad (9)$$

$$\begin{cases} \eta' = \eta & if\ \eta \le 1 \\ \eta' = {}^{1}/_{\eta} & if\ \eta > 1 \end{cases} \quad (10)$$

In the previous equations, the new parameters refer to the following:

- f'_c is the uniaxial cylinder compressive strength of concrete;
- ε_0 is the strain corresponding to the peak cylinder stress f'_c;
- η is the ratio of the transverse to the longitudinal tensile strength of steel reinforcement;

- f_{Ly} , f_{Ty} are the yielding stresses of the longitudinal, transverse reinforcement, respectively;

To calculate the damage coefficient D, Mansour and Hsu [3] introduced the damage parameter ψ as a constant (ψ=0.4), and defined ε'_c as the maximum compression strain normal to the compression direction under consideration and occurred in the previous loading cycles. Some considerations about the damage coefficient are stated in chapter3.

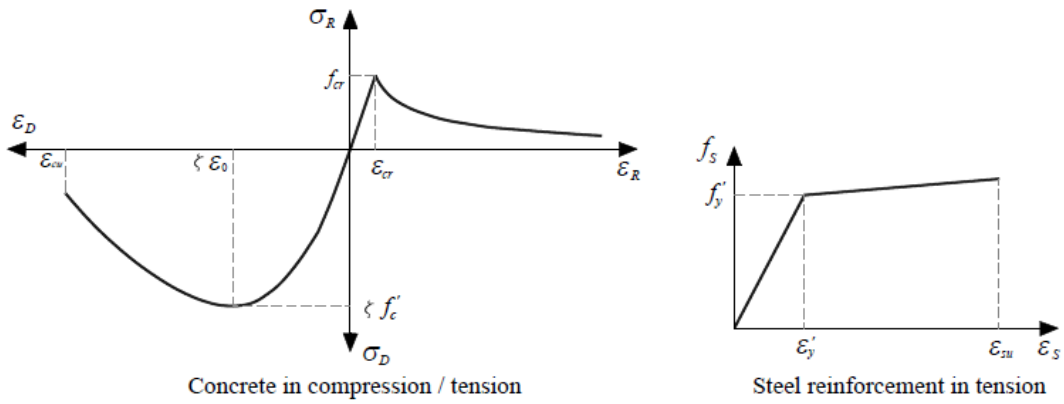

Figure 4. Smeared constitutive laws.

2.3.1.2 Concrete in Tension

To model the behavior of concrete in tension, an additional smeared constitutive law needs to be incorporated, to account for the tension in the perpendicular direction to the struts.

Similarly to concrete in compression, the smeared softened $\sigma - \varepsilon$ relationship proposed by Belarbi and Hsu in 1994 [15] was utilized in this research. (Eq.(11) to (13), see Figure 4)

$$\begin{cases} \sigma_R = E_c \varepsilon_R & if\ \varepsilon_R \le \varepsilon_{cr} \\ \sigma_R = f_{cr}\left(\dfrac{\varepsilon_{cr}}{\varepsilon_R}\right)^{0.4} & if\ \varepsilon_R > \varepsilon_{cr} \end{cases} \tag{11}$$

$$E_c = 3875\sqrt{f'_c(\text{MPa})} \tag{12}$$

$$f_{cr} = E_c \varepsilon_{cr} = 0.311\sqrt{f'_c(\text{MPa})} \tag{13}$$

In the previous equations, E_c refers to Young's modulus for concrete, and ε_{cr} is the tensile strain corresponding to the peak stress f_{cr} (concrete tensile strength).

From reference [15], ε_{cr} can be considered constant and equal to 0.00008.

2.3.2 Steel Reinforcement

As for steel bars embedded in concrete, a simplification of the nonlinear $\sigma - \tau$ stiffened relationship from Belarbi and Hsu in 1994 [15] was used. This simplification was proposed by Jeng and Hsu in 2009 [34] and the smeared and bilinear $\sigma - \tau$ stiffened relationship was introduced (Eq.(14), see Figure 4), to model the behavior of steel bars in tension embedded in concrete.

$$\begin{cases} f_S = E_S \varepsilon_S \quad if\ \varepsilon_S \leq \varepsilon'_y \\ f_S = (0.91 - 2BN) f_{Sy} + (0.02 + 0.25BN) E_S \varepsilon_S \quad if\ \varepsilon_S > \varepsilon'_y \end{cases} \tag{14}$$

$$\varepsilon'_y = \frac{f'_y}{E_S} \tag{15}$$

$$f'_y = (0.93 - 2BN) f_{Sy} \tag{16}$$

$$BN = \frac{1}{\rho_S} \left(\frac{f_{cr}}{f_{Sy}} \right)^{1.5} \tag{17}$$

The parameters in the previous equations are identified as: f_s and ε_s are the average tensile stress and strain in the steel reinforcement, E_s is Young's modulus for steel.

The subscript "S" must be replaced with "L" or "T" for the longitudinal and transverse steel reinforcement, respectively.

2.4 Efficient Solution Procedure

2.4.1 Equations for Proportional Loading

The loading condition of choice in this study was proportional loading, which is the most commonly used loading condition in practice and experiments for RC membrane elements under in-plane stresses. The proportional loading refers to the cases where the principal external stresses maintain constant directions and constant ratios of their values through all loading history.

The proportional loading condition is incorporated through the proportionality coefficients which remain constant, namely: longitudinal (m_L), transverse (m_T), and shear (m_{LT}). Those coefficients relate the applied (external) in-plane stresses in the L-T reference frame (σ_L, σ_T and τ_{LT}) to the applied principal tensile stress (σ_1) in the 1-2 reference frame (see Figure 2).

$$m_L = \frac{\sigma_L}{\sigma_1} \tag{18}$$

$$m_T = \frac{\sigma_T}{\sigma_1} \tag{19}$$

$$m_{LT} = \frac{\sigma_{LT}}{\sigma_1} \tag{20}$$

The stresses σ_L, σ_T and τ_{LT} from Eq. (18) to Eq.(20) are then substituted into Eq.(1) and Eq.(2). A quadratic equation (Eq.(21)) is stated after some algebraic manipulations and considering the applied principal tensile stress σ_1 in the RC panel element (see Figure 2) as the independent variable. Eq.(25) is the solution equation for σ_1 (more details about the mathematical manipulations can be found in reference[4]).

$$A'\sigma_1{}^2 - B'\sigma_1 + C'' = 0 \tag{21}$$

$$A' = m_L m_T - m_{LT}{}^2 \tag{22}$$

$$B' = m_L\left(\sigma_R + \rho_T f_T + \rho_{Tf} f_{Tf}\right) + m_T\left(\sigma_R + \rho_L f_L + \rho_{Lf} f_{Lf}\right) \tag{23}$$

$$C' = \left(\sigma_R + \rho_L f_L + \rho_{Lf} f_{Lf}\right)\left(\sigma_R + \rho_T f_T + \rho_{Tf} f_{Tf}\right) \tag{24}$$

$$\sigma_1 = \frac{B' \pm \sqrt{B'^2 - 4A'C'}}{2A'} \tag{25}$$

From Figure 2 and Mohr's circle for stresses, σ_1 can be related with the stresses in the $L-T$ reference frame system as follows:

$$\sigma_1 = \frac{\sigma_L + \sigma_T}{2} + \sqrt{\left(\frac{\sigma_L - \sigma_T}{2}\right)^2 + {\tau_{LT}}^2} \tag{26}$$

2.4.2 Residual Function for the Initial Estimates

The first step of initiating the solution procedure is to compute the initial estimates of the average strains $\varepsilon_D, \varepsilon_L$ and ε_T. To do so, few equations are derived for the calculation procedure namely: the principal compressive stress in concrete, as well as the variable angle α_D as a function of the strains in the $L-T$ and $R-D$ coordinate systems.

The following additional equations are computed to assist the calculation procedure:

σ_T, σ_L and τ_{LT} from Eq. (18) to (20) are substituted into Eq.(2).

$$m_L\sigma_1 - \rho_L f_L = cos^2(\alpha_D)\sigma_D + sin^2(\alpha_D)\sigma_D \tag{27}$$

$$m_T\sigma_1 - \rho_T f_T = cos^2(\alpha_D)\sigma_D + sin^2(\alpha_D)\sigma_D \tag{28}$$

$$m_{LT}\sigma_1 = sin(\alpha_D)cos(\alpha_D)(\sigma_R - \sigma_D) \tag{29}$$

Regarding the principal compressive stress in the concrete member (Figure 1), Eq. (29(27) is solved for σ_D, resulting the following equation:

$$\sigma_D = \sigma_R - \frac{m_{LT}}{\sin(\alpha_D)\cos(\alpha_D)}\sigma_1 \tag{30}$$

Eq.(30) is then taken and substituted into Eq. (27) and (28), then solved for the tensile stresses in the longitudinal (f_L) and transverse (f_T) reinforcement, respectively:

$$f_L = \frac{m_L + m_{LT}\cot(\alpha_D)}{\rho_L}\sigma_1 - \frac{\sigma_R}{\rho_L} \tag{31}$$

$$f_T = \frac{m_T + m_{LT}\tan(\alpha_D)}{\rho_T}\sigma_1 - \frac{\sigma_R}{\rho_T} \tag{32}$$

As for the variable angle α_D, it was written as a function of the stains in the $L-T$ and $R-D$ coordinate systems, by incorporating the trigonometric identity $sin^2(\alpha_D) + cos^2(\alpha_D) = 1$ into the first two lines of Eq.(3), the following two equations are obtained:

$$\sin(\alpha_D) = \sqrt{\frac{\varepsilon_L - \varepsilon_D}{\varepsilon_R - \varepsilon_D}} \tag{33}$$

$$\cos(\alpha_D) = \sqrt{\frac{\varepsilon_T - \varepsilon_D}{\varepsilon_R - \varepsilon_D}} \tag{34}$$

Eq.(33) and (34) are then divided as follows to compute the variable angle α_D from Eq.(38)

$$\tan(\alpha_D) = \sqrt{\frac{\varepsilon_L - \varepsilon_D}{\varepsilon_T - \varepsilon_D}} \tag{35}$$

To compute the initial estimates for the strains $\varepsilon_D, \varepsilon_L$ and ε_T, at this stage (first loading increment), and for simplicity, the tensile stress in concrete is neglected to compute the initial estimates, and the materials were considered to behave in the linear and elastic stages, so Hook's laws for concrete ($\sigma_D = E_c\varepsilon_D$), and steel bars ($f_L = E_s\varepsilon_L$ and $f_T = E_s\varepsilon_T$), holds. Hook's laws are then substituted into Eq.(30) to (32), and solved for the strains, giving the following equations:

$$\varepsilon_D = \frac{-m_{LT}\sigma_1}{E_c\, sin(\alpha_D)\, cos(\alpha_D)} \tag{36}$$

$$\varepsilon_L = \frac{(m_L + m_{LT}\, cot(\alpha_D))\sigma_1}{E_S\rho_L} \tag{37}$$

$$\varepsilon_T = \frac{(m_T + m_{LT}\, tan(\alpha_D))\sigma_1}{E_S\rho_T} \tag{38}$$

From Eq.(35) a nonlinear residual function ($F_{START}(\alpha_D)$) is stated (Eq.(39)), and the average strains are defined from equations (36) to (38).

To start the calculations of the refined efficient RA-STM procedure, this function (Eq.(39)) is set to zero, and numerically solved for α_D.

The solution angle α_D, the value which minimizes $F_{START}(\alpha_D)$, is used to compute the initial estimates $\varepsilon_D, \varepsilon_L$ and ε_T, by using again Eq.(36) to (38), then the calculation procedure is started.

$$F_{START}(\alpha_D) = \frac{\varepsilon_L - \varepsilon_D}{\varepsilon_T - \varepsilon_D} - tan^2(\alpha_D) \tag{39}$$

$$F_{START}(\alpha_D) = 0 \tag{40}$$

2.4.3 Residual functions for the efficient RA-STM

In the efficient RA-STM procedure, the chosen primary variables are the average strains $\varepsilon_D, \varepsilon_L$ and ε_T . To numerically compute them, two nonlinear residual functions were derived ($F^{(1)}{}_{RA-STM}(\varepsilon_L, \varepsilon_T)$ and $F^{(2)}{}_{RA-STM}(\varepsilon_L, \varepsilon_T)$) by following the next steps.

For the first residual function $F^{(1)}{}_{RA-STM}(\varepsilon_L, \varepsilon_T)$ Eq.(27) and (34) are added, then Eq.(33) and (34) are substituted in the resulting equation, and finally the terms are arranged.

The second residual function $F^{(2)}{}_{RA-STM}(\varepsilon_L, \varepsilon_T)$ is obtained in a similar way, by adding Eq.(29) and (34), then substituting Eq.(34) and (35) in the resulting equation and arranging the terms [4].

The two residual functions are represented in the following matrix equation:

$$\begin{bmatrix} F^{(1)}_{RA-STM}(\varepsilon_L, \varepsilon_T) \\ F^{(2)}_{RA-STM}(\varepsilon_L, \varepsilon_T) \end{bmatrix} = \begin{bmatrix} \sigma_D \frac{\varepsilon_T - \varepsilon_D}{\varepsilon_R - \varepsilon_D} + \sigma_R \frac{\varepsilon_L - \varepsilon_D}{\varepsilon_R - \varepsilon_D} - m_L \sigma_1 + \rho_L f_L + \rho_{Lf} f_{Lf} \\ \sigma_D \frac{\varepsilon_L - \varepsilon_D}{\varepsilon_R - \varepsilon_D} + \sigma_R \frac{\varepsilon_T - \varepsilon_D}{\varepsilon_R - \varepsilon_D} - m_T \sigma_1 + \rho_T f_T + \rho_{Tf} f_{Tf} \end{bmatrix} \tag{41}$$

The residual functions are set to zero (Eq.(42), (39), constituting a system of two nonlinear equations numerically solved for ε_T and ε_L. The solution's average strains ε_T and ε_L are the values which minimize both residual functions $F^{(1)}{}_{RA-STM}(\varepsilon_L, \varepsilon_T)$ and $F^{(2)}{}_{RA-STM}(\varepsilon_L, \varepsilon_T)$.

$$\begin{bmatrix} F^{(1)}_{RA-STM}(\varepsilon_L, \varepsilon_T) \\ F^{(2)}_{RA-STM}(\varepsilon_L, \varepsilon_T) \end{bmatrix} = \begin{bmatrix} 0 \\ 0 \end{bmatrix} \tag{42}$$

2.4.4 Algorithm for the efficient RA-STM procedure

Based on the equations presented in this chapter 2, an algorithm to compute the numerical solution points for the refined efficient RA-STM procedure was developed and implemented in

computer using MATLAB in a previous studies [4], [35], and modified for this work. The code is exhibited in Appendix I.

Figure 5. Flowchart. presents a flowchart of the algorithm and calculation procedure, and can be summarized as follows:

1. Data entry: the longitudinal and transverse reinforcement ratios (ρ_L, ρ_T), Young's modulus for steel (E_s), uniaxial yielding stresses of the longitudinal and transverse reinforcement (f_{Ly}, f_{Ty}), ultimate strain for concrete in compression (ε_{su}), uniaxial compressive strength of concrete (f'_c), tensile strength of concrete (f_{cr}), Young's modulus for concrete (E_c), strain corresponding to the tensile strength of concrete (ε_{cr}), strain corresponding to the concrete compressive peak stress (ε_0), ultimate strain for concrete in compression (ε_{cu}), reference factors for the longitudinal and transverse normal stress in the RC membrane element ($\sigma_L . \sigma_T$), reference factor for the shear stress in the RC membrane element in the L-T coordinate system (τ_{LT}) (for instance, for pure shear, reference factors for $\sigma_L . \sigma_T$ are set to zero and reference factor for τ_{LT} can be set to 1),. In addition, $\Delta\varepsilon_D$ parameter $\Delta\varepsilon_D$ refers to the path's increment for the principal compressive concrete strain (ε_D). The initial value for the principal compressive stain ε_D is defined as $\varepsilon_D^{K=0} = \varepsilon_D^0 = \Delta\varepsilon_D$ (with superscript K representing the step number of the calculation procedure).
2. The yielding strains for longitudinal and transverse reinforcement are then calculated using Hook's law ($\varepsilon_{Ly} = {f_{Ly}}/{E_s}$ and $\varepsilon_{Ty} = {f_{Ty}}/{E_s}$, respectively), in addition to the applied principal tensile stress σ_1, from Eq.(26), and the proportionality coefficients m_L, m_T and m_{LT}, using Eq.(18) to (20).

3. Next step is to compute the initial estimates. For this, the residual function $F_{START}(\alpha_D)$ is solved (minimized) for the variable angle (α_D), Eq.(39) and (40).

4. The average strains ($\varepsilon_D, \varepsilon_L$ and ε_T) are then introduced with Eq.(36) to (38), by forming a system of equations consistent of the residual function and the strains. It is possible to compute the value of the variable angle (α_D), which afterwards is used in calculating the average stains. Those are going to be defined as the initial estimates ($\varepsilon_D^1, \varepsilon_L^1$ and ε_T^1) to compute the first solution point and start the solution procedure.

5. Compute the primary variables ε_L and ε_T for each step k and each incremented strain $\varepsilon_D^k = \varepsilon_D^{k-1} + \Delta\varepsilon_D$, by solving (minimizing) the residual functions (${F^{(1)}}_{RA-STM}(\varepsilon_L, \varepsilon_T)$ and ${F^{(2)}}_{RA-STM}(\varepsilon_L, \varepsilon_T)$) (Eq.(41)and (42)). For each step k, the initial point is defined as the solution point from the previous step ($k-1$).

6. Calculate, for each step, the principal tensile strain ε_R from Eq.(4), the principal tensile stress in concrete σ_R form Eq.(11), the principal compressive stress in concrete σ_D from Eq.(6), the tensile stresses in the longitudinal (f_L) and transverse (f_T) steel reinforcements from Eq.(14), and recalculate the applied principal tensile stress σ_1 from Eq.(25).

7. The calculation procedure holds, until the ultimate value specified for the concrete in compression (ε_{cu}), or one of the failure criteria is reached ($\varepsilon_D \geq \varepsilon_{cu}, \varepsilon_L \geq \varepsilon_{su}$ or $\varepsilon_T \geq \varepsilon_{su}$); otherwise, repeat step 5 and 6.

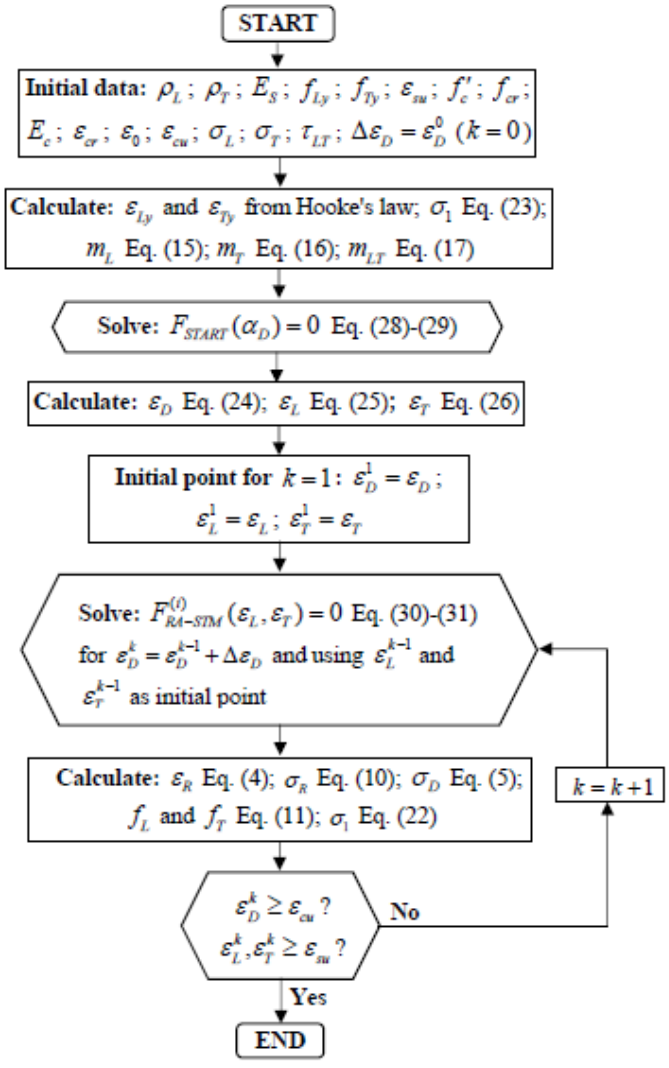

Figure 5. Flowchart.

3 Comparative Analysis with Experimental Results

3.1 Previous Experimental Study

The research chosen for comparison in this study, as mentioned previously, was the one held by Hsu and Mansour in the university of Houston using the Universal Panel Tester [36], for various reasons, namely: i) the number of reinforced concrete (RC) panels tested under cyclic shear is much higher than the ones tested in other facilities; ii) the higher number of tests allowed to incorporate new features as variable studies, such as ratio of the longitudinal to the transverse reinforcement ratio, and the direction of the reinforcements; *iii)* the universal panel tester allowed to perform biaxial tests on RC panels under controlled conditions, along with simulating different types of incremental loadings and their combinations (proportional or sequential).

Figure 6 represents a picture of the universal panel tester. This device has high loading capacity and can test full-size panels up to 1,4 m^2, 0,4 m thick; by virtue of its large (5×5) m steel frame, and 40 tons of weight. It also consists of forty in-plane jacks, 100 tons capacity each, and twenty out-of-plane jacks of 60 tons capacity each.

The jacks are individually regulated by a servo-controlled hydraulic system. Formed by a 5000 psi (34,474 MPa) pump, hardline steel tubes of 0,7 km length, high pressure hoses, a 60 four-way valves control board, and a servo control system.

Later on, a new data management system was added to upgrade the servo control capacity, alongside a mode switch that allows to shift between strain-control mode, and load-control mode. A new real time analysis and graphic capability was also added [37].

The incorporation of the universal panel tester equipped with a servo-control system was particularly crucial as it can carry out strain-controlled tests with proportional loading. Therefore, to observe the post-yield hysteretic loops with high accuracy. This aspect is of particular interest for this study.

Furthermore, Mansour *et al.* in 2001 [38], tested three panels (series CVE) with steel grids parallel to the principal stress. Even though the test results were not used in this study since the loading conditions were different (sequential), it was possible to determine the cyclic constitutive laws of concrete.

The last feature to mention is the varying longitudinal to transverse percentage of steel, and the steel bars orientation, which helped to evaluate the hysteretic loops of the shear-stress versus shear-strain curves for different design features.

(a) South view

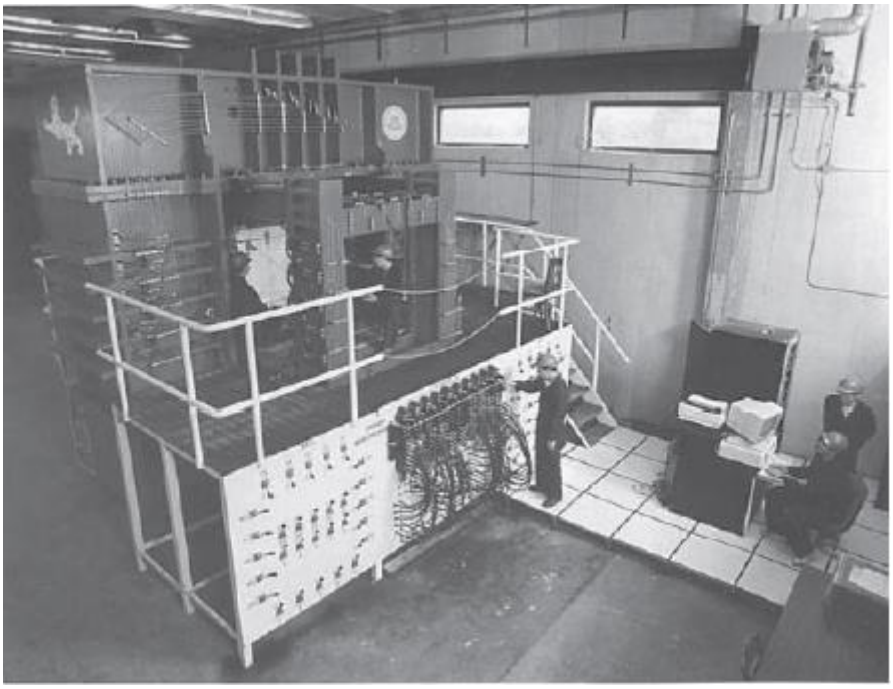

(b) North view

Figure 6. Universal panel tester at the University of Houston[28]

3.1.1 Test Program and Panels:

The tests were carried out at the University of Houston. They involved 12 full-size reinforced concrete membrane elements (panels), which were tested under reversed cyclic shear, to study and observe the effect of two variables:

1) The angle between steel bars and the applied principal stress, which varied among four angles ($\alpha_2 = 45°$, $68.2°, 79.8°$, and $90°$. See Figure 7. Loading conditions and reinforcement layout of the reference RC panels Figure 7).
2) The reinforcement ratios in the longitudinal (ρ_L), and transversal (ρ_T) direction, which can be equal or not.

All the other material properties and test variables remained approximately constant throughout the study, such as the concrete cylinder compressive strength (f'_c), which was maintained at a target value of 42 MPa [28].

As for the reinforcement, it was composed of grade 60 deformed bars. Three sizes of bars were used: #4, #6, and #8, with a cross-section of 129, 284, and 510 mm^2 respectively. The mechanical properties for the steel bar used in the test program are presented in

Table 1, in which f_y refers to the yielding strength, whereas E_s is the modulus of elasticity of bare steel bar.

Table 1. Mechanical Properties of steel bars

Steel bar	f_y (MPa)	ε_y	E_s (GPa)	ε_u
#4	424.1	0.0019	223.2	0.38
#6	425.4	0.0020	212.7	0.33
#8	453.4	0.0024	188.9	0.31

Note: ε_u is the strain at rupture.

The study specimens were grouped into several series, namely: CA, CB, CD, CE, and CF, as shown in Table 2.

In the specimens' identification system, the letter "C" refers to the nature of applied load, which was in this case cyclic.

The second letters "A, B, D, E, and F" refer to the steel grid orientation in the panels:

- E: grid orientation of 90°, meaning that the steel grid was parallel to the applied principal horizonal and vertical stresses. The steel grid ratios were equal in both the longitudinal and transverse directions.
- A: grid orientation of 45°, meaning that the steel grid was oriented at 45° angle to the applied principal vertical stresses. The steel grid ratios were also equal in both directions.

- B: grid orientation of 45°, but different from the A-series. The steel ratios in the longitudinal and transverse directions were not equal, as it was chosen to be bigger in the longitudinal direction.
- D: grid orientation of 68,2°, meaning that the angle between the longitudinal steel direction (L) and the direction of the applied vertical stress was 68,2°. Steel ratios were equal for both longitudinal and transverse directions.
- F: grid orientation of 79,8°, in other words, the angle between the longitudinal steel direction (L), and the principal vertical stress direction was 79,8°. The steel grid ratios were equal in both directions.

Regarding the numerical digits "2, 3, and 4", they refer to the percentage of steel; the larger the number is, the larger the steel ratios in panels are. As for panels with different reinforcement ratios, those were labeled according to the larger steel percentage used in each panel.

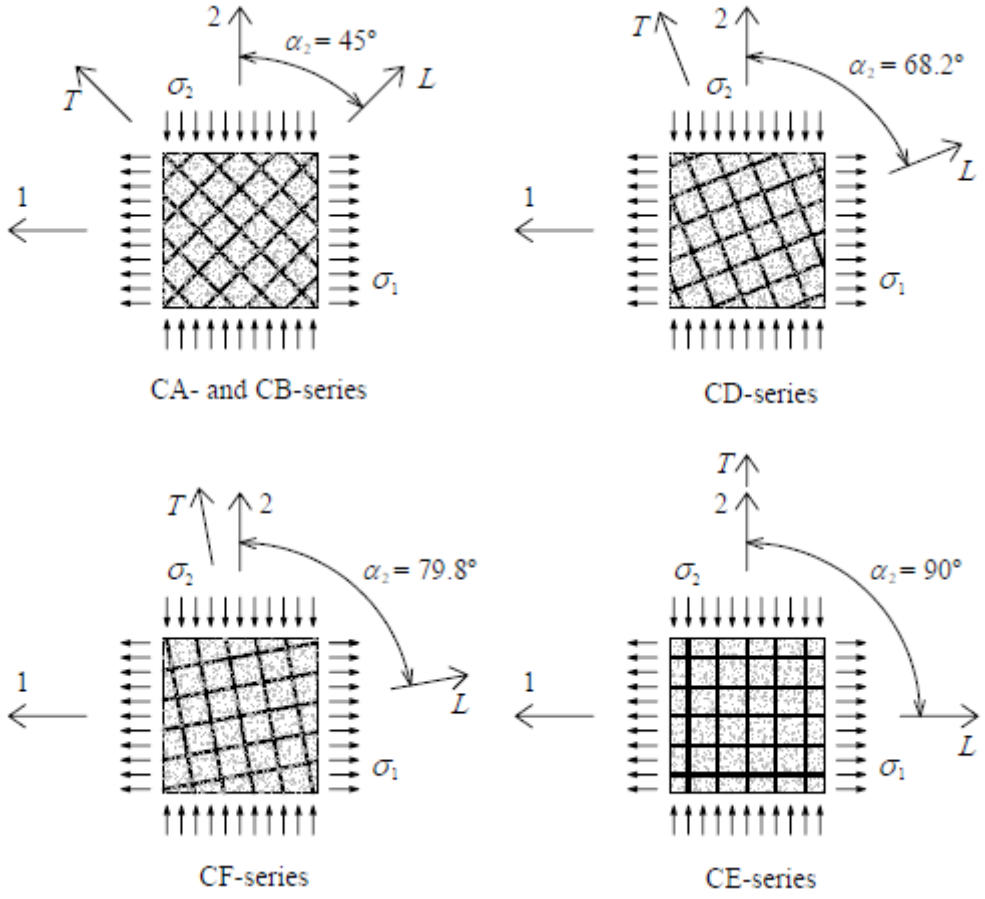

Figure 7. Loading conditions and reinforcement layout of the reference RC panels

The coordinate systems that have been used for all panels in this study are:

- (V, H) which coincide with the reference frame (1,2) from Figure 7, and represents the horizontal H, and vertical V directions of the applied principal stresses.
- (L, T) that represents the longitudinal and transverse directions of the steel bars.

The steel bars angle α_2 represents the angle between the two coordinate systems $(V-H)$, and $(L-T)$.

The reinforced concrete panels with #4 or #5 rebars were uniformed in size, with $1397 \times 1397 \times 178$ mm, while RC panels with #8 rebars were dimensioned with $1397 \times 1397 \times 203$ mm. The thickness of these panels was increased to accommodate and cover the larger rebars.

The panels incorporated two layers of steel bars, one in each direction. The reinforcement ratio for each direction was calculated including the steel bars within the measured region only, since the reinforcing bars out of the measured area were intended to strengthen the edge of the panels, so that the failure occurs in the measured region. The spacing between bars ranged from 188 to 267 mm in both L and T directions.

Table 2 exhibits the mechanical properties and the steel bars arrangements of the RC panels, where f_c' is the maximum compressive stress of concrete, and ε_0 is the corresponding peak concrete strain.

Table 2. Main properties of the referenced RC panels [28].

Series	Panel	f_c' MPa	ε_0 %	ρ_L [(1)] %	ρ_T [(1)] %	α_2 °
CA	CA2	45	0.25	0.77	0.77	45
	CA3	44.5	0.24	1.7	1.7	45
	CA4	45	0.28	2.7	2.7	45
CB	CB3	48	0.26	1.7	0.77	45
	CB4	47	0.24	2.7	0.67	45
CD	CD2	44.5	0.25	0.59	0.59	68.2
	CD3	47	0.26	1.3	1.3	68.2
	CD4	43	0.24	2.0	2.0	68.2
CE	CE2	49	0.23	0.54	0.54	90
	CE3	50	0.24	1.2	1.2	90
	CE4	47	0.22	1.9	1.9	90
CF	CF2	44	0.25	5.6	5.6	79.8

[(1)] $\rho_L = {}^{A_L}/_{A_C}$ and $\rho_T = {}^{A_T}/_{A_C}$ (A_C is the area of the concrete cross-section)

In the CE series, the bars orientation was in the direction of the applied principal stress, where the longitudinal reinforcement direction was parallel to the applied horizontal stress, while the transverse reinforcement was parallel to the vertical stress direction. It was particularly important to study this series for two reasons: (1) the panels CE helped establish and compute the cyclic constitutive laws of reinforcement bars embedded in concrete as reported by Mansour [38], (2) the steel bars angle in the panels served as reference angle ($\alpha_2 = 90°$), to study how the hysteretic loops and the stress-strain curves are affected by the orientation of steel bars.

The other panels from series CA, CD, and CF were designed to study the shape of the hysteretic loops and how they vary with different angles values. The series CB was designed to compare and study the effect of different longitudinal and transverse steel ratios (Table 2) on the hysteretic loops.

3.1.2 Loading Method

The test was carried out by subjecting reversed cyclic stresses in both horizontal and vertical directions on all test panels, using the Universal Panel Tester. Figure 8 illustrates a typical loading history for panel CA3.

As has been explained previously, the Universal Panel Tester was equipped with a servo-control system allowing to carry out stress- and strain-controlled tests, with the yielding point marking that transition.

In the stress-controlled mode, the vertical principal stress was controlled by the horizontal stress, in a way that they were equal in magnitude and opposite in directions, which created a state of pure shear stress at 45° direction to the principal stress (see Figure 7). Noting that the state of pure shear stress occurs when the sum of normal principal stresses is zero, or when the tension in one direction is equal to the compression in the perpendicular direction.

To incorporate the effect of cyclic loading, the shear stresses wavered between the positive and negative values with increasing amplitude as shown in Figure 8. The absolute values of maximum shear strains (positive and negative) were multiples of the yield shear strain.

To obtain the smeared stresses and smeared strains records, the jack forces and panels deformation during testing were measured. The 40 in-plane jacks, 20 horizontals and 20 verticals, were used to apply the loads throughout the panels surface.

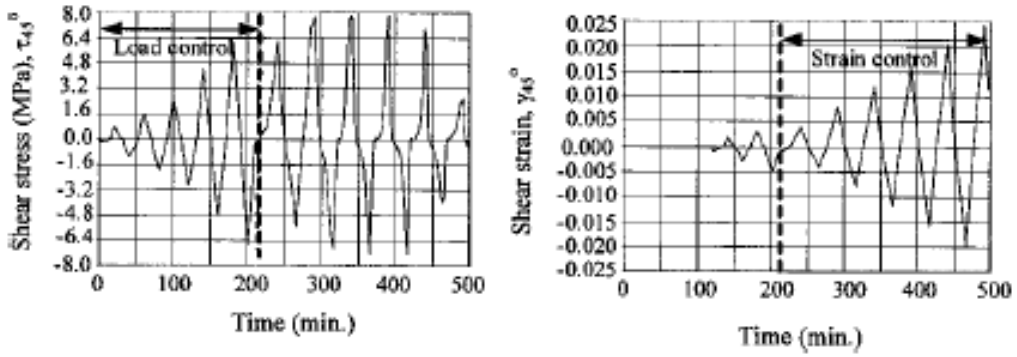

Figure 8.loading history of panel CA3[28]

3.1.3 Experimental Results and Hysteretic Loops

This experiment used two LVDTs arrangements depending on the steel grid orientation in the test panels.

For panel with symmetical orientation at an angle of 45° or 90° with respect to the applied principal vertical stresses (CA, CB, and CE series), 10 LVDTs were placed on each face of the test panels.

Figure 9 and Figure 10 exhibit CB- and CD- series panels in test position, in addition tho the LVDTs arrangment of the mentioned panels.

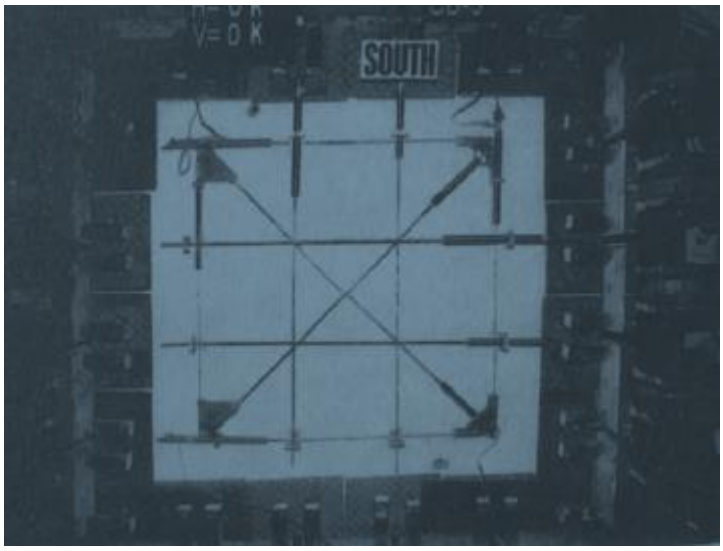

Figure 9. LVDTs arrangement of typical panel in the CB- series. [38]

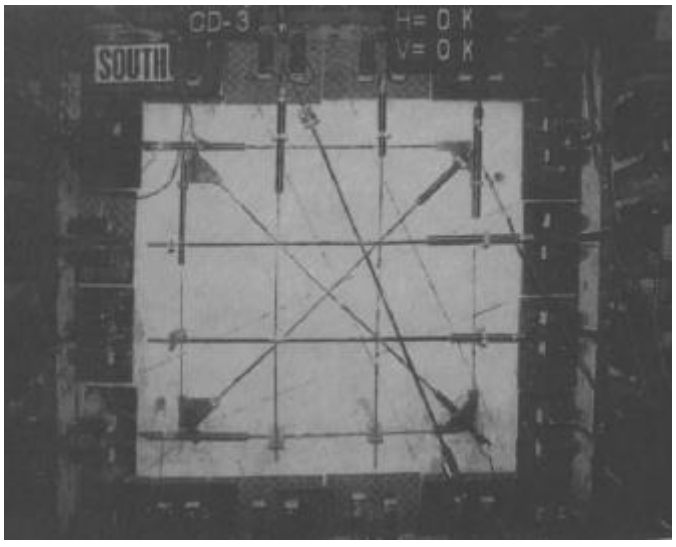

Figure 10. LVDTs arrangement of typical panel in the CD- series. [38]

As for panels of unsymmetrically oriented steel grid at an angle of 68.2° or 79.8° with respect to the applied vertical stresses (CD-, CF- series) respectively, an additional LVDT was added to each face in the transverse direction.

After the test was conducted, the cracks patterns and widths were taken. The following Figure 11 and Figure 12 show the development of cracks in panel CA2 and panel CA4, with panel CA2 lightly reinforced and panel CA4 heavily reinforced.

By comparing the panels it can be noted that, in addition to the tensile strain, the cracks development also depends on the reinforcement ratio. When the reinforcement ratio is small, fewer cracks were formed with larger crack widths. As for heavily reinforced panels, a constrast was observed, large number of cracks developed, with smaller widths that increased much slower than the ones in lightly reinforced panels. [38]

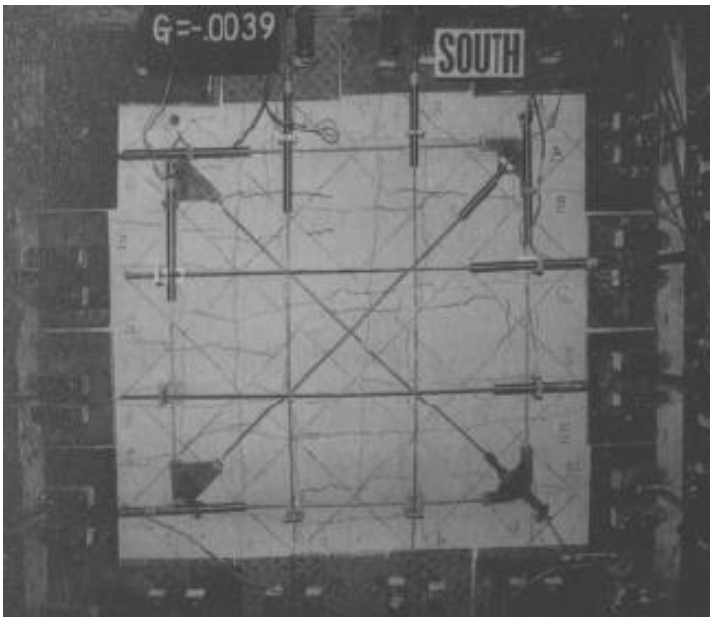

Figure 11. Crack pattern of panel CA2. [38]

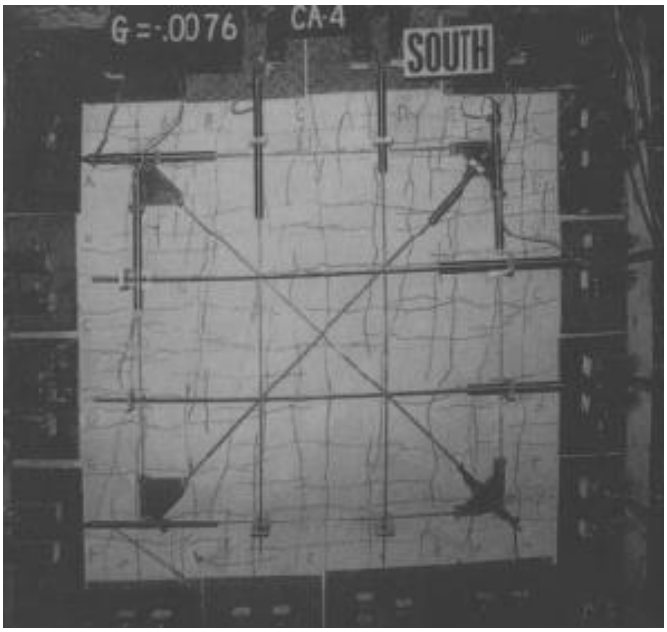

Figure 12. Crack pattern of panel CA4. [38]

Figure 13 exhibits the crack patten for panel CB3. In this series of panels with unsymmetrical reinforcement ratios, crack rotation was noticeable with respect to the initial horizontal. During the tests, it was observed that the direction of the cracks gradually deviated from the initial crack direction towards the $L-$ direction.

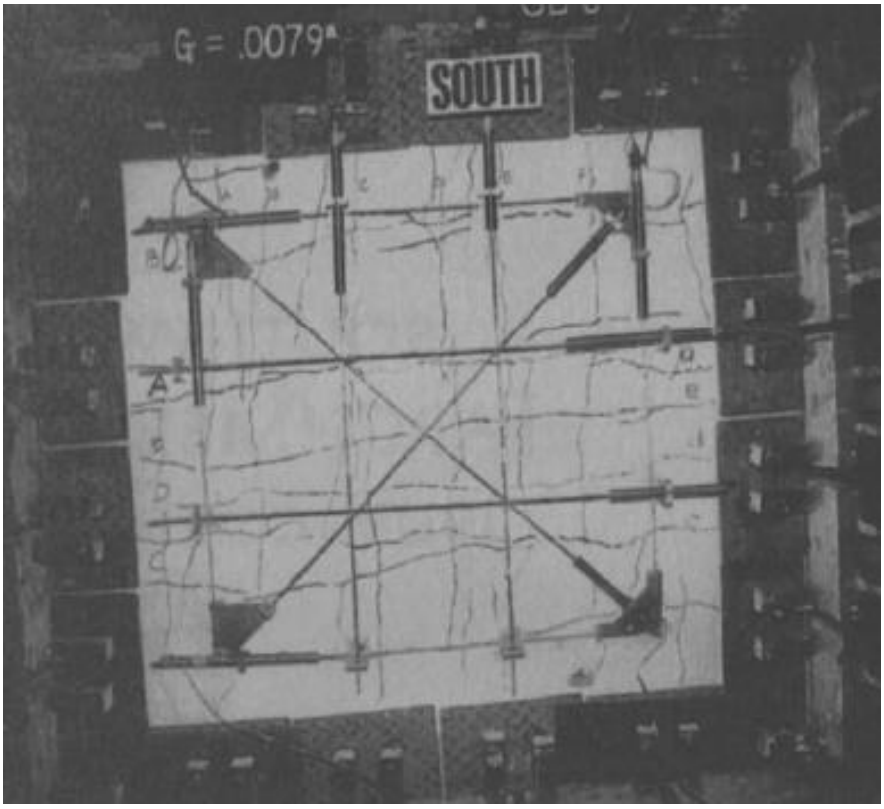

Figure 13. Crack pattern of panel CB3. [38]

The following Figure 14 illustrates the results throught the experimental hysteretic loops of the shear-stress and shear-strain curves of test panels.

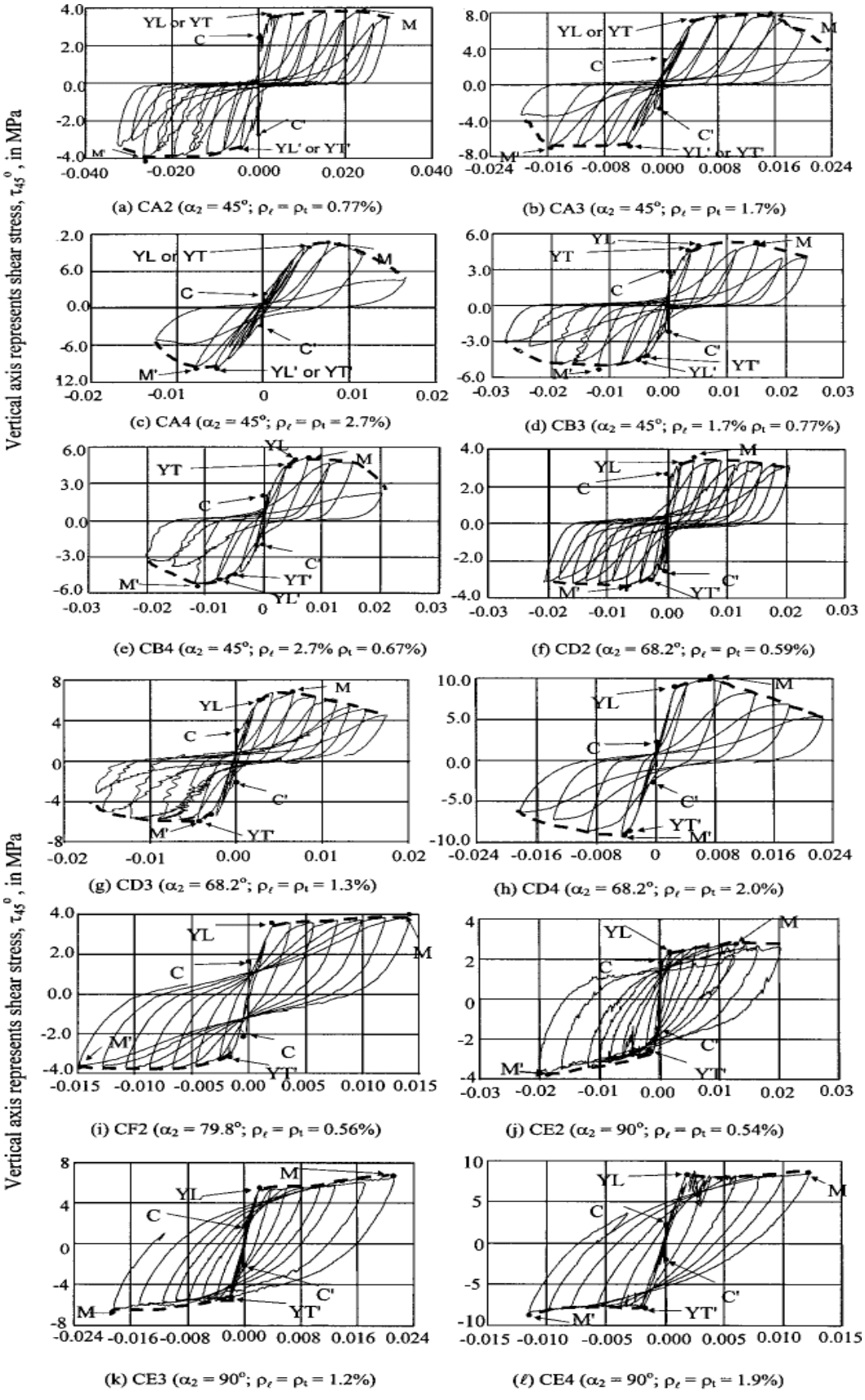

Figure 14. Cyclic shear-stress versus shear-strain curves of test panels. [28]

Table 3. Definition of Critical Points

Loading direction	Point label	Meaning of critical points
Positive	C	Cracking shear stress of panel
	YT	Yielding of steel bars in the transverse direction
	YL	Yielding of the steel bars in the longitudinal direction
	M[a]	Maximum shear stress
Negative	C'	Cracking shear stress of panel
	YT'	Yielding of steel bars in the transverse direction
	YL'	Yielding of the steel bars in the longitudinal direction
	M'[a]	Maximum shear stress

Critical points from Figure 14 are marked and labeled, the definition of these points can be found in **Table 3**.

Envelop curves are presented as the dotted curves in Figure 14. Each panel has two envelope curves, one negative and another positive. These curves are drawn from the yield point to an ultimate point, which is chosen for the two cases as follows[28]

1) No descending branch exists in the envelope curves: the ultimate point is marked as the point of maximum shear stress (τ_{max})).
2) A descending branch is observed: the ultimate point is defined as the point where the ultimate shear stress (τ_u) is equal to 80% of the maximum shear stress (0.8 τ_{max}) in the descending branch.

3.2 Comparative Analysis

3.2.1 Previous Considerations

In this section, the data and results that were obtained from the mentioned experimental research (reference [38]), were used as a base to compare the predictions from the efficient RA-STM module, for $\tau - \gamma$ envelope curves of RC panels under cyclic shear.

The panels' dimensions and properties chosen for the efficient RA-STM procedure were identical to the ones in reference [38] (**Table 2**) for continuity in comparison variants.

As for other material properties that were not specified in reference [28], in this study they were computed from Eurocode 2 [39], namely, by a correlation with f_c'. This was done for the tensile concrete strength under a biaxial state (f_{cr}), and for the Young's modulus for concrete (E_c) (eq.(12)-(13)).

The efficient RA-STM procedure was used to compute the monotonic response of the RC reference panels (**Table 2**).

To simplify and better understand the reference frames, they were labeled as follows:

- The $1-2$ reference frames: indicate the global horizonal and vertical directions of the panels;
- The $L-T$ reference frames: coincide with the direction of the longitudinal and transverse reinforcement;
- The $L'-T'$ reference frames: indicate a reference frame with a 45° angle with respect to the $1-2$ reference frame.

As this study is performed considering that the RC panels are under monotonic pure shear, it was important to introduce the $L'-T'$ reference frames to satisfy this condition for the CD, CE, and CF series.

For panels of the CA and CB series, the $L-T$ reference frame coincides with $L'-T'$ frame, to the contrary for panels of the CD, CE, and CF series. And all the theoretical monotonic $\tau-\gamma$ curves for all the RC panels were computed with respect to the $L'-T'$ reference frames, these curves are named as "envelope $\tau_{45°}-\gamma_{45°}$ curves" from now on.

It was also necessary to compute an equivalent steel grid reinforcement with equivalent ratios $\rho_{L'}$ and $\rho_{T'}$ for the RC reference frames from CD, CE, and CF series. This was carried out by using the usual transformation rules for the reference frames under rotation by knowing ρ_L and ρ_T, and the required angle the $L-T$ reference frame must rotate to coincide with the $L'-T'$ reference frame (this is further explained in Appendix III). For such panels, the equivalent reinforcement rations $\rho_{L'}$ and $\rho_{T'}$ were considered as inputs in the efficient RA-STM procedure.

Mansour and Hsu in a previous study [3] explained the importance of incorporating the damage coefficient D. As the horizontal and vertical principle applied stresses are subjected to out-of-phase compression-tension stresses, a damage coefficient needs to be incorporated in the envelope compression stress-strain curves of concrete to take into account the damage caused by the history of tensile and compressive stress reversal normal to compression direction being considered.

$$D = 1 - \psi \frac{\varepsilon'_c}{\varepsilon_0} \leq 1.0 \tag{43}$$

In Eq.(43) ψ refers to a damage parameter, ε'_c is the maximum compression strain normal to the compression direction under consideration and that occurred in the previous loading cycles. ε_0 is the concrete cylinder compressive strain corresponding to the peak cylinder stress [3].

In 2001 [38] Mansour studied the variations of a damage parameter ψ. It was taken as a value of ψ = 0.4, in order to provide a value of the damage coefficient D that better fitted the experimental results.

From previous Eq.(43), it can be observed that the only present variable is the strain.

Mansour in the mentioned study considered the strain as the maximum compression strain normal to the compression direction under consideration, whereas here the strain was monolithically incremented with small steps until the conventional failure of the RC panel was reached.

From studying the damage parameter Mansour concluded that the notable influence in incorporating and modifying the parameter, was in the post peak part of the hysteretic $\tau_{45^\circ} - \gamma_{45^\circ}$ loops, and no notable influence in the envelope $\sigma - \varepsilon$ curve for concrete in compression was observed when compared to the monotonic one.

This conclusion matches the results obtained in this study; two main points were observed after doing some calculation attempts:

- No notable effect on the theoretical envelope curves $\overset{\circ}{\tau}_{45} - \overset{\circ}{\gamma}_{45}$ was perceived for RC panels whose failure was imposed by the steel reinforcement in tension;
- For RC panels whose failure was due to concrete in compression, some convergence problems were observed after the peak shear stress.

Based on the information above, it was decided to not incorporate the damage parameter in the monotonic curve for concrete in compression to compute the envelope $\tau_{45^\circ} - \gamma_{45^\circ}$ curves of each reference RC panel from **Table 2** with the efficient RA-STM procedure.

3.2.2 Theoretical Results and Envelope Curves

Figure 15, and Figure 16 exhibit the theoretical envelope $\tau_{45^\circ} - \gamma_{45^\circ}$ curves from the efficient RA-STM procedure against the experimental curves for each RC panel. The experimental envelope $\tau_{45^\circ} - \gamma_{45^\circ}$ curves were drawn from the hysteretic $\tau_{45^\circ} - \gamma_{45^\circ}$ loops reported in reference [28], and illustrated in Figure 17.

The graphs demonstrate two envelope curves: a theoretical curve computed with the efficient RA-STM procedure labeled as (“Eff. RA-STM”), and the experimental curve labeled as (“Exp”); both envelope curves present a positive (“+”) and negative (“-“) shear loading direction.

It should be mentioned that neither the experimental nor theoretical $\tau_{45^\circ} - \gamma_{45^\circ}$ hysteretic loops computed with CSMM from references [28] and [38] are illustrated in Figure 15, and Figure 16; as only the envelope $\tau_{45^\circ} - \gamma_{45^\circ}$ curves are studied here.

After analyzing Figure 15 and Figure 16, it was observed that the theoretical $\tau_{45^\circ} - \gamma_{45^\circ}$ envelope curves computed with the efficient RA-STM procedure are in a reasonably good agreement with the experimental ones, for both the positive and negative shear loading.

It was shown that the efficient RA-STM procedure -for most of the RC reference panels- was able to capture well the global response of the RC panels until the maximum shear stress is reached, as well as the transition from the uncracked to the cracked stage, and also the yielding point.

Regarding the descending branch, it was observed that for some RC reference panels (CB4, CD3, CE4), after the peak shear stress is reached, less accurate results from the efficient RA-STM procedure were reported. However, this feature is not of much interest for a precheck analysis or predesign.

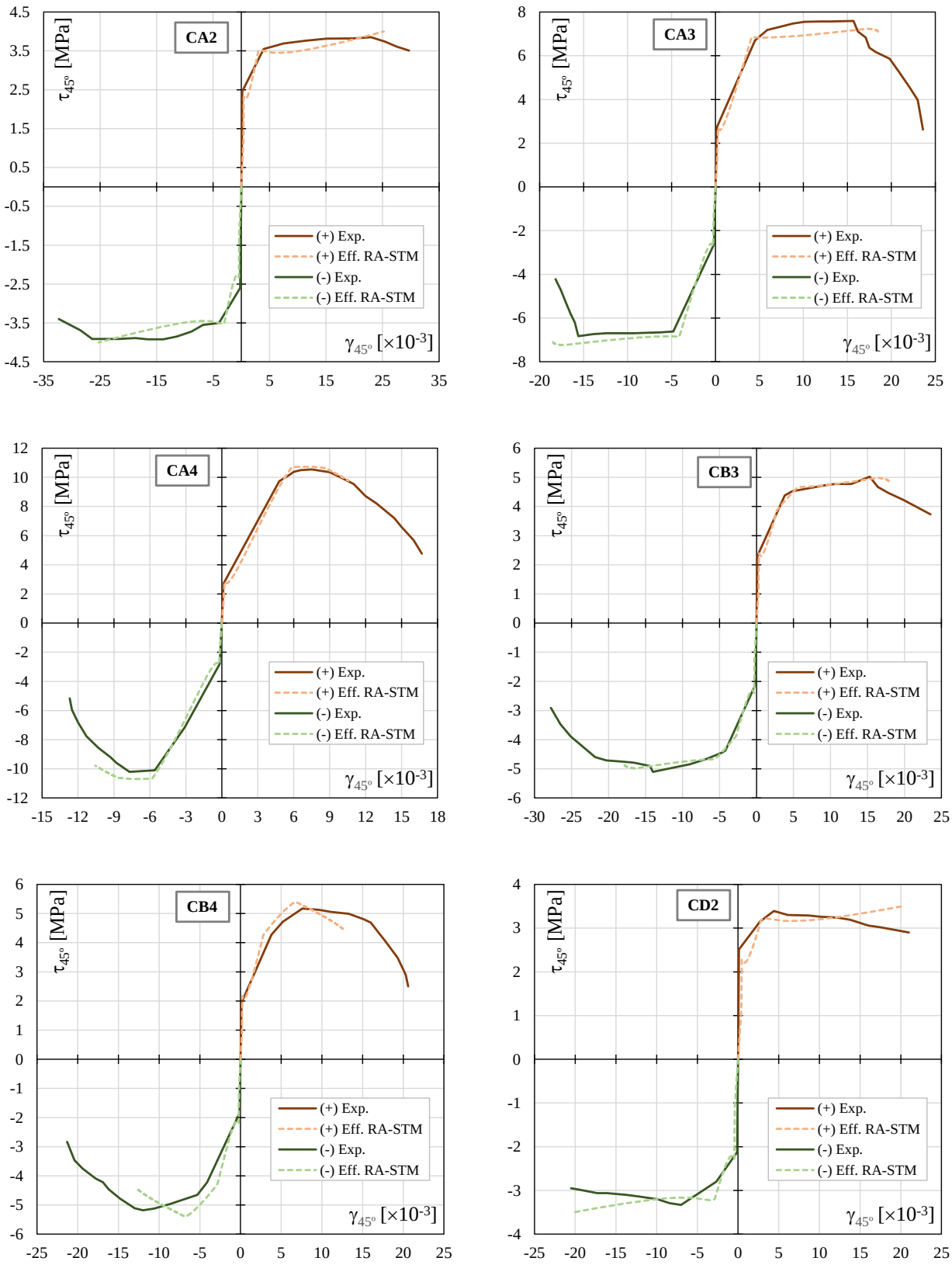

Figure 15. Envelop $\tau_{45}^{\circ} - \gamma_{45}^{\circ}$ curves for the reference RC panels (CA2, CA3, CA4, CB3, CB4, and CD2)

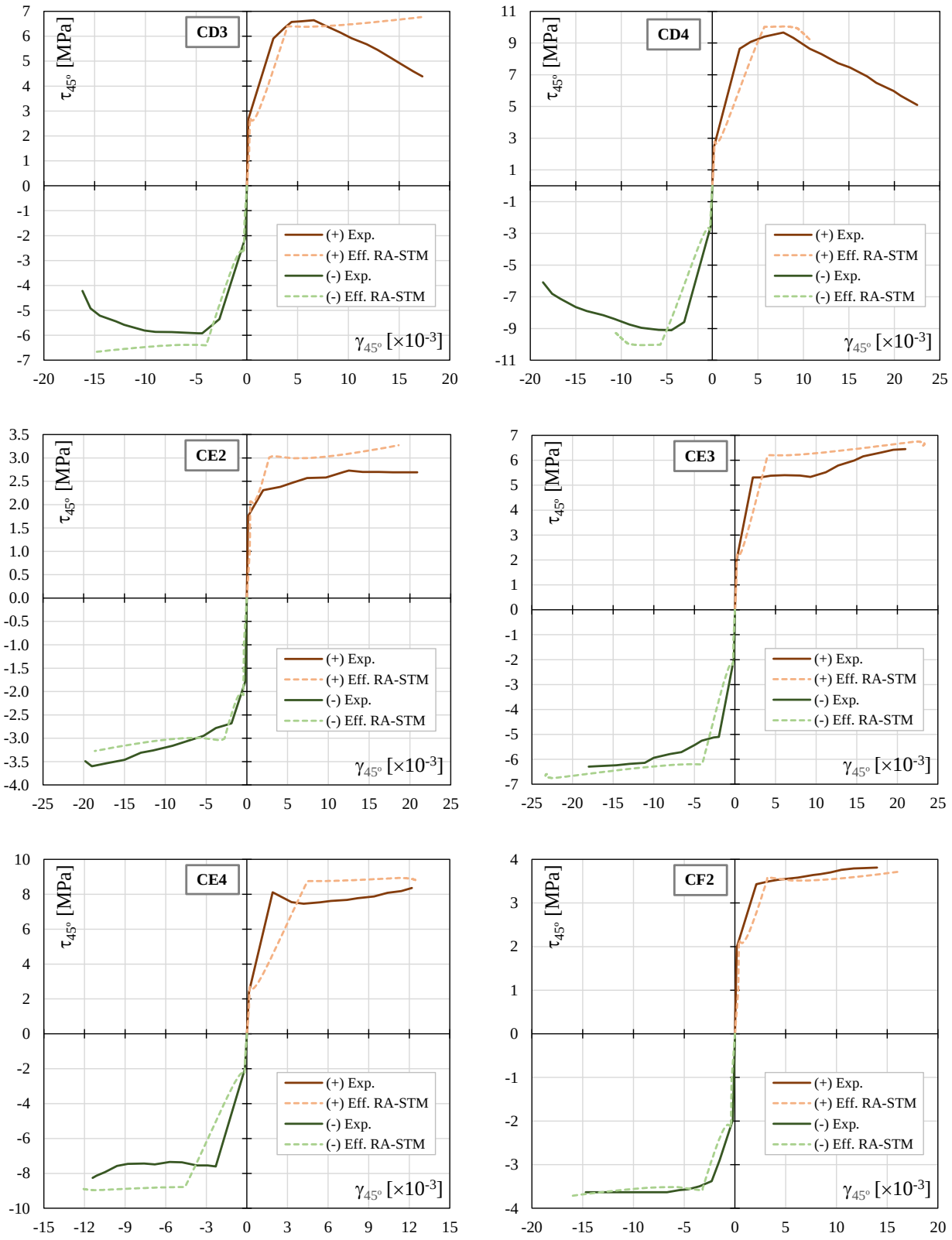

Figure 16. Envelop $\tau_{45}^{\circ} - \gamma_{45}^{\circ}$ curves for the reference RC panels (CD3, CD4, CE2, CE3, CE4, and CF2)

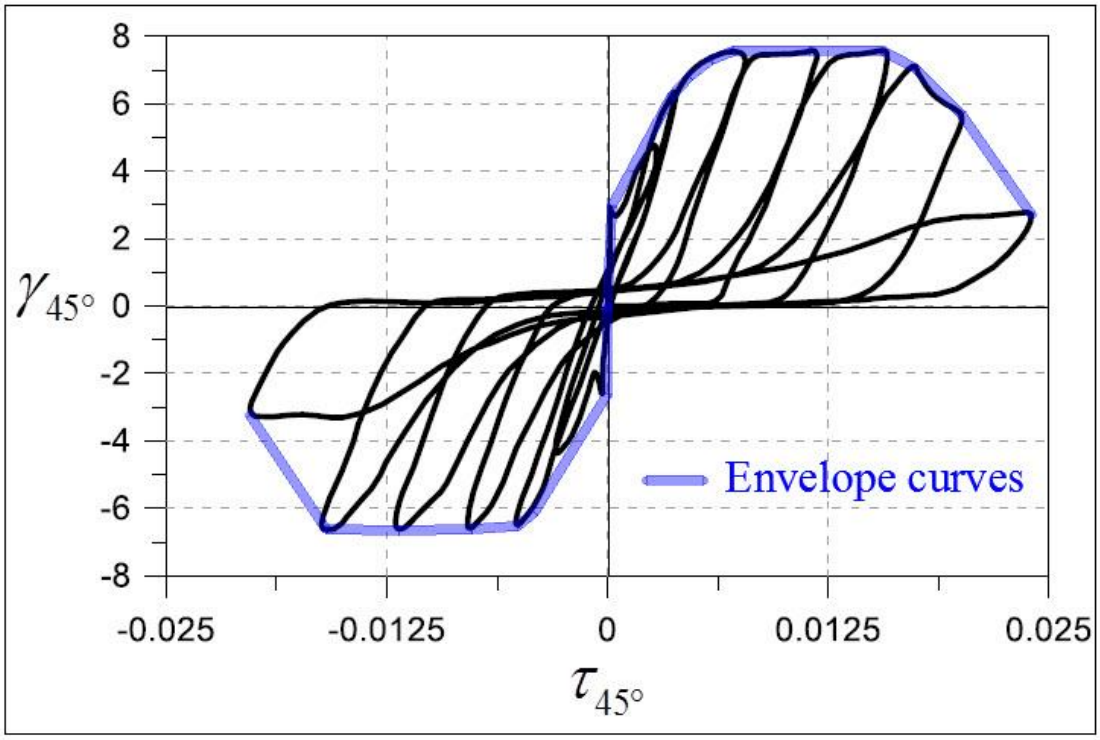

Figure 17. Drawing of the experimental envelope curve from the hysteretic loops.

3.2.3 Quantitative Comparative Analysis

The following tables (**Table 4** – **Table 7**) a quantitative comparative analysis between the theoretical and experimental numerical results for each reference RC panel.

These results consist of the theoretical and experiment coordinates of significant key points of the envelope $\tau_{45}^{\circ} - \gamma_{45}^{\circ}$ curves such as: concrete cracking, reinforcement yielding, and maximum shear stress.

Table 4, and **Table 5** exhibit the referred values for the positive ("+") loading shear direction; whereas **Table 6** and **Table 7** present these values for the negative ("-") loading shear direction.

The following experimental ("exp"), and theoretical ("th") values are presented in the mentioned tables:

- The cracking shear stresses ($\tau_{cr,exp}$ and $\tau_{cr,th}$), and corresponding shear strains ($\gamma_{cr,exp}$ and $\gamma_{cr,th}$)
- The yielding shear stresses ($\tau_{y,exp}$ and $\tau_{y,th}$), and the corresponding shear strains ($\gamma_{y,exp}$ and $\gamma_{y,th}$)
- The peak shear stresses ($\tau_{max,exp}$ and $\tau_{max,th}$), and the corresponding shear strains ($\gamma_{max,exp}$ and $\gamma_{max,th}$)

- The shear ductility factor ($\mu_{E\gamma,exp}$ and $\mu_{E\gamma,th}$)

It should be mentioned that the yielding point for reference RC panels with asymmetrical reinforcement ratios, for each loading direction, was the point corresponding to the first reinforcement (longitudinal or transversal) yield.

It was considered very important to include the concept of the envelope shear ductility factor $\mu_{E\gamma}$, It was considered very important to include the concept of the envelope shear ductility factor $\mu_{E\gamma}$, which is a measure of the ductility of RC panels under shear. As it is crucial to design and understand the response of RC structures subjected to cyclic shear, like the one induced by an earthquake for instance, with such factor it is possible to prevent brittle failure or sudden total collapse.

This parameter is defined as in reference [28], it is the ratio of the envelope shear strain at ultimate, γ_u, to that at the onset of yielding γ_y, as follows:

$$\mu_{E\gamma} = \frac{\gamma_u}{\gamma_\gamma} \tag{44}$$

Where γ_u is defined as the ultimate shear strain and is determined as follows:

- When the envelope $\tau_{45}^{\circ} - \gamma_{45}^{\circ}$ curve does not exhibit a descending branch: it is the shear strain corresponding to the last point of the curve;
- When the envelope $\tau_{45}^{\circ} - \gamma_{45}^{\circ}$ curve does exhibit a descending branch: it is defined as the shear strain of the point in the curve corresponding to (0.8 τ_{max}) in the descending branch.

The experimental values of those parameters are incorporated in **Table 5**, and **Table 7** are the values reported in reference [28].

Finally, the ratios of the experimental to the theoretical incorporate values; and for each of them, the mean ($\bar{x}$), the standard deviation (s), and the coefficient of variation (cv) are also presented in (**Table 4** to **Table 4**)

Table 4. Comparative analysis: positive (+) loading shear direction (cracking and yielding points).

Panel	$\tau_{cr,exp}$ MPa	$\tau_{cr,th}$ MPa	$\frac{\tau_{cr,exp}}{\tau_{cr,th}}$	$\gamma_{cr,exp}$ $\times 10^{-3}$	$\gamma_{cr,th}$ $\times 10^{-3}$	$\frac{\gamma_{cr,exp}}{\gamma_{cr,th}}$	$\tau_{y,exp}$ MPa	$\tau_{y,th}$ MPa	$\frac{\tau_{y,exp}}{\tau_{y,th}}$	$\gamma_{y,exp}$ $\times 10^{-3}$	$\gamma_{y,th}$ $\times 10^{-3}$	$\frac{\gamma_{y,exp}}{\gamma_{y,th}}$
CA2	2.46	2.32	1.06	0.16	0.44	0.37	3.55	3.53	1.01	3.94	3.13	1.26
CA3	2.76	2.71	1.02	0.19	0.28	0.68	6.70	6.80	0.99	4.50	4.07	1.10
CA4	2.71	2.84	0.95	0.14	0.26	0.53	10.20	10.71	0.95	5.70	5.86	0.97
CB3	2.30	2.40	0.96	0.11	0.33	0.34	4.52	4.27	1.06	4.80	4.24	1.13
CB4	1.95	2.17	0.90	0.14	0.22	0.62	4.72	4.83	0.98	5.20	4.82	1.08
CD2	2.51	2.28	1.10	0.12	0.46	0.26	3.15	2.86	1.10	2.70	2.32	1.16
CD3	2.67	2.73	0.98	0.14	0.31	0.45	5.91	6.40	0.92	2.60	3.97	0.65
CD4	2.41	2.80	0.86	0.15	0.24	0.62	8.64	10.00	0.86	3.00	5.69	0.53
CE2	1.75	2.07	0.85	0.15	0.42	0.36	2.31	3.01	0.77	2.00	2.73	0.73
CE3	1.95	2.22	0.88	0.17	0.27	0.63	5.31	6.11	0.87	2.20	3.96	0.56
CE4	2.40	2.70	0.89	0.16	0.21	0.76	8.11	8.75	0.93	1.90	4.56	0.42
CF2	1.98	2.15	0.92	0.18	0.39	0.46	3.43	3.53	0.97	2.10	3.16	0.66
$\bar{x}$ =			0.95			0.51			0.95			0.86
s =			0.08			0.16			0.09			0.29
cv =			8.5%			31.3%			9.4%			34.2%

Table 5. Comparative analysis: positive (+) loading shear direction (peak point and ductility)

Panel	$\tau_{max,exp}$ MPa	$\tau_{max,th}$ MPa	$\frac{\tau_{max,exp}}{\tau_{max,th}}$	$\gamma_{max,exp}$ $\times 10^{-3}$	$\gamma_{max,th}$ $\times 10^{-3}$	$\frac{\gamma_{max,exp}}{\gamma_{max,th}}$	$\mu_{E\gamma,exp}$	$\mu_{E\gamma,th}$	$\frac{\mu_{E\gamma,exp}}{\mu_{E\gamma,th}}$
CA2	3.85	4.00	0.96	23.00	25.22	0.91	7.54	8.06	0.94
CA3	7.59	7.23	1.05	15.70	17.34	0.91	4.18	4.53	0.92
CA4	10.54	10.72	0.98	7.50	7.51	1.00	1.99	1.80	1.10
CB3	5.02	4.98	1.01	15.30	16.47	0.93	4.83	4.22	1.14
CB4	5.17	5.39	0.96	7.60	6.82	1.11	2.92	2.61	1.12
CD2	3.39	3.50	0.97	4.40	20.15	0.22	7.77	8.69	0.89
CD3	6.64	6.77	0.98	6.60	17.18	0.38	5.38	4.32	1.24
CD4	9.66	10.04	0.96	7.80	7.87	0.99	4.80	1.90	2.53
CE2	2.73	3.27	0.83	12.50	18.60	0.67	10.45	6.80	1.54
CE3	6.45	6.75	0.96	21.00	22.40	0.94	9.54	5.86	1.63
CE4	8.36	8.94	0.94	12.20	11.47	1.06	6.42	2.74	2.34
CF2	3.81	3.72	1.03	14.00	16.16	0.87	6.66	5.11	1.30
$\bar{x}$ =			0.97			0.83			1.39
s =			0.05			0.27			0.54
cv =			5.5%			32.8%			38.8%

Table 6. Comparative analysis: negative (-) loading shear direction (cracking and yield points).

Panel	$\tau_{cr,exp}$ MPa	$\tau_{cr,th}$ MPa	$\frac{\tau_{cr,exp}}{\tau_{cr,th}}$	$\gamma_{cr,exp}$ $\times 10^{-3}$	$\gamma_{cr,th}$ $\times 10^{-3}$	$\frac{\gamma_{cr,exp}}{\gamma_{cr,th}}$	$\tau_{y,exp}$ MPa	$\tau_{y,th}$ MPa	$\frac{\tau_{y,exp}}{\tau_{y,th}}$	$\gamma_{y,exp}$ $\times 10^{-3}$	$\gamma_{y,th}$ $\times 10^{-3}$	$\frac{\gamma_{y,exp}}{\gamma_{y,th}}$
CA2	-2.60	-2.33	1.12	-0.19	-0.44	0.44	-3.50	-3.53	0.99	-3.96	-3.13	1.27
CA3	-2.63	-2.72	0.97	-0.18	-0.28	0.65	-6.61	-6.85	0.97	-4.80	-4.08	1.18
CA4	-2.81	-2.85	0.99	-0.18	-0.23	0.78	-10.10	-10.67	0.95	-5.60	-5.80	0.96
CB3	-2.10	-2.40	0.88	-0.13	-0.33	0.40	-4.37	-4.26	1.03	-4.20	-4.14	1.01
CB4	-1.85	-2.18	0.85	-0.13	-0.22	0.58	-4.65	-4.83	0.96	-5.30	-4.82	1.10
CD2	-2.12	-2.28	0.93	-0.11	-0.46	0.24	-2.80	-3.20	0.88	-2.67	-2.86	0.93
CD3	-2.06	-2.61	0.79	-0.13	-0.33	0.39	-5.35	-6.41	0.84	-2.70	-3.97	0.68
CD4	-2.50	-2.80	0.89	-0.16	-0.24	0.67	-8.59	-10.00	0.86	-3.10	-5.69	0.54
CE2	-1.78	-2.07	0.86	-0.18	-0.42	0.43	-2.68	-3.01	0.89	-1.88	-2.74	0.69
CE3	-1.96	-2.20	0.89	-0.12	-0.28	0.44	-5.10	-6.11	0.83	-1.98	-3.96	0.50
CE4	-1.98	-2.30	0.86	-0.14	-0.17	0.82	-7.60	-8.78	0.87	-2.30	-4.57	0.50
CF2	-1.97	-2.15	0.92	-0.21	-0.39	0.53	-3.38	-3.59	0.94	-2.30	-3.19	0.72
$\bar{x}$ =			0.91			0.53			0.92			0.84
s =			0.08			0.17			0.06			0.27
cv =			9.2%			32.6%			7.0%			32.0%

Table 7. Comparative analysis: negative (-) loading shear direction (peak point and ductility)

Panel	$\tau_{max,exp}$ MPa	$\tau_{max,th}$ MPa	$\frac{\tau_{max,exp}}{\tau_{max,th}}$	$\gamma_{max,exp}$ $\times 10^{-3}$	$\gamma_{max,th}$ $\times 10^{-3}$	$\frac{\gamma_{max,exp}}{\gamma_{max,th}}$	$\mu_{E\gamma,exp}$	$\mu_{E\gamma,th}$	$\frac{\mu_{E\gamma,exp}}{\mu_{E\gamma,th}}$
CA2	-3.91	-4.00	0.98	-26.40	-25.24	1.05	8.15	8.07	1.01
CA3	-6.83	-7.23	0.94	-15.60	-17.34	0.90	3.66	4.53	0.81
CA4	-10.20	-10.69	0.95	-7.70	-7.55	1.02	1.66	1.82	0.91
CB3	-5.10	-4.98	1.02	-14.00	-16.42	0.85	5.24	4.32	1.21
CB4	-5.18	-5.39	0.96	-12.00	-6.82	1.76	2.95	2.61	1.13
CD2	-3.33	-3.50	0.95	-7.00	-20.19	0.35	7.68	7.06	1.09
CD3	-5.92	-6.67	0.89	-4.40	-15.12	0.29	5.82	3.80	1.53
CD4	-9.10	-10.04	0.91	-4.50	-7.87	0.57	4.39	1.90	2.31
CE2	-3.60	-3.27	1.10	-19.00	-18.65	1.02	10.53	6.81	1.55
CE3	-6.29	-6.75	0.93	-18.00	-22.40	0.80	9.10	5.85	1.55
CE4	-8.26	-8.96	0.92	-11.40	-11.25	1.01	4.96	2.68	1.85
CF2	-3.63	-3.72	0.98	-14.70	-16.19	0.91	6.39	5.07	1.26
$\bar{x}$ =			0.96			0.88			1.35
s =			0.06			0.38			0.43
cv =			5.9%			43.3%			31.8%

The results in (**Table 4** to **Table 7**) show that the efficient RA-STM procedure predicts reasonably well both the cracking shear stress (τ_{cr}), and the yielding shear stress (τ_y) with ($\bar{x} > 0.9$), and a very acceptable degree of dispersion ($cv < 10\%$). It was also noticed that for the peak shear stress (τ_{max}) the predictions were better ($\bar{x} > 0.95$ and $cv < 6\%$)

As for the shear strain corresponding to the cracking shear stress (γ_{cr}), the results show that the efficient RA-STM tend to underestimate this parameter ($\bar{x} \approx 0.5$) and with a high degree of dispersion ($cv \approx 30\%$). This can be attributed to the difficulty to accurately measure this parameter experimentally, or to be obtained from the experimental $\tau_{45}^{\circ} - \gamma_{45}^{\circ}$ hysteretic loops with sufficient accuracy, as it is very small. This issue was also reported in previous studies [30], [40].

Regarding the shear strains corresponding to the yield shear stress (γ_y) and the peak shear stress (γ_{max}), the results show that these values are not very accurately predicted, as they tend to be underestimated ($0.85 < \bar{x} \leq 0.88$) and with a high degree of dispersion ($cv \geq 30\%$).

A smeared truss model is a discontinuous model that does not accurately account for the influence of the member's actual stiffness, even though it incorporates a smeared constitutive law for concrete in tension. In addition, the smeared truss model used in this study (the efficient RA-STM) did not incorporate cyclic constitutive laws that usually account for the materials' loss of stiffness throughout loading cycles, which impacts the global stiffness of the RC panel in the ultimate stage. This further explains the reason why at the ultimate stage, the predicted deformations tend to be underestimated by the model.

However, the previously referred parameters related to the shear strains (γ_y, γ_{max} , and γ_{cr}), can be viewed as not very crucial for the design or for a first check analysis.

Regarding the shear ductility factor ($\mu_{E\gamma}$), the results show that the model show an overestimation of the shear ductility of reference panels ($1.35 \leq \bar{x} < 1.4$) and a high degree of dispersion ($cv > 30\%$). This is mainly contributed to the reasons stated in the previous paragraph, but also due to the reason that the shear ductility factor is calculated with the shear strains at the ultimate stage (γ_u). As mentioned previously, the efficient RA-STM procedure exhibits difficulties to predict well the post-peak behavior of the envelope $\tau_{45}^{\circ} - \gamma_{45}^{\circ}$ curves, namely, the descending branch.

4 Conclusions and Suggestions

Shear walls and shell type RC structures can be viewed as a combination of smaller two-dimensional membrane elements, or panels.

It is possible to predict the global behavior of the referred structures under cyclic loadings by predicting the behavior of the membrane elements (panels).

In this study the envelope $\tau_{45}^{\circ} - \gamma_{45}^{\circ}$ curves of RC panels under cyclic shear were predicted using the monotonic version of the efficient RA-STM procedure, and then compared with the results from an experimental study reported in literature [3], [28].

This research has completed the following objectives set forth in chapter 1:

1. Validate the monotonic efficient RA-STM procedure for cyclic shear loading;
2. Predict the envelope $\tau_{45}^{\circ} - \gamma_{45}^{\circ}$ curves of RC panels under cyclic shear;
3. To validate the predictions from the monotonic efficient RA-STM for important key shear stresses for precheck analysis.

As a result of this research, an article was published in an international journal [41].

4.1 Research Conclusions

After analyzing the results obtained with the efficient RA-STM procedure, and comparing them with the experimental study, the following conclusions can be drawn:

1. The efficient RA-STM procedure is able to predict, with reasonably good agreement, the shape of the experimental envelope $\tau_{45}^{\circ} - \gamma_{45}^{\circ}$ curves of the reported RC panels under cyclic shear, at least until the peak shear stress is reached. Even though the model was previously proposed and checked for monotonic shear loading;
2. Important key features from the global experimental envelope curves response of the RC panels under cyclic shear was captured well in the theoretical curves, including the transition from the uncracked to the cracked stage and the yielding of the reinforcement;
3. The monotonic RA-STM procedure can reasonably predict several key shear stresses, which are crucial for the design stage. Namely, the cracking shear stress, the yielding shear stress, and the peak shear stress of the RC panels under cyclic shear;
4. The monotonic RA-STM procedure exhibited more difficulty to accurately predict the experimental values of the shear strains corresponding to the key shear stresses, and the model tends to underestimate their values. Nevertheless, this issue is not considered to be of much importance for this study, as the referred strains are not crucial for design or a precheck analysis;

5. Due to the stated in the previous point, the model showed high difficulty in predicting well the ductility of the RC panels under cyclic shear, as the model tends to overestimate its value. Unlike the drawback in predicting the strains, this issue is considered relevant, as ductility is considered a key parameter for the design, especially for structures located in seismic regions.

It can be concluded from the above-mentioned, that the monotonic efficient RA-STM procedure showed good results in predicting the envelope $\tau_{45}^{\circ} - \gamma_{45}^{\circ}$ curves for RC panels under cyclic shear and with a reasonable accuracy, in spite of it being a model for RC panels under monotonic shear loading. Hence, it is considered as a reliable model to use for practice, at least for predesign or precheck analysis.

In addition, it predicted reasonably well important key shear stresses, such as the cracking, yielding, and the maximum (peak) shear stresses, which are important parameters for design.

The drawback in predicting the shear ductility of RC panels, which tends to be overestimated, can be overlooked for a precheck analysis or a predesign; and the monotonic efficient RA-STM procedure can be used before more complex and reliable models for overall analysis are considered.

4.2 Suggestions for Future Developments

As the monotonic efficient RA-STM procedure was established to be a reliable model to predict only the envelope curves response for RC panels under cyclic shear, it can only be used for the predesign stage or precheck analysis. Hence, further research is suggested to extend the model and improve its results:

1. Transform the monotonic efficient RA-STM into a cyclic efficient RA-STM model, by implementing appropriate smeared constitutive laws for concrete and steel reinforcement for cycling loading, namely to account for the decrease of stiffness due to damage during the unloading-reloading cycles;
2. Extend both the monotonic and the new cyclic efficient RA-STM models for panels under cyclic shear built with special concretes (lightweight concrete, fiber-reinforced concrete, ultra-high-performance concrete, etc.) and different reinforcing systems (internal fiber reinforced polymer (FRP), external fiber reinforced polymer strips or wraps, etc.);
3. Implement the efficient RA-STM in a finite element software to create a computing tool able to analyses more general shear walls and shell type structures.

Bibliography

[1] T. T. C. Hsu and Y. L. Mo, “UNIFIED THEORY OF CONCRETE STRUCTURES,” 2010.

[2] K. Orakcal, L. M. Massone, and D. Ulugtekin, “A Hysteretic Constitutive Model for Reinforced Concrete Panel Elements,” *Int J Concr Struct Mater*, vol. 13, no. 1, p. 51, 2019, doi: 10.1186/s40069-019-0365-9.

[3] M. Mansour and T. T. C. Hsu, “Behavior of Reinforced Concrete Elements under Cyclic Shear. II: Theoretical Model,” *Journal of Structural Engineering*, vol. 131, no. 1, pp. 54–65, Jan. 2005, doi: 10.1061/(asce)0733-9445(2005)131:1(54).

[4] L. F. A. Bernardo, B. M. V. C. Filho, and B. Horowitz, “Refinement of the rotating-angle softened truss model with efficient solution procedure for RC membranes,” *Eng Struct*, vol. 213, Jun. 2020, doi: 10.1016/j.engstruct.2020.110552.

[5] N. S. Hoffman, “CONSTITUTIVE RELATIONSHIPS OF PRESTRESSED STEEL FIBER CONCRETE MEMBRANE ELEMENTS,” 2010.

[6] Vecchio F.J and Collins M.P, “Stress-strain characteristics of reinforced concrete in pure shear,” *IABSE Colloquium, Advanced Mechanics of Reinforced Concrete, Delft, Final Report; International Association of Bridge and Structural Engineering*, pp. 221–225, 1981, doi: 10.5169/seals-26889.

[7] Vecchio F.J and Collins M.P, “The Modified Compression-Field Theory for Reinforced Concrete Elements Subjected to Shear,” *ACI Journal Proceedings*, vol. 83, no. 2, pp. 219–231, 1986, doi: 10.14359/10416.

[8] Balakrishnan Samanaidu and Murray D.W, “Prediction of R/C Panel and Deep Beam Behavior by NLFEA,” *Journal of Structural Engineering*, vol. 114, no. 10, pp. 2323–2342, Oct. 1988, doi: 10.1061/(ASCE)0733-9445(1988)114:10(2323).

[9] Vecchio F.J and Collins M.P, “The Response of Reinforced Concrete to In-Plane Shear and Normal Stresses,” 1982.

[10] Crisfield Michael A and Wills John, “Analysis Of R/C Panels Using Different Concrete Models,” *J Eng Mech*, vol. 115, no. 3, pp. 578–597, Mar. 1989, doi: 10.1061/(ASCE)0733-9399(1989)115:3(578).

[11] Stevens N.J, Collins M.P., and Uzumeri S M, “Reinforced concrete subjected to reversed cyclic shear--Experiments and constitutive model,” *ACI Struct J*, vol. 88, no. 2, 1991, doi: 10.14359/2880.

[12] N. Ohmori, T. Takahashi, T. Haruji, N. Inoue, K. Kurihara, and S. Watanabe, “Experimental Studies on Nonlinear Behaviours of Reinforced Concrete Panels Subjected

to Cyclic In-plane Shear," *Journal of Structural and Construction Engineering (Transactions of AIJ)*, vol. 403, pp. 105–118, Sep. 1989, doi: 10.3130/aijsx.403.0_105.

[13] Hsu TTC and Pang Xiao-Bo David, "Behavior of Reinforced Concrete Membrane Elements in Shear," *ACI Struct J*, vol. 92, no. 6, 1995, doi: 10.14359/9661.

[14] Hsu TTC and Belarbi Abdeldjelil, "Constitutive Laws of Softened Concrete in Biaxial Tension Compression," *ACI Struct J*, vol. 92, no. 5, 1995, doi: 10.14359/907.

[15] Hsu TTC and Belarbi Abdeldjelil, "Constitutive Laws of Concrete in Tension and Reinforcing Bars Stiffened By Concrete," *ACI Struct J*, vol. 91, no. 4, 1994, doi: 10.14359/4154.

[16] Hsu TTC and Zhang Li-Xin, "Nonlinear Analysis of Membrane Elements by Fixed-Angle Softened-Truss Model," *ACI Struct J*, vol. 94, no. 5, 1997, doi: 10.14359/498.

[17] Hsu TTC and Pang Xiao-Bo David, "Fixed Angle Softened Truss Model for Reinforced Concrete," *ACI Struct J*, vol. 93, no. 2, 1996, doi: 10.14359/1452.

[18] Zhang Li-Xin and Hsu TTC, "Behavior and Analysis of 100 MPa Concrete Membrane Elements," *Journal of Structural Engineering*, vol. 124, no. 1, pp. 24–34, Jan. 1998, doi: 10.1061/(ASCE)0733-9445(1998)124:1(24).

[19] Ayoub Amir and Filippou Filip, "Nonlinear Finite-Element Analysis of RC Shear Panels and Walls," *Journal of Structural Engineering*, vol. 124, no. 3, pp. 298–308, Mar. 1998, doi: 10.1061/(ASCE)0733-9445(1998)124:3(298).

[20] Vecchio FJ, "Reinforced Concrete Membrane Element Formulations," *Journal of Structural Engineering*, vol. 116, no. 3, pp. 730–750, Mar. 1990, doi: 10.1061/(ASCE)0733-9445(1990)116:3(730).

[21] Kaufmann walter and Marti Peter, "Structural Concrete: Cracked Membrane Model," *Journal of Structural Engineering*, vol. 124, no. 12, pp. 1467–1475, Dec. 1998, doi: 10.1061/(ASCE)0733-9445(1998)124:12(1467).

[22] S. J. Foster and P. Marti, "Cracked Membrane Model: Finite Element Implementation," *Journal of Structural Engineering*, vol. 129, no. 9, pp. 1155–1163, Sep. 2003, doi: 10.1061/(ASCE)0733-9445(2003)129:9(1155).

[23] Vecchio F.J, "Disturbed Stress Field Model for Reinforced Concrete: Formulation," *Journal of Structural Engineering-asce - J STRUCT ENG-ASCE*, vol. 126, Sep. 2000, doi: 10.1061/(ASCE)0733-9445(2000)126:9(1070).

[24] Vecchio F.J, "Disturbed Stress Field Model for Reinforced Concrete: Implementation," *Journal of Structural Engineering*, vol. 127, no. 1, pp. 12–20, Jan. 2001, doi: 10.1061/(ASCE)0733-9445(2001)127:1(12).

[25] B. Belletti, R. Cerioni, and I. Iori, “Physical Approach for Reinforced-Concrete (PARC) Membrane Elements,” *Journal of Structural Engineering*, vol. 127, no. 12, pp. 1412–1426, 2001, doi: 10.1061/(ASCE)0733-9445(2001)127:12(1412).

[26] Zhu RRH and Hsu TTC, “Softened Membrane Model for Reinforced Concrete Elements in Shear,” *ACI Struct J*, vol. 99, no. 4, 2002, doi: 10.14359/12115.

[27] Zhu RRH, Hsu TTC, and Lee JY, “Rational Shear Modulus for Smeared-Crack Analysis of Reinforced Concrete,” *ACI Struct J*, vol. 98, no. 4, 2001, doi: 10.14359/10287.

[28] M. Mansour and T. T. C. Hsu, “Behavior of Reinforced Concrete Elements under Cyclic Shear. I: Experiments,” *Journal of Structural Engineering*, vol. 131, no. 1, pp. 44–53, Jan. 2005, doi: 10.1061/(asce)0733-9445(2005)131:1(44).

[29] L. F. A. Bernardo, B. M. V. de Carvalho Filho, and B. Horowitz, “Predicting the behavior of FRP-strengthened RC membrane elements with efficient rotating-angle softened truss model procedure,” *Mater Struct*, vol. 54, no. 1, p. 42, 2021, doi: 10.1617/s11527-021-01631-y.

[30] L. F. A. Bernardo, B. M. V. C. Filho, and B. Horowitz, “Refinement of the rotating-angle softened truss model with efficient solution procedure for RC membranes,” *Eng Struct*, vol. 213, p. 110552, 2020, doi: https://doi.org/10.1016/j.engstruct.2020.110552.

[31] Greene Gray and Belarbi Abdeldjelil, “Model for Reinforced Concrete Members under Torsion, Bending, and Shear. I: Theory,” *J Eng Mech*, vol. 135, no. 9, pp. 961–969, Sep. 2009, doi: 10.1061/(ASCE)0733-9399(2009)135:9(961).

[32] L. F. A. Bernardo, J. M. A. Andrade, and N. C. G. Nunes, “Generalized softened variable angle truss-model for reinforced concrete beams under torsion,” *Mater Struct*, vol. 48, no. 7, pp. 2169–2193, 2015, doi: 10.1617/s11527-014-0301-z.

[33] Mansour Mohamad, Lee Jung-Yoon, and Hsu Thomas T. C., “Cyclic Stress-Strain Curves of Concrete and Steel Bars in Membrane Elements,” *Journal of Structural Engineering*, vol. 127, no. 12, pp. 1402–1411, Dec. 2001, doi: 10.1061/(ASCE)0733-9445(2001)127:12(1402).

[34] Jeng Chyuan-Hwan and Hsu Thomas T.C., “A softened membrane model for torsion in reinforced concrete members,” *Eng Struct*, vol. 31, no. 9, pp. 1944–1954, Sep. 2009, doi: 10.1016/j.engstruct.2009.02.038.

[35] T. Ji, “A new algorithm for the rotating-angle, softened-truss model of reinforced concrete elements,” *Magazine of Concrete Research*, vol. 57, no. 6, pp. 353–360, 2005, doi: 10.1680/macr.2005.57.6.353.

[36] D. Petersen, T. Hsu, A. Belarbi, and X. Pang, “A Universal Panel Tester,” *J Test Eval*, vol. 23, no. 1, p. 41, 1995, doi: 10.1520/JTE10397J.

[37] “Universal Element Tester | Structural Research Laboratory.” http://structurallab.egr.uh.edu/le/universal-element-tester (accessed Mar. 25, 2022).

[38] Mohamad Mansour, “Behavior of reinforced concrete elements under cyclic shear: Experiments to theory,” PhD dissertation, University of Houston, Houston, 2001.

[39] “EN 1992-1-1: Eurocode 2: Design of concrete structures - Part 1-1: General rules and rules for buildings,” 2004.

[40] L. Bernardo, B. Filho, and B. Horowitz, “Predicting the behavior of prestressed concrete membrane elements by refined rotating-angle softened-truss model with efficient solution procedure,” *Structural Concrete*, vol. 21, Jan. 2020, doi: 10.1002/suco.201900481.

[41] L. Bernardo and S. Sadieh, “A Monotonic Smeared Truss Model to Predict the Envelope Shear Stress—Shear Strain Curve for Reinforced Concrete Panel Elements under Cyclic Shear,” *Applied Mechanics*, vol. 2, no. 1, pp. 174–194, Mar. 2021, doi: 10.3390/applmech2010011.

[42] MathWorks, “MATLAB_2018a.” 2018.

APPENDICES

Appendix I

MATLAB Code for the Efficient RA-STM Procedure

Script to initiate the Efficient RA-STM Procedure [42]

```
%////////////////////////////////////////////////////////////////////////
/
% RA-STM - ROTATING ANGLE SOFTENED TRUSS MODEL - REINFORCED CONCRETE          /
%////////////////////////////////////////////////////////////////////////
/

% INICIO ////////////////////////////////////////////////////////////////
clear all; clc;

% DADOS DE ENTRADA //////////////////////////////////////////////////////
DADOS_INICIAIS; tic;

% CÁLCULO DA ESTIMATIVA INICIAL (MCTM) //////////////////////////////////
alfaD1 = (lsqnonlin(@(alfaD) MCTM_PLACA(alfaD),0.01,[],0))*180/pi;

% SOLUÇÃO ///////////////////////////////////////////////////////////////
COMP_PLACA;

% CURVAS TENSÃO-DEFORMAÇÃO //////////////////////////////////////////////
toc; PLOT_PLACA;
```

Function to choose the panels

```
function DADOS_INICIAIS

%////////////////////////////////////////////////////////////////////////
% SELEÇÃO DA PLACA / INTRODUÇÃO DOS DADOS INICIAIS                      /
%////////////////////////////////////////////////////////////////////////

disp('Placas de MANSOUR e HSU (2005)');
disp(' ');
disp('Selecione os dados iniciais:');
disp(' ');
disp('Placas de Betão Armado solicitadas com ALFA2=45°');
disp('1  - CA2(+)Loading');
disp('2  - CA2(-)Loading');
disp('3  - CA3(+)Loading');
disp('4  - CA3(-)Loading');
disp('5  - CA4(+)Loading');
disp('6  - CA4(-)Loading');
disp('7  - CB3(+)Loading');
disp('8  - CB3(-)Loading');
disp('9  - CB4(+)Loading');
disp('10 - CB4(-)Loading');
disp(' ');
disp('Placas de Betão Armado solicitadas com ALFA2=68.2°');
disp('11 - CD2(+)Loading');
disp('12 - CD2(-)Loading');
disp('13 - CD3(+)Loading');
disp('14 - CD3(-)Loading');
disp('15 - CD4(+)Loading');
disp('16 - CD4(-)Loading');
disp(' ');
disp('Placas de Betão Armado solicitadas com ALFA2=90°');
disp('17 - CE2(+)Loading');
disp('18 - CE2(-)Loading');
disp('19 - CE3(+)Loading');
disp('20 - CE3(-)Loading');
disp('21 - CE4(+)Loading');
disp('22 - CE4(-)Loading');
disp(' ');
disp('Placa de Betão Armado solicitada com ALFA2=79.8°');
```

```
disp('23 - CF2(+)Loading');
disp('24 - CF2(-)Loading');
disp(' ');
disp('0 - Sair');
disp(' ');
IND = input('Escolha uma opção: ');

if IND >= 0 & IND <= 24
    switch IND
        case 1
            CA2_plus_MANSOUR_e_HSU;
        case 2
            CA2_minus_MANSOUR_e_HSU;
        case 3
            CA3_plus_MANSOUR_e_HSU;
        case 4
            CA3_minus_MANSOUR_e_HSU;
        case 5
            CA4_plus_MANSOUR_e_HSU;
        case 6
            CA4_minus_MANSOUR_e_HSU;
        case 7
            CB3_plus_MANSOUR_e_HSU;
        case 8
            CB3_minus_MANSOUR_e_HSU;
        case 9
            CB4_plus_MANSOUR_e_HSU;
        case 10
            CB4_minus_MANSOUR_e_HSU;
        case 11
            CD2_plus_MANSOUR_e_HSU;
        case 12
            CD2_minus_MANSOUR_e_HSU;
        case 13
            CD3_plus_MANSOUR_e_HSU;
        case 14
            CD3_minus_MANSOUR_e_HSU;
        case 15
            CD4_plus_MANSOUR_e_HSU;
        case 16
            CD4_minus_MANSOUR_e_HSU;
        case 17
```

```
            CE2_plus_MANSOUR_e_HSU;
        case 18
            CE2_minus_MANSOUR_e_HSU;
        case 19
            CE3_plus_MANSOUR_e_HSU;
        case 20
            CE3_minus_MANSOUR_e_HSU;
        case 21
            CE4_plus_MANSOUR_e_HSU;
        case 22
            CE4_minus_MANSOUR_e_HSU;
        case 23
            CF2_plus_MANSOUR_e_HSU;
        case 24
            CF2_minus_MANSOUR_e_HSU;
        case 0
            error('SCRIPT INTERROMPIDO!')
            clc
    end
else
    disp(' ');
    disp('O VALOR INTRODUZIDO NÃO É VÁLIDO!');
    disp(' ');
    DADOS_INICIAIS
end
end
```

Example of experimental data: Panel CA3 (Positive Loading)

```
function CA3_plus_MANSOUR_e_HSU

%////////////////////////////////////////////////////////////////////////
% DADOS EXPERIMENTAIS DA PLACA CA3(+)Loading - MANSOUR E HSU (2005)       /
%////////////////////////////////////////////////////////////////////////

global roL roT Es fLy fTy Ec fcr ecr fcm e0 tal sigL sigT eLy eTy  esu ecu
global sig1 mLT mL mT
global  e_plot  sigmaD_plot  eR_plot  aco_plot  eL_plot  eT_plot  fL_plot  fT_plot
sigmaR_plot
global alfa_plot tal_plot gama_plot tal_Teo gama_Teo a b c eRaux_plot

%////////////////////////////////////////////////////////////////////////
% DADOS INICIAIS                                                         /
%////////////////////////////////////////////////////////////////////////

% Taxas de armadura:
roL = 0.017;
roT = 0.017;

% Propriedades mecânicas dos aços:
Es  = 212700;            %Módulo de elasticidade do aço (MPa)
fLy = 425.4;             %Tensão de cedência da armadura longitudinal (MPa)
fTy = 425.4;             %Tensão de cedência da armadura transversal (MPa)
esu = 25;                %Extensão última das armaduras (1/1000)

% Propriedades mecânicas do betão:
fcm = 44.5;              %Resistência média do betão(MPa)
Ec = 25849;              %Módulo de elast. do betão (MPa)
e0  = -2.4;              %Extensão do betão correspondente ao pico (1/1000)
fcr = 4.15;              %Resistência à tração do betão (MPa)
ecr = 0.08;              %Extensão correspondente a fcr - Belarbi e Hsu (1994)
  if fcm <= 58;          %Extensão última do betão (1/1000)
    ecu = -3.5;
  else
    ecu = -(2.8 + 27 * ((98-fcm)/100)^4);
  end

% Solicitações no elemento de betão armado (L-T):
tal  = 1;                      %Tensão tangencial (MPa)
sigL = 0;                      %Tensão de tração longitudinal (MPa)
```

```
sigT = 0;                          %Tensão de compressão transversal (Mpa)

%////////////////////////////////////////////////////////////////////////////
% CÁLCULOS PRELIMINARES                                                     /
%////////////////////////////////////////////////////////////////////////////

eLy  = fLy/Es*1000;
eTy  = fTy/Es*1000;
sig1 = (sigL + sigT)/2 + sqrt(((sigL - sigT)/2)^2 + tal^2);
mLT  = tal/sig1;
mL   = sigL/sig1;
mT   = sigT/sig1;

%////////////////////////////////////////////////////////////////////////////
% DADOS CURVAS EXPERIMENTAIS E TEÓRICAS                                     /
%////////////////////////////////////////////////////////////////////////////

e_plot      = 0;
sigmaD_plot = 0;
sigmaR_plot = 0;
eR_plot     = 0;
eRaux_plot  = 0;
aco_plot    = 0;
eL_plot     = 0;
eT_plot     = 0;
fL_plot     = 0;
fT_plot     = 0;
alfa_plot   = 0;
tal_plot     = [0; 2.76; 6.7; 7.18; 7.3; 7.47; 7.55; 7.57; 7.57; 7.59; 7.11;
6.83;
               6.37; 6.17; 5.86; 5.3; 4.54; 3.98; 2.62];
gama_plot    = [0; 0.19; 4.5; 5.9; 7.1; 8.8; 10.1; 12; 13.2; 15.7; 16.2; 17.1;
17.5;
               18.2; 19.8; 20.8; 22.1; 23; 23.6];
tal_Teo     = 0;
gama_Teo    = 0;

%Legenda
a = 'CA3(+) Exp.';
b = 'Eff. RA-STM';
c = '-';
end
```

Function to compute the initial estimates (MCTM)

```
function F = MCTM_PLACA(alfaD)

%////////////////////////////////////////////////////////////////////////////
% COMPORTAMENTO LINEAR DDA PLACA (MCTM) - ESTIMATIVAS INICIAIS PARA O RA-STM /
%////////////////////////////////////////////////////////////////////////////
global roL roT Es Ec eL eT eD sig1 mLT mL mT

% Equações de equilíbrio (Eqs. 2.53-2.55):
eL=(mL+mLT*cot(alfaD))/(Es*roL)*0.001*sig1 ;
eT=(mT+mLT*tan(alfaD))/(Es*roT)*0.001*sig1;
eD=-mLT/(Ec*sin(alfaD)*cos(alfaD))*0.001*sig1;

% Eq. não linear (Eq. 2.5):
F = (eL-eD)/(eT-eD)-(tan(alfaD))^2;

end
```

Functions for the Efficient RA-STM Procedure

```
function COMP_PLACA
%////////////////////////////////////////////////////////////////////////
% COMPORTAMENTO CARGA-DEFORMÇÃO DA PLACA (RASTM_PAINEL)                  /
%////////////////////////////////////////////////////////////////////////
global eL eT eD sigmaD eR fL fT sigmaR esu ecu d
global ED SIGMAD TAL GAMA EL ET FL FT ALFAD ER tal_plot gama_plot SIGMAR D

% Estimativa inicial com base no MCTM:
x(1) = eL*1000;
x(2) = eT*1000;
ed1  = eD*1000;

% Número máximo de pontos e tamanho do passo:
pontos = 1000;
passo  = 4/pontos;

% Cálculo comportamento tensão-deformção:
for i = 1:pontos

    options = optimset('TolX',10^-10,'TolFun',10^-10);
    x = lsqnonlin(@(x) RASTM_PLACA(x,ed1-passo*i),x,[0,0],[],options);

    % Criar vetores de comportamento:
    ED(i)    = ed1 - passo*i;
    SIGMAD(i)= sigmaD;
    SIGMAR(i)= sigmaR;
    COS      = (x(2)-ED(i))/(eR-ED(i));
    SIN      = (x(1)-ED(i))/(eR-ED(i));
    TAL(i)   = (-SIGMAD(i)+SIGMAR(i))*sqrt(COS*SIN);
    GAMA(i)  = 2*(eR-ED(i))*sqrt(COS*SIN);
    EL(i)    = x(1);
    ET(i)    = x(2);
    FL(i)    = fL;
    FT(i)    = fT;
    ALFAD(i) = -atan(sqrt(SIN/COS))*180/pi;
    ER(i) = EL(i) + ET(i) - ED(i);
    D(i) = d;

    % Critérios de paragem (betão normal e de alta resistência)
    if - ED(i) >= - ecu || EL(i) >= esu || ET(i) >= esu ;
```

```
        break
    end

end
MAXTAL = max(TAL);
MAXGAMAj = GAMA(find(TAL==max(TAL)));
MAXTAL_PLOT = max(tal_plot);
MAXGAMA_PLOT = gama_plot(find(tal_plot==max(tal_plot)));
disp('Valores últimos (máximos) são:');
fprintf('Tau_u,th: %f kN.m\n',MAXTAL);
fprintf('Gama_u,th: %f rad/m\n',MAXGAMAj);
fprintf('Tau_u,exp: %f kN.m\n',MAXTAL_PLOT);
fprintf('Gama_u,exp: %f rad/m\n',MAXGAMA_PLOT);
fprintf('\n')


end
```

```
function F = RASTM_PLACA(x,ed1)

%////////////////////////////////////////////////////////////////////////
% COMPORTAMENTO NÃO-LINEAR DA PLACA (RA-STM)                            /
%////////////////////////////////////////////////////////////////////////

global roL roT Es fcm fLy fTy e0 mLT mL mT sigmaD csi eR fL fT eLy eTy sigmaR
global fcr ecr sigL sigT d

% CÁLCULOS INICIAIS ////////////////////////////////////////////////////

% Princípio da Invariância (Eq. 2.8):
eR = x(1) + x(2) - ed1;

% Coeficiente de Amolecimento (Eqs. 2.15-2.18):
R = 5.8/(sqrt(fcm));
```

```
if   R <= 0.9
    R_linha = R;
else
    R_linha = 0.9;
end

n = (roT*fTy-sigT)/(roL*fLy-sigL);
if   n <= 1
    n_linha = n;
else
    n_linha = 1/n;
end

csi = R_linha/(sqrt(1+((0.4*eR)/n_linha)));


% Relação constitutiva do betão à compressão (Eq. 2.12) com fator de dano d:
d = 1; % d = 1 - 0.4*ed1/e0;

if ed1 > csi*e0
    sigmaD = -d*csi*fcm*(2*(ed1/(csi*e0))-(ed1/(csi*e0))^2);
else
    sigmaD = -d*csi*fcm*(1-((ed1/(csi*e0)-1)/((4/csi)-1))^2);
end


% Relação constitutiva do aço (Eqs. 2.23-2.26):

% Armadura Longitudinal
BL  = (1/roL)*(fcr/fLy)^1.5;
enL = eLy*10^-3*(0.93-2*BL);

if x(1)*10^-3 <= enL
    fL = x(1)*10^-3*Es;
else
    fL = fLy*((0.91-2*BL)+(0.02+0.25*BL)*(x(1)/eLy));
end

% Armadura Transversal
BT  = (1/roT)*(fcr/fTy)^1.5;
enT = eTy*10^-3*(0.93-2*BT);
```

```
if x(2)*10^-3 <= enT
    fT  = x(2)*10^-3*Es;
else
    fT = fTy*((0.91-2*BT)+(0.02+0.25*BT)*(x(2)/eTy));
end

% Relação constitutiva do betão à tração

sigmaR = fcr*(ecr/(eR+ecr))^0.4;

% Tensão principal de tracção (Eqs. 2.40-2.43):
A = mL*mT - mLT^2;
B = mL*(sigmaR + roT*fT) + mT*(sigmaR + roL*fL);
C = (sigmaR + roT*fT)*(sigmaR + roL*fL);
sigma1 = (1/(2*A))*(B-sqrt(B^2-4*A*C));


%COMPORTAMENTO NÃO LINEAR RA-STM ////////////////////////////////////////

% Sistema de equações não-linear (Eq. 2.57):
F(1)  =  sigmaD*(x(1)-ed1)/(eR-ed1)-mT*sigma1+roT*fT  +  sigmaR*(x(2)-ed1)/(eR-
ed1);
F(2)  =  sigmaD*(x(2)-ed1)/(eR-ed1)-mL*sigma1+roL*fL  +  sigmaR*(x(1)-ed1)/(eR-
ed1);


end
```

Function to plot the curves

```
function PLOT_PLACA

%////////////////////////////////////////////////////////////////////////
% IMPRESSÃO DAS CURVAS DE COMPORTAMENTO TENSÃO-DEFORMAÇÃO DA PLACA       /
%////////////////////////////////////////////////////////////////////////

global ED SIGMAD TAL GAMA EL ET FL FT ER SIGMAR
global e_plot sigmaD_plot eL_plot eT_plot fL_plot fT_plot
global tal_plot gama_plot tal_Teo gama_Teo sigmaR_plot a b c eRaux_plot

% DADOS INICIAIS ////////////////////////////////////////////////////////

% Opção:
disp('1 - Curva tensão-deformação de compressão do betão');
disp('2 - Curva tensão-deformação de tração do betão');
disp('3 - Curva tensão-deformação da armadura longitudinal');
disp('4 - Curva tensão-deformação da armadura transversal');
disp('5 - Curva tensão-deformação de corte da placa');
disp(' ');
disp('6 - Voltar ao inicio');
disp('0 - Sair');
disp(' ');
IND = input('Escolha uma opção: ');

% IMPRESSÃO DAS CURVAS //////////////////////////////////////////////////

while IND > 0
    switch IND

        case 1
            % 1 - Curva tensão-deformação de compressão do betão
            hold on
            plot(-e_plot,-sigmaD_plot,'-rs','LineWidth',2,'MarkerSize',7)
            plot(-[0 ED],-[0 SIGMAD],'--b','LineWidth',2)%1.5)

            % Títulos
            xlabel('\epsilon_D (1/1000)');
            ylabel('\sigma_D (MPa)');
            legend(a,...
```

```
        b,'Location','southeast');
    grid on
    hold off

case 2
    % 2 - Curva tensão-deformação de tração do betão
    hold on
    plot(eRaux_plot,sigmaR_plot,'-rs','LineWidth',2,'MarkerSize',7)
    plot([0 ER],[0 SIGMAR],'--b','LineWidth',2)%1.5)

    % Títulos
    xlabel('\epsilon_R (1/1000)');
    ylabel('\sigma_R (MPa)');
    legend(a,...
        b,'Location','southeast');
    grid on
    hold off

case 3
    % 3 - Curva tensão-deformação da armadura longitudinal
    hold on
    plot(eL_plot,fL_plot,'--rs','LineWidth',2,'MarkerSize',7)
    plot([0 EL],[0 FL],'-g','LineWidth',2)

    % Títulos
    xlabel('\epsilon_L(1/1000)');
    ylabel('f_L (MPa)');
    legend(a,...
        b,'Location','southeast');
    grid on
    hold off


case 4
    % 4 - Curva tensão-deformação da armadura transversal
    hold on
    plot(eT_plot,fT_plot,'--rs','LineWidth',2,'MarkerSize',7)
    plot([0 ET],[0 FT],'-g','LineWidth',2)

    % Títulos
    xlabel('\epsilon_T (1/1000)');
    ylabel('f_T (MPa)');
```

```
            legend(a,...
                b,'Location','southeast');
            grid on
            hold off


        case 5
            % 5 - Curva tensão-deformação de corte da placa
            hold on
            plot(gama_plot,tal_plot,'-rs','LineWidth',2,'MarkerSize',7)
            plot([0 GAMA],[0 TAL],'--b','LineWidth',2)
            plot (gama_Teo, tal_Teo,'-k','LineWidth',1)

            % Títulos
            xlabel('\gamma_4_5_° (1/1000)');
            ylabel('\tau_4_5_° (MPa)');
            legend(a,...
                b,...
                c,'Location','southeast');
            grid on
            hold off


        case 6
            if IND == 6
                inicio;
                break
            end
end
    disp(' ');
    IND = input('Escolha uma opção: ');

end
end
```

Appendix II

Theoretical predictions for the envelop curves

Panel CA2 (Mansour and Hsu, 2005) - Positive loading

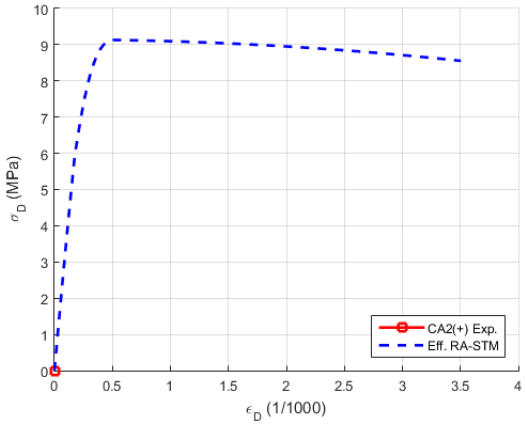

Curve $\sigma_D - \varepsilon_D$

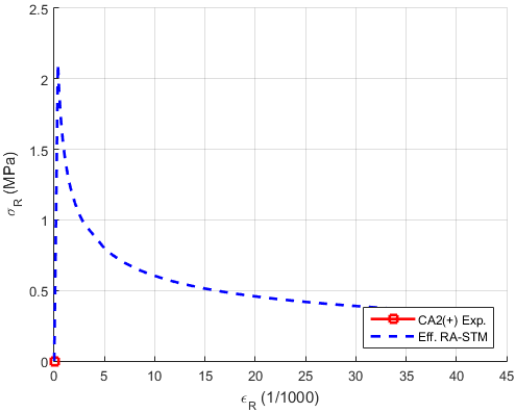

Curve $\sigma_R - \varepsilon_R$

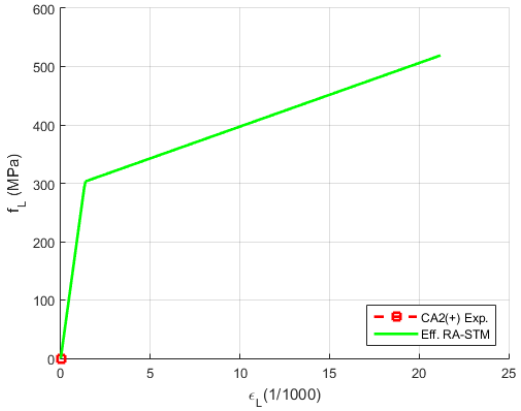

Curve $f_L - \varepsilon_L$

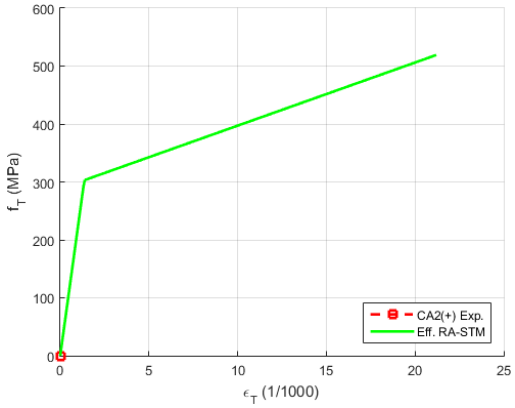

Curve $f_T - \varepsilon_T$

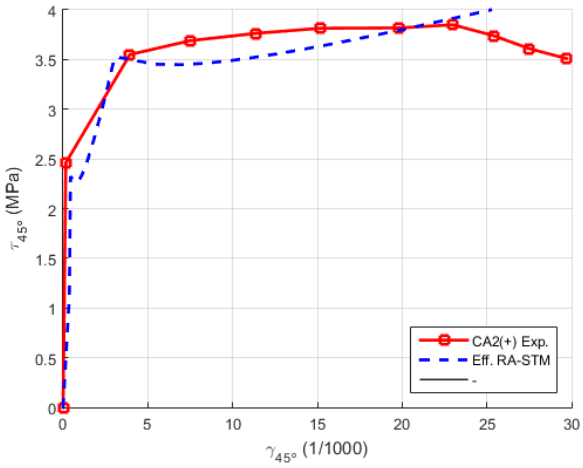

Curve $\tau_{45°} - \gamma_{45°}$

Panel CA2 (Mansour and Hsu, 2005) - Negative loading (1)

(1) Absolute values

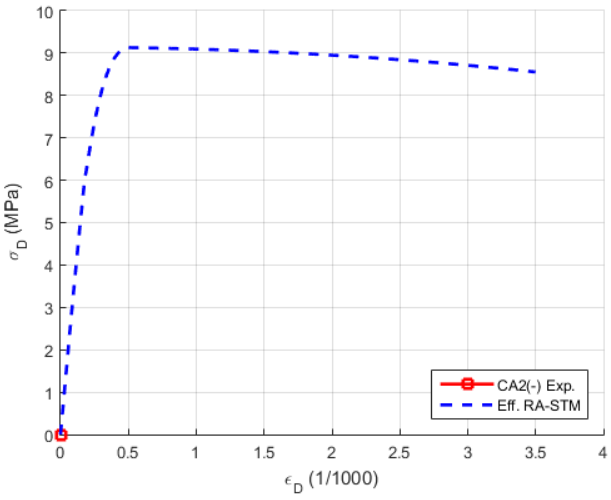

Curva $\sigma_D - \varepsilon_D$

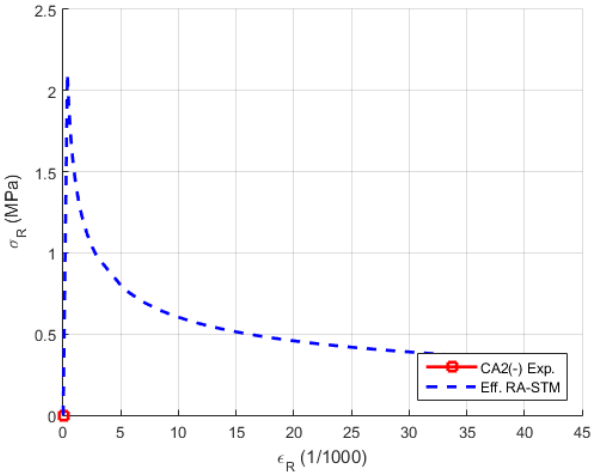

Curva $\sigma_R - \varepsilon_R$

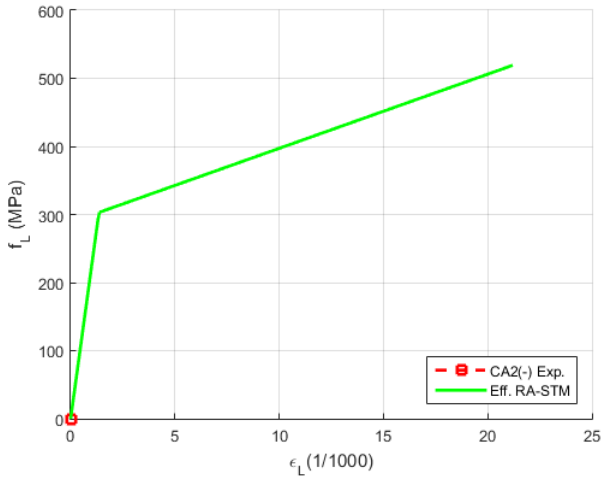

Curva $f_L - \varepsilon_L$

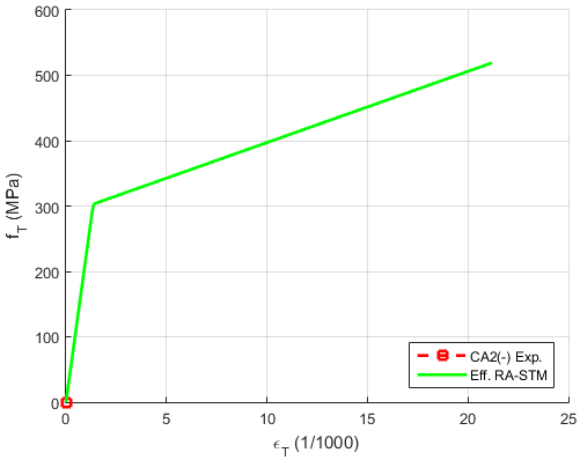

Curva $f_T - \varepsilon_T$

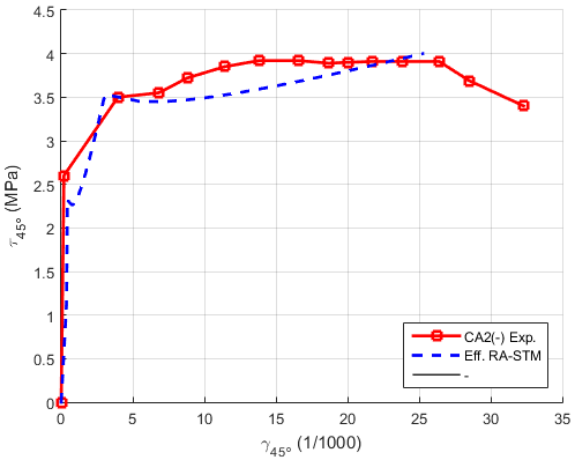

Curve $\tau_{45^\circ} - \gamma_{45^\circ}$

Panel CA3 (Mansour and Hsu, 2005) - Positive loading

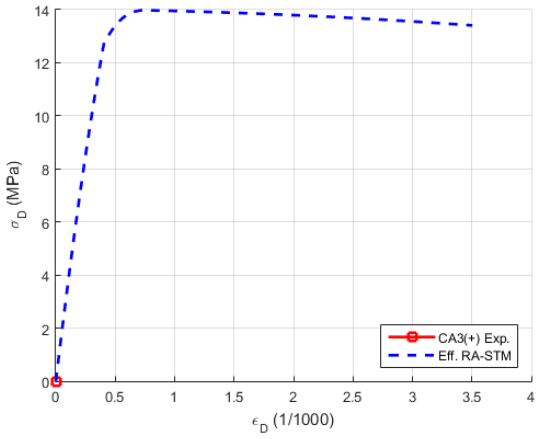

Curva $\sigma_D - \varepsilon_D$

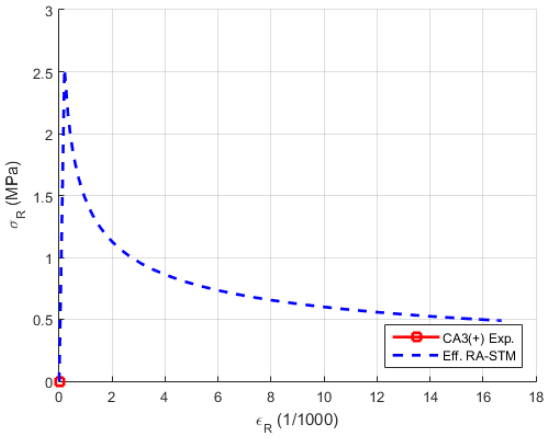

Curva $\sigma_R - \varepsilon_R$

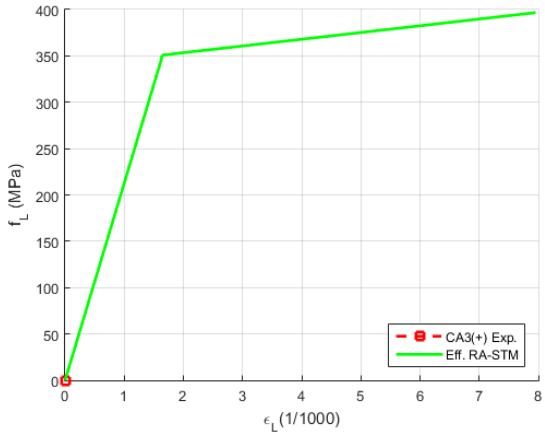

Curva $f_L - \varepsilon_L$

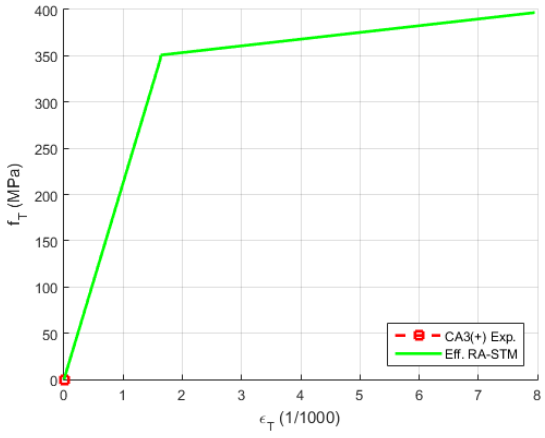

Curva $f_T - \varepsilon_T$

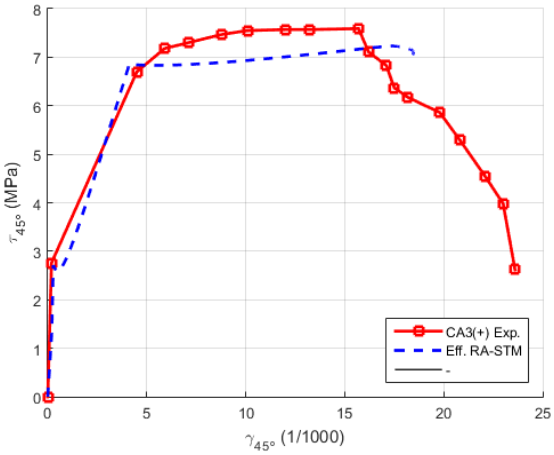

Curve $\tau_{45°} - \gamma_{45°}$

Panel CA3 (Mansour and Hsu, 2005) - Negative loading (1)

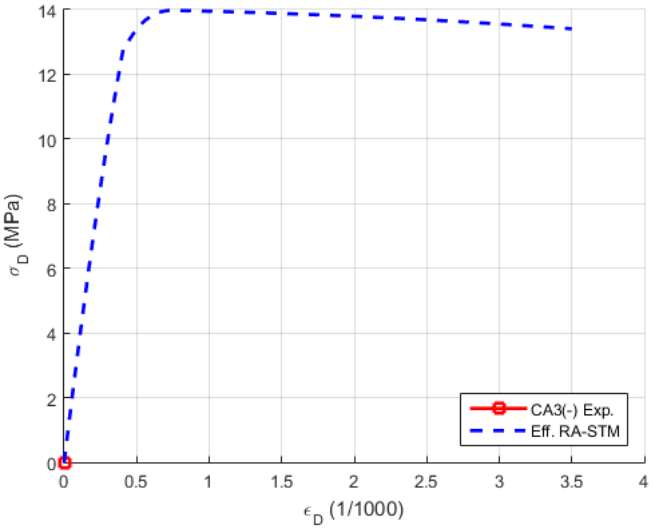

Curva $\sigma_D - \varepsilon_D$

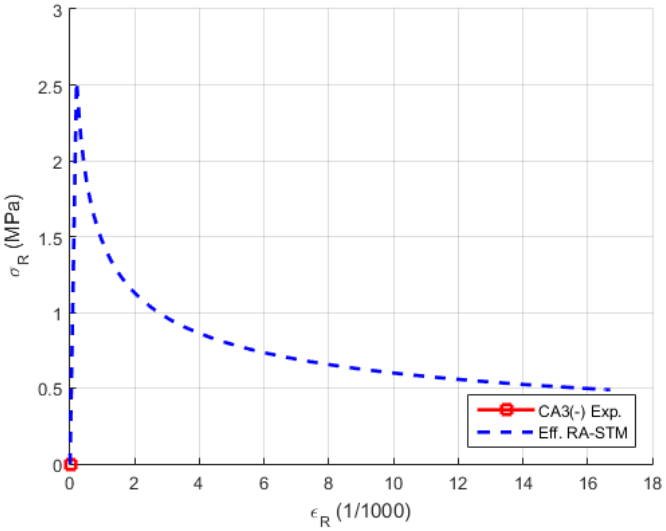

Curva $\sigma_R - \varepsilon_R$

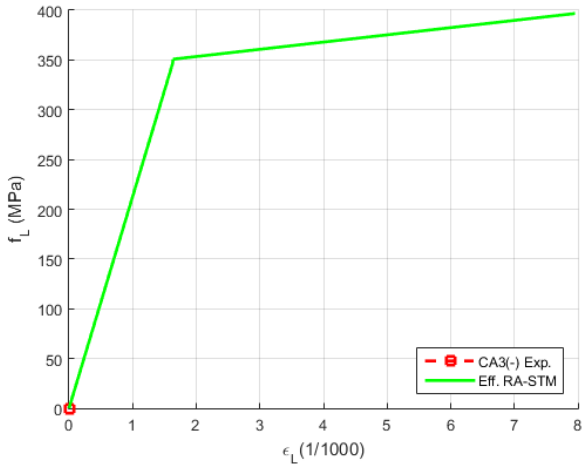

Curva $f_L - \varepsilon_L$

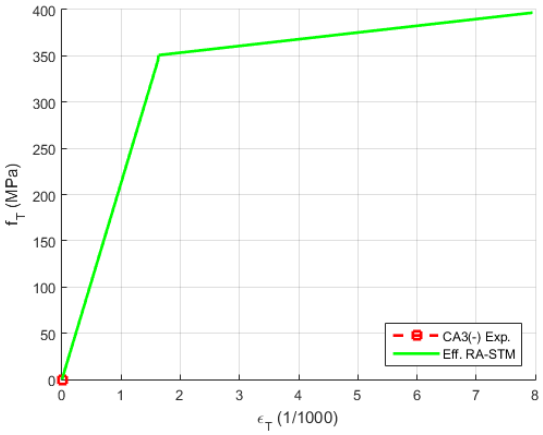

Curva $f_T - \varepsilon_T$

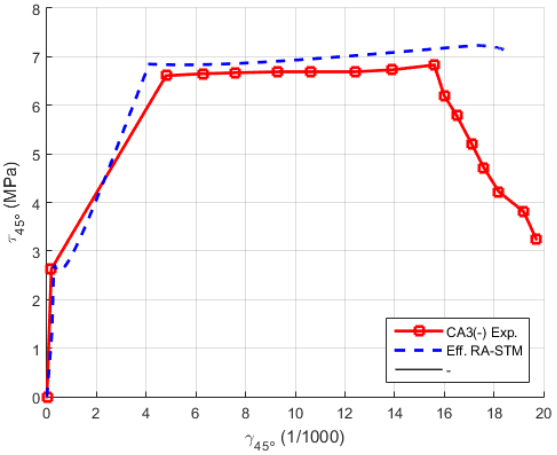

Curve $\tau_{45^\circ} - \gamma_{45^\circ}$

Panel CA4 (Mansour and Hsu, 2005) - Positive loading

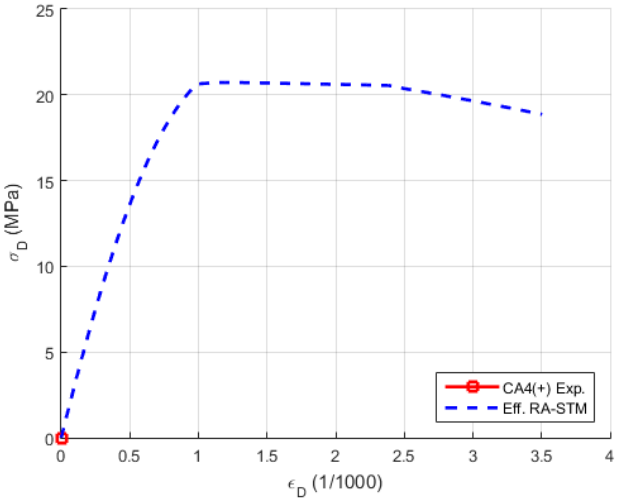

Curva $\sigma_D - \varepsilon_D$

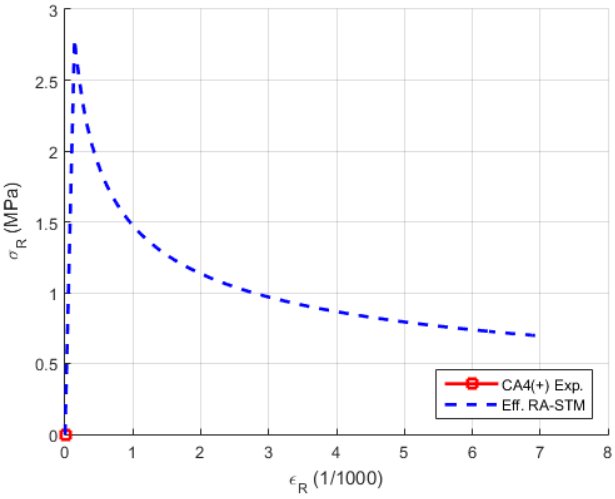

Curva $\sigma_R - \varepsilon_R$

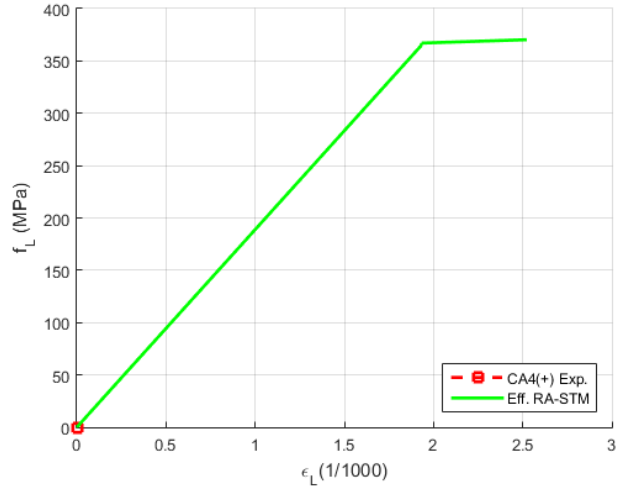

Curva $f_L - \varepsilon_L$

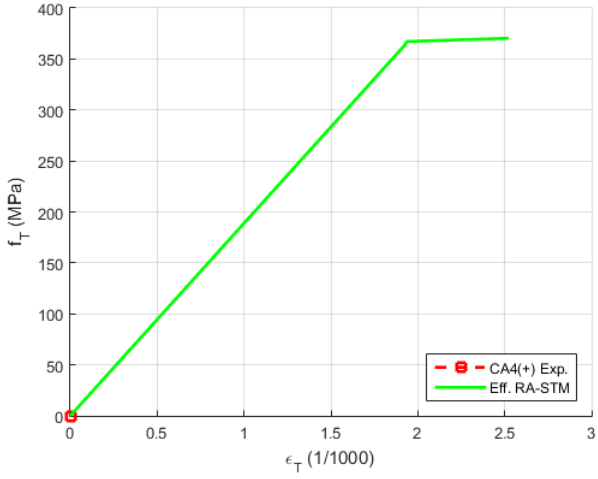

Curva $f_T - \varepsilon_T$

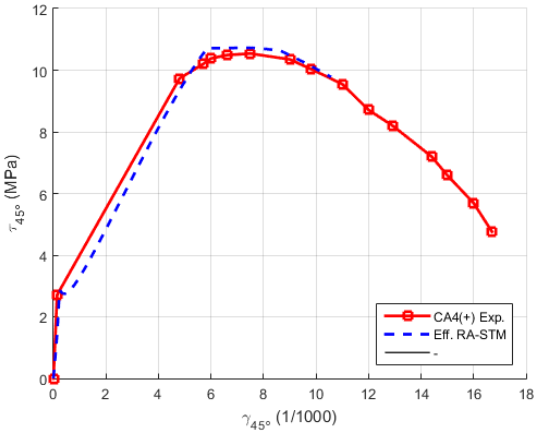

Curve $\tau_{45^\circ} - \gamma_{45^\circ}$

Panel CA4 (Mansour and Hsu, 2005) - Negative loading [1]

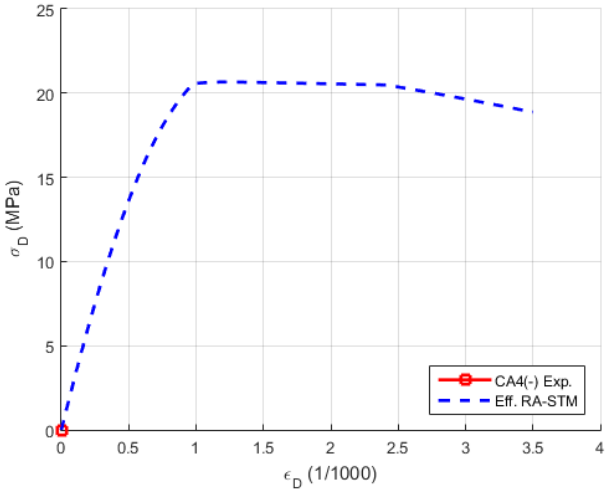

Curva $\sigma_D - \varepsilon_D$

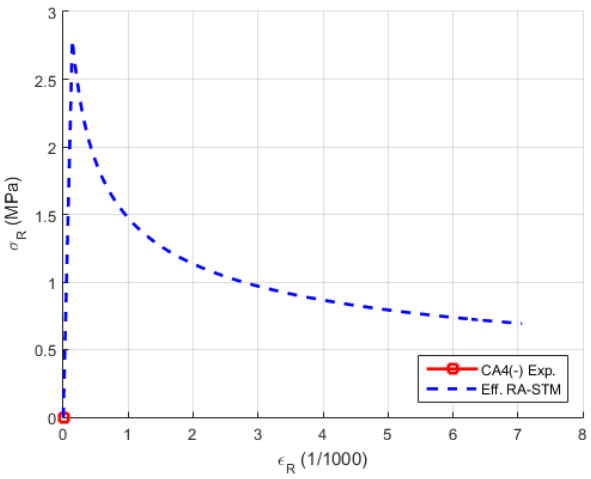

Curva $\sigma_R - \varepsilon_R$

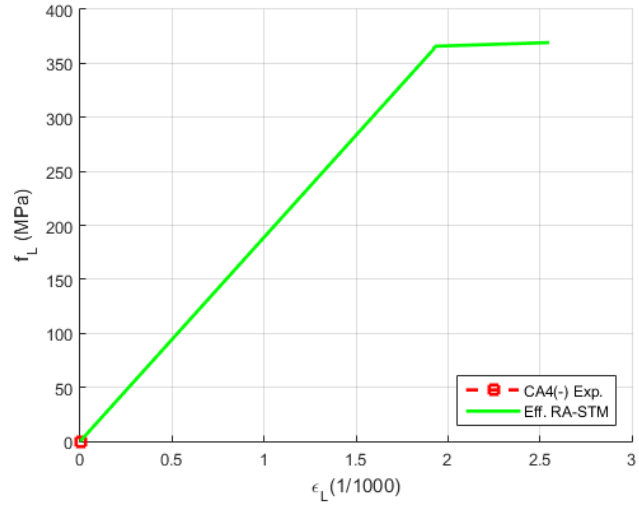

Curva $f_L - \varepsilon_L$

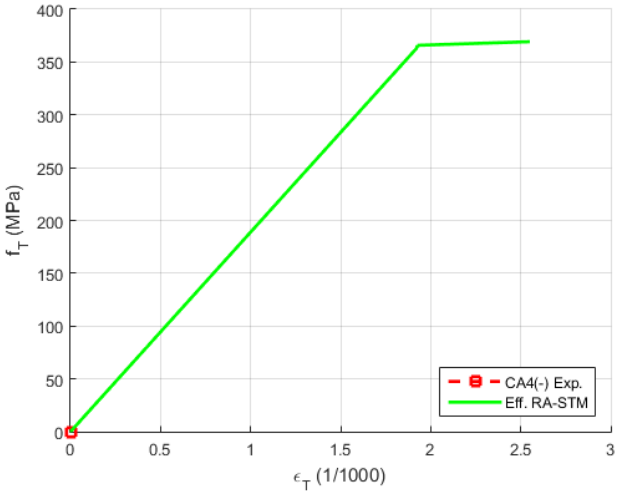

Curva $f_T - \varepsilon_T$

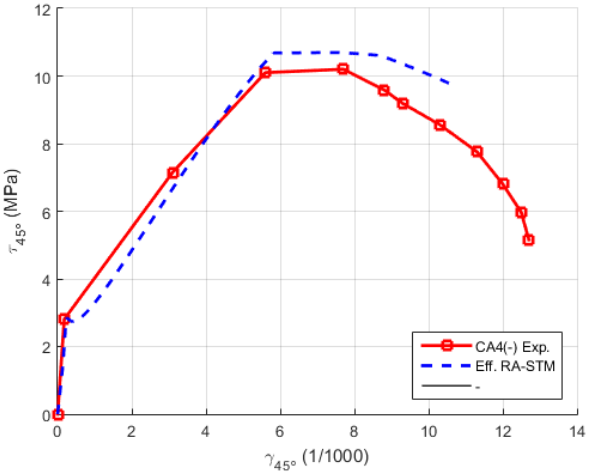

Curve $\tau_{45°} - \gamma_{45°}$

Panel CB3 (Mansour and Hsu, 2005) - Positive loading

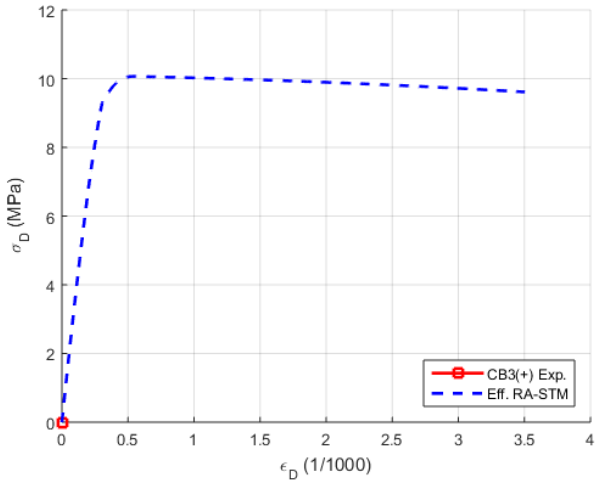

Curva $\sigma_D - \varepsilon_D$

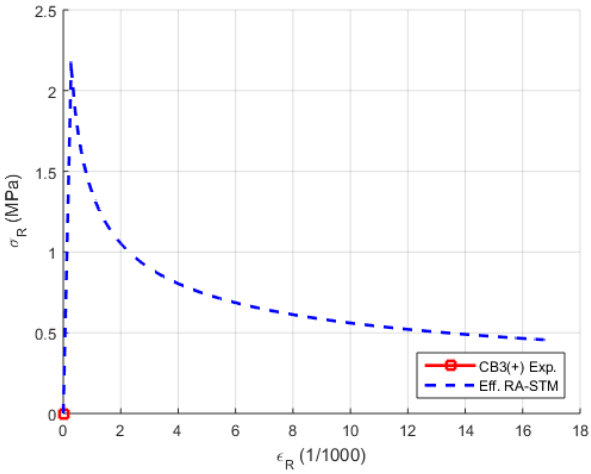

Curva $\sigma_R - \varepsilon_R$

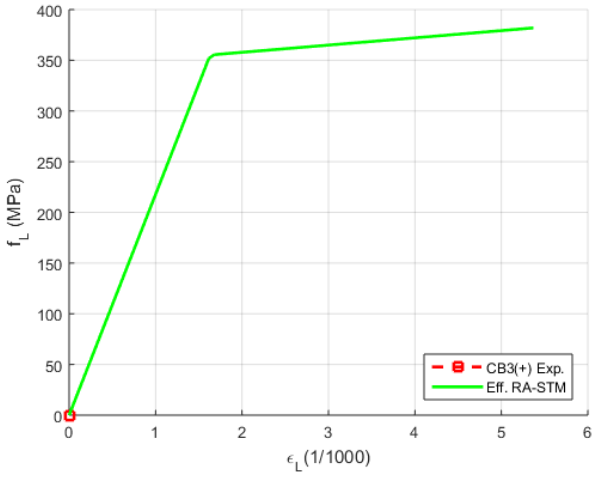

Curva $f_L - \varepsilon_L$

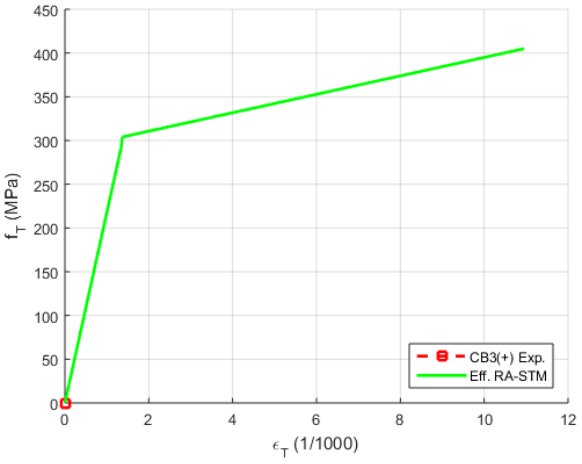

Curva $f_T - \varepsilon_T$

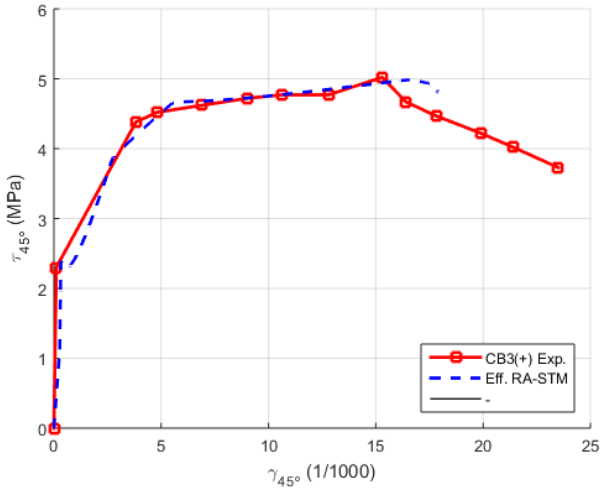

Curve $\tau_{45°} - \gamma_{45°}$

Panel CB3 (Mansour and Hsu, 2005) - Negative loading (1)

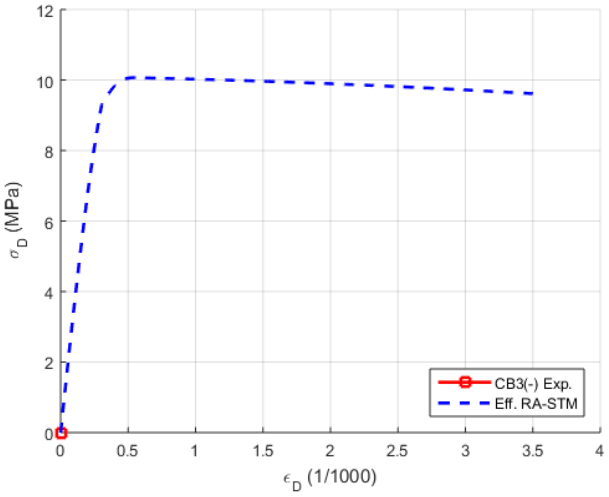

Curva $\sigma_D - \varepsilon_D$

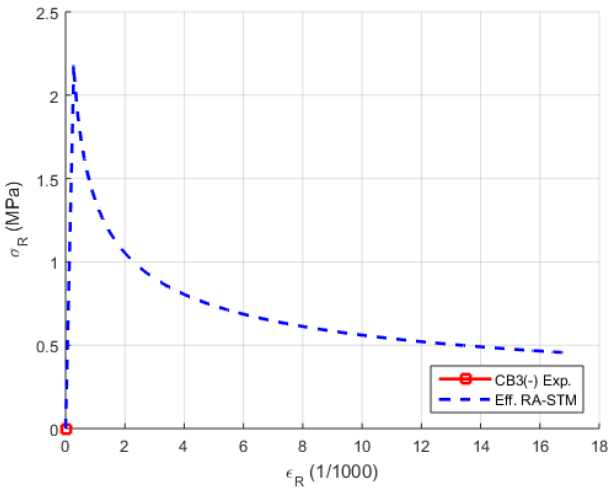

Curva $\sigma_R - \varepsilon_R$

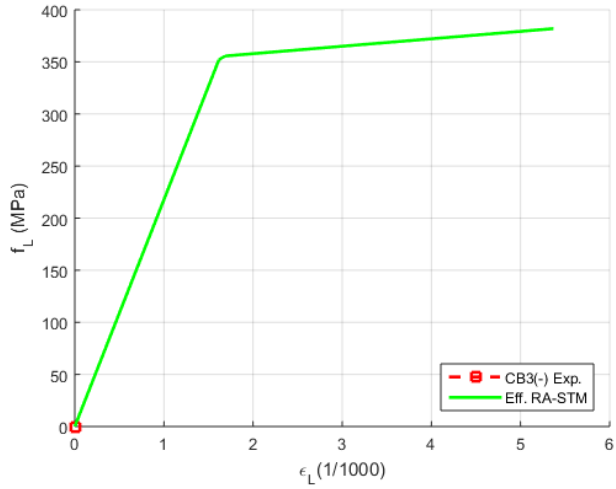

Curva $f_L - \varepsilon_L$

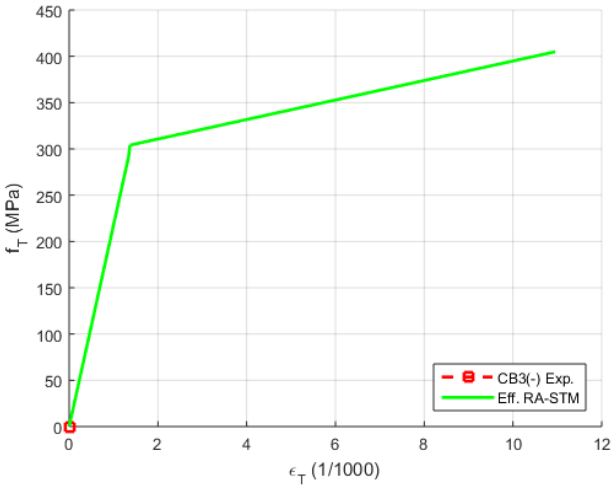

Curva $f_T - \varepsilon_T$

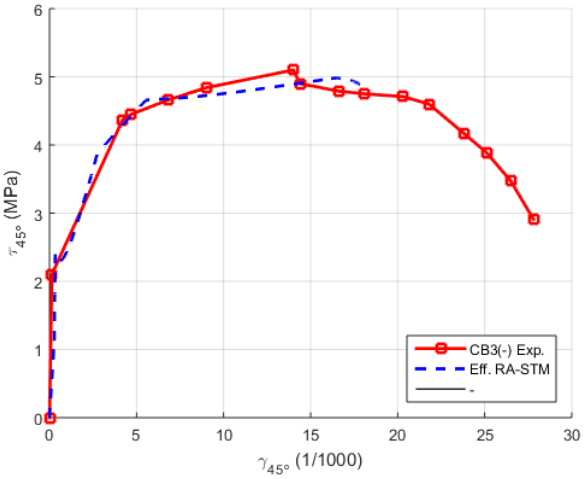

Curve $\tau_{45°} - \gamma_{45°}$

Panel CB4 (Mansour and Hsu, 2005) - Positive loading

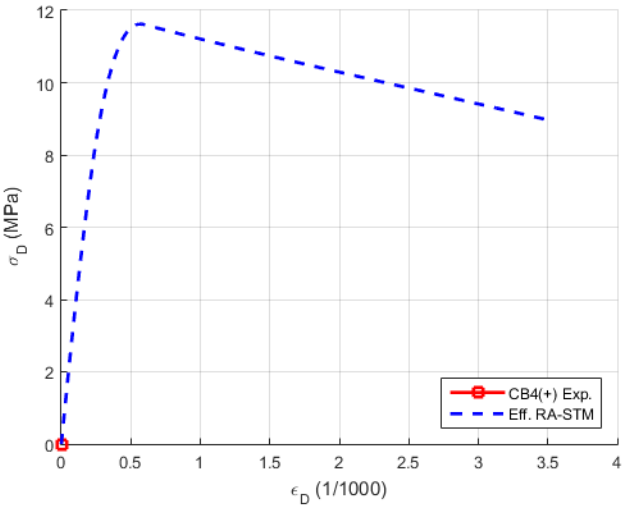

Curva $\sigma_D - \varepsilon_D$

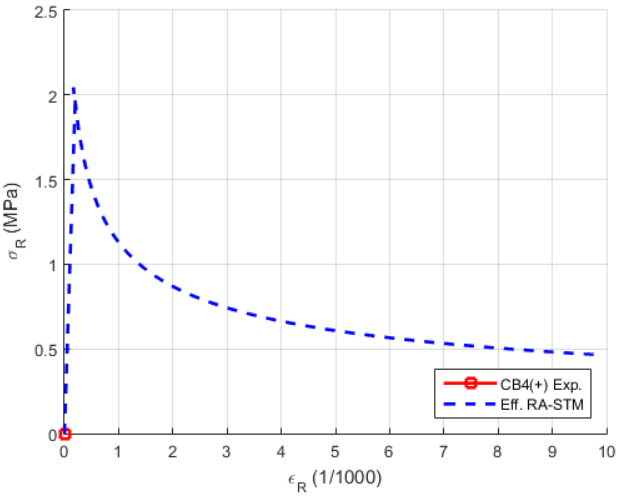

Curva $\sigma_R - \varepsilon_R$

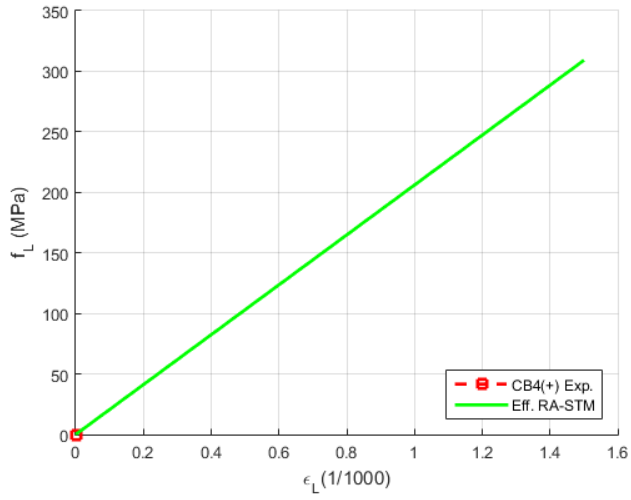

Curva $f_L - \varepsilon_L$

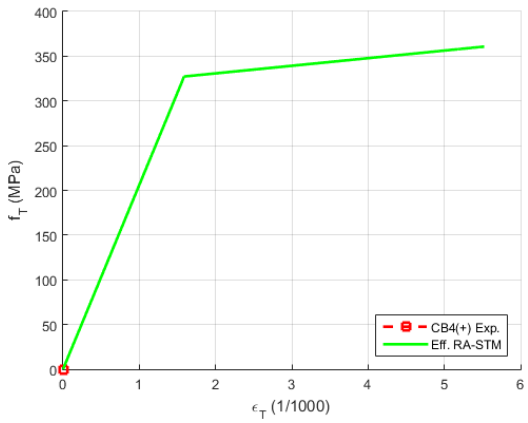

Curva $f_T - \varepsilon_T$

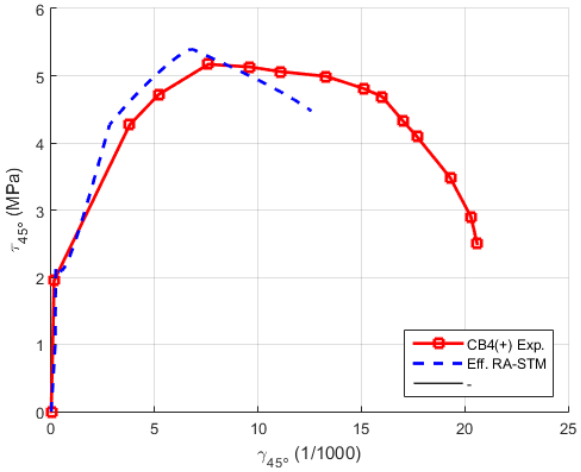

Curve $\tau_{45^\circ} - \gamma_{45^\circ}$

Panel CB4 (Mansour and Hsu, 2005) - Negative loading (1)

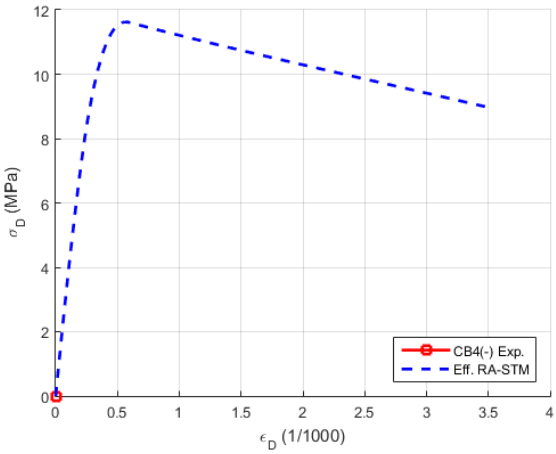

Curva $\sigma_D - \varepsilon_D$

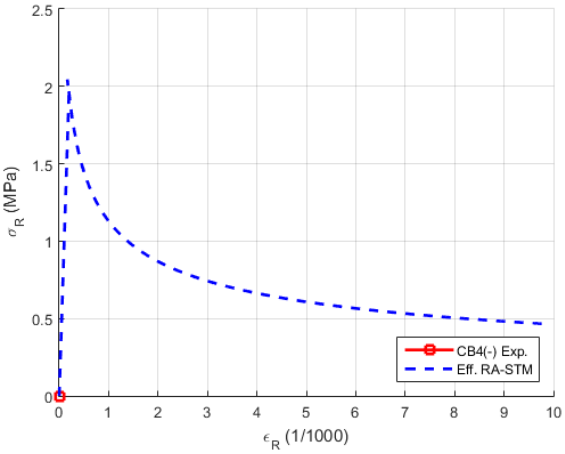

Curva $\sigma_R - \varepsilon_R$

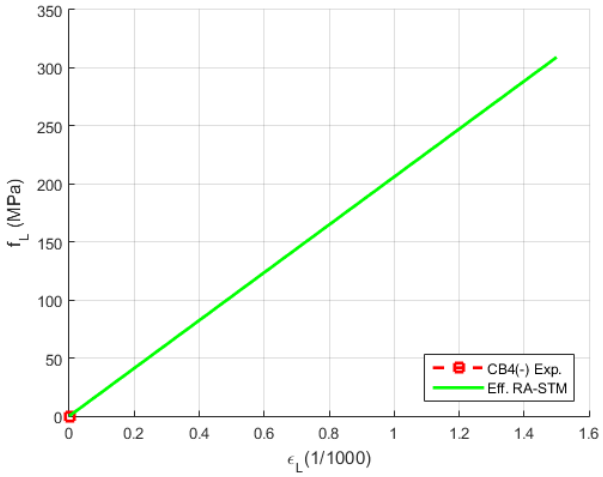

Curva $f_L - \varepsilon_L$

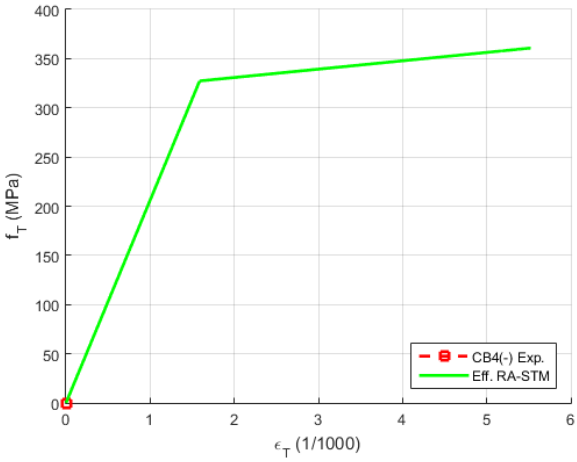

Curva $f_T - \varepsilon_T$

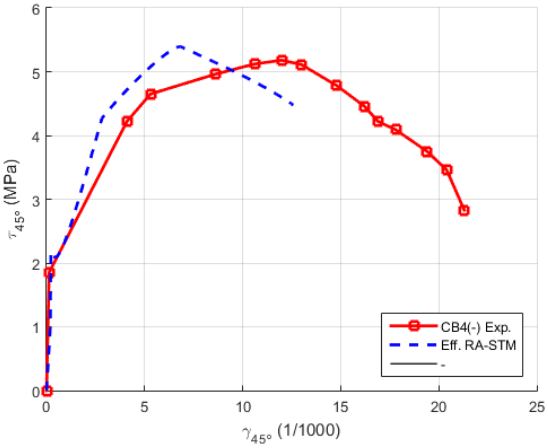

Curve $\tau_{45°} - \gamma_{45°}$

Panel CD2 (Mansour and Hsu, 2005) - Positive loading

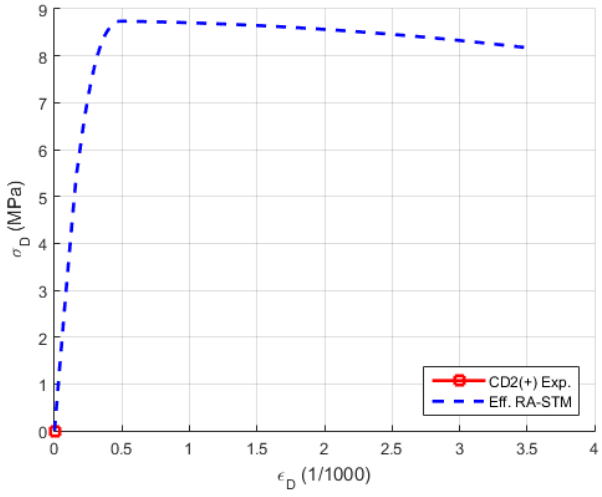

Curva $\sigma_D - \varepsilon_D$

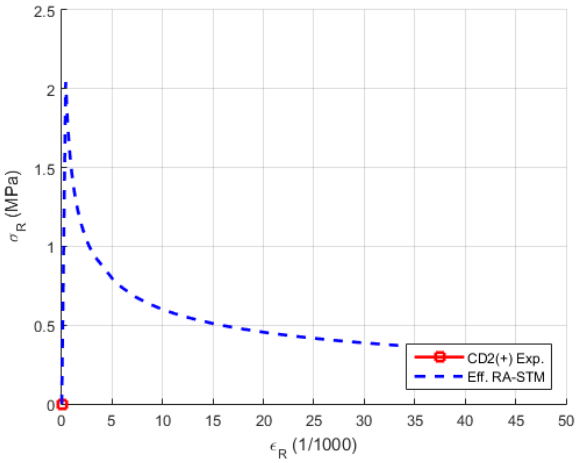

Curva $\sigma_R - \varepsilon_R$

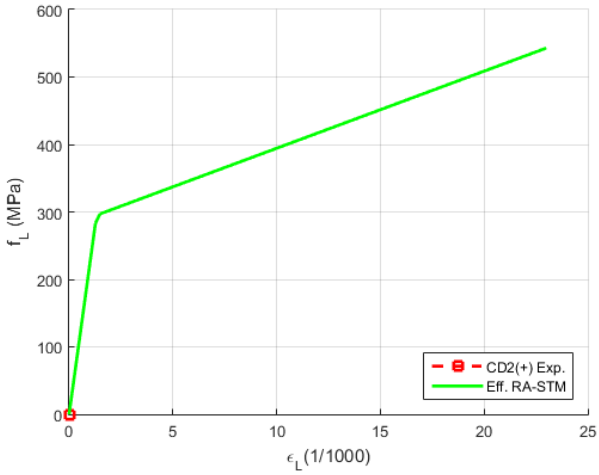

Curva $f_L - \varepsilon_L$

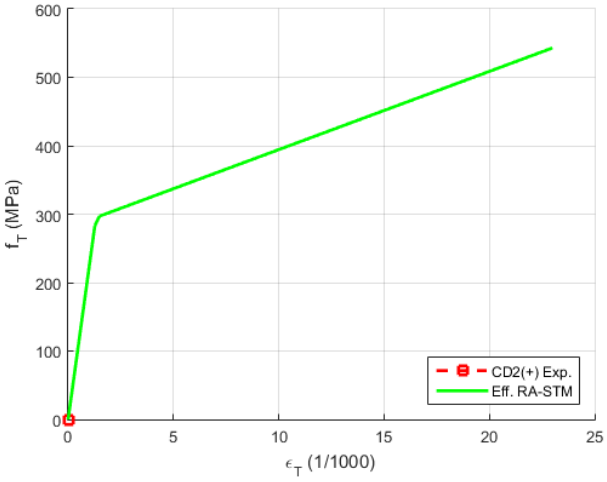

Curva $f_T - \varepsilon_T$

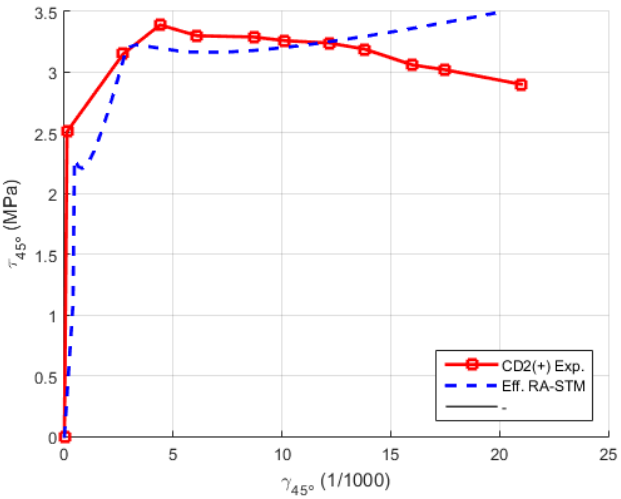

Curve $\tau_{45°} - \gamma_{45°}$

Panel CD2 (Mansour and Hsu, 2005) - Negative loading (1)

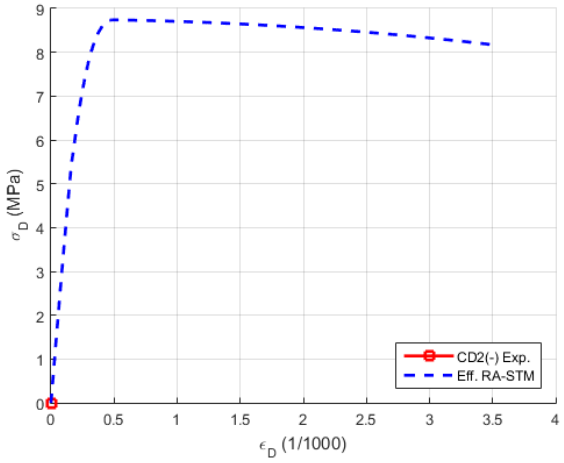

Curva $\sigma_D - \varepsilon_D$

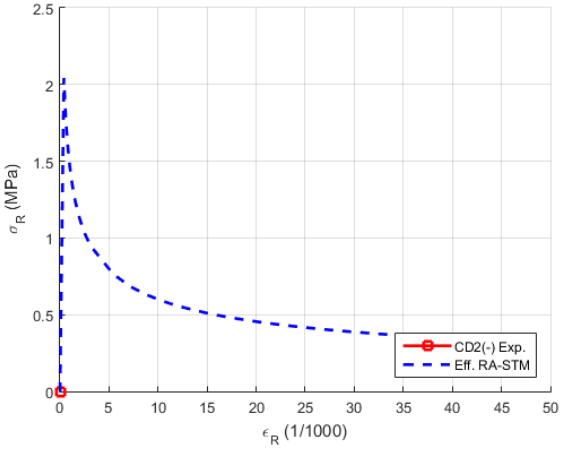

Curva $\sigma_R - \varepsilon_R$

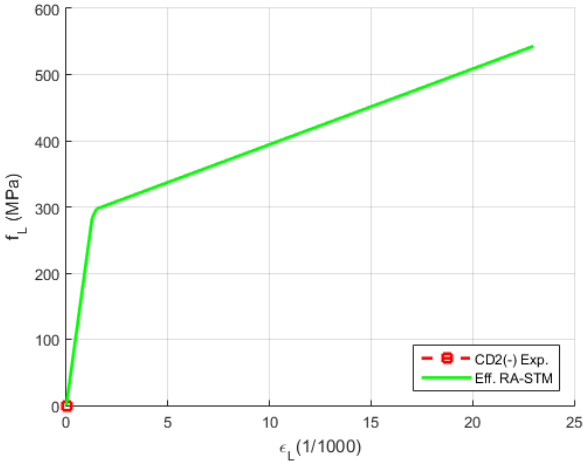

Curva $f_L - \varepsilon_L$

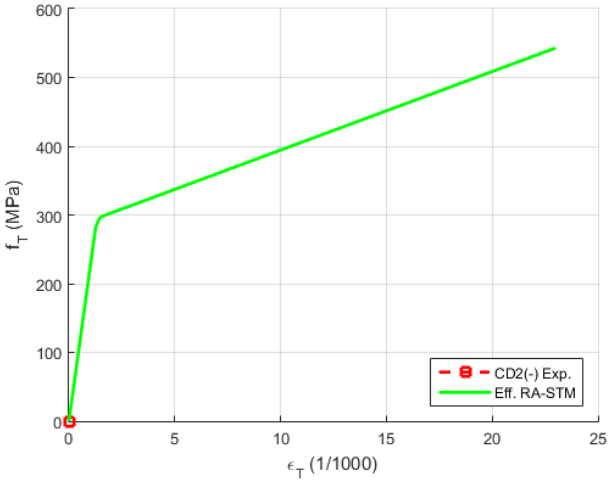

Curva $f_T - \varepsilon_T$

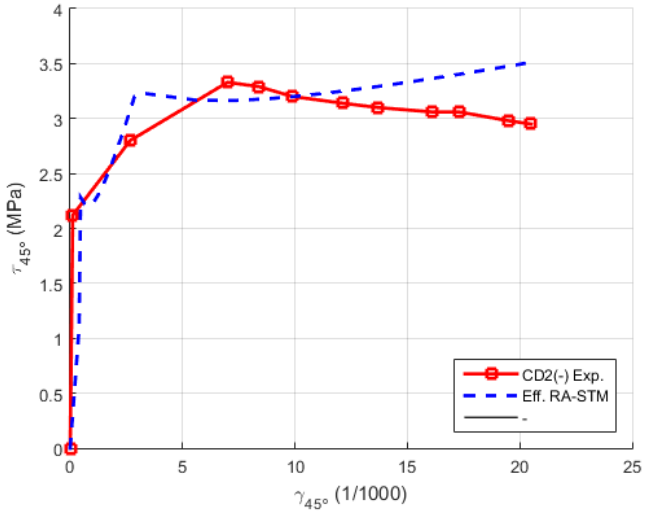

Curve $\tau_{45°} - \gamma_{45°}$

Panel CD3 (Mansour and Hsu, 2005) - Positive loading

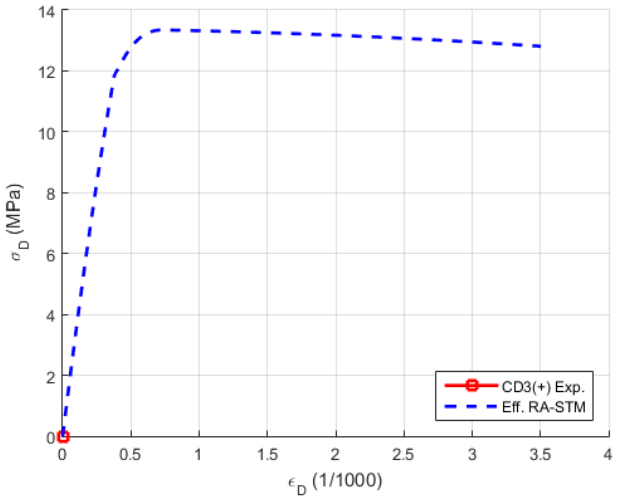

Curva $\sigma_D - \varepsilon_D$

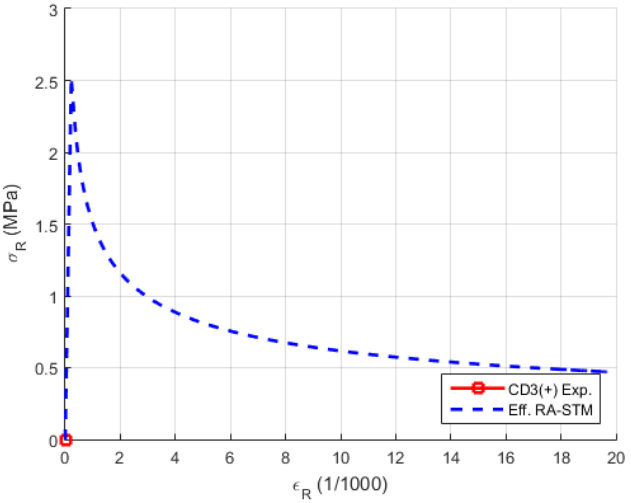

Curva $\sigma_R - \varepsilon_R$

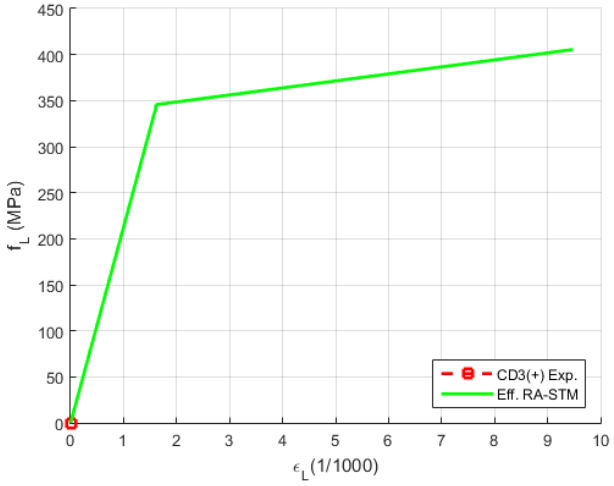

Curva $f_L - \varepsilon_L$

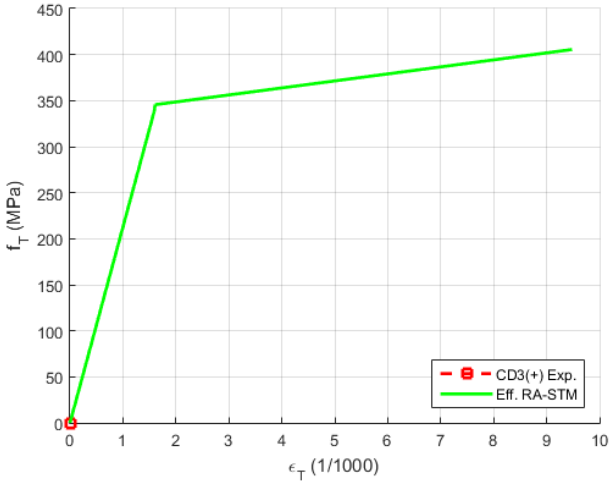

Curva $f_T - \varepsilon_T$

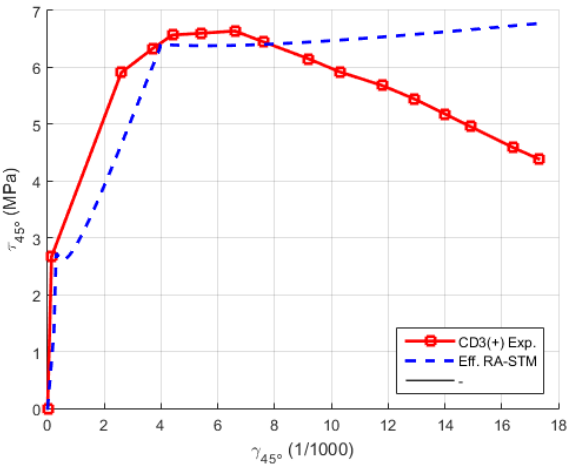

Curve $\tau_{45°} - \gamma_{45°}$

Panel CD3 (Mansour and Hsu, 2005) - Negative loading (1)

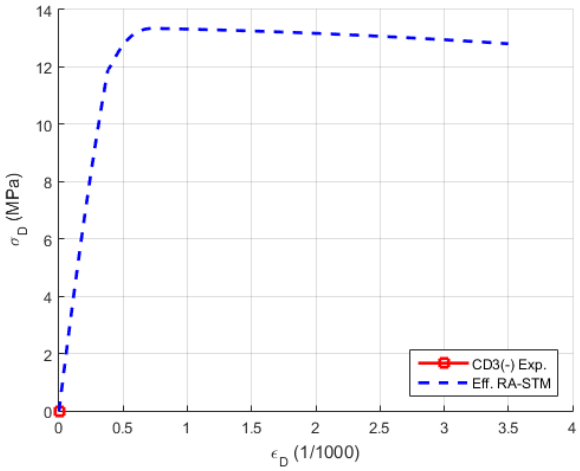

Curva $\sigma_D - \varepsilon_D$

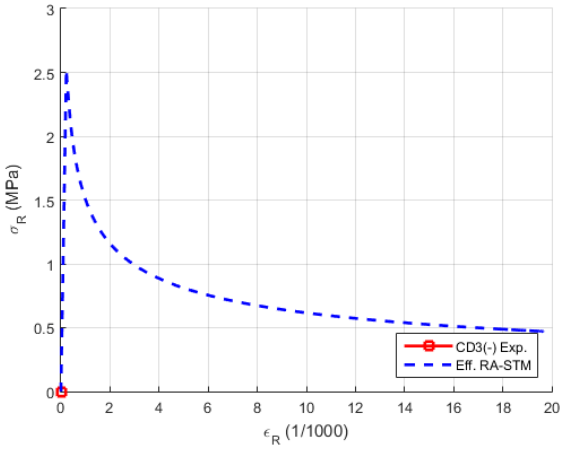

Curva $\sigma_R - \varepsilon_R$

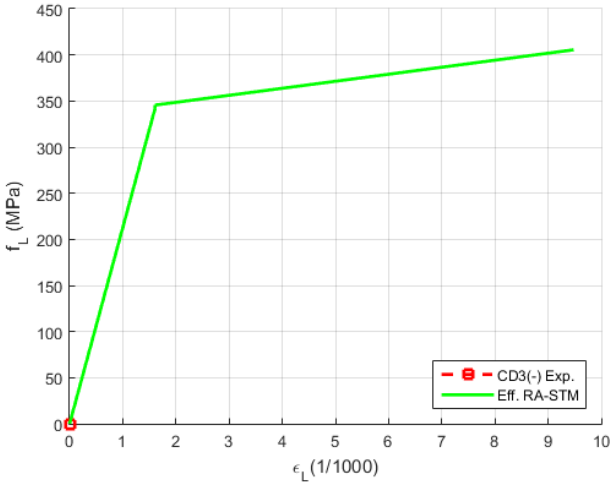

Curva $f_L - \varepsilon_L$

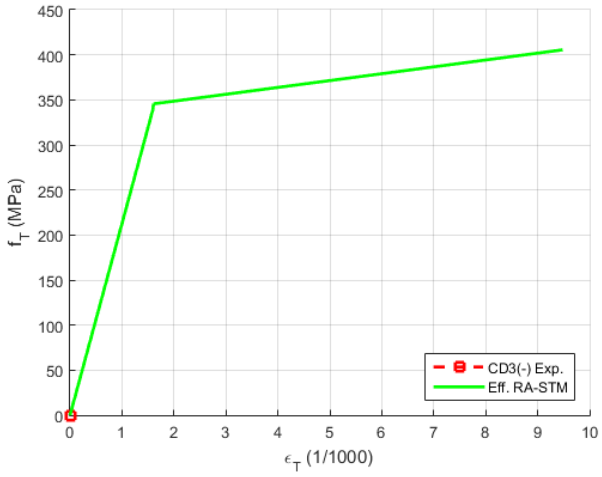

Curva $f_T - \varepsilon_T$

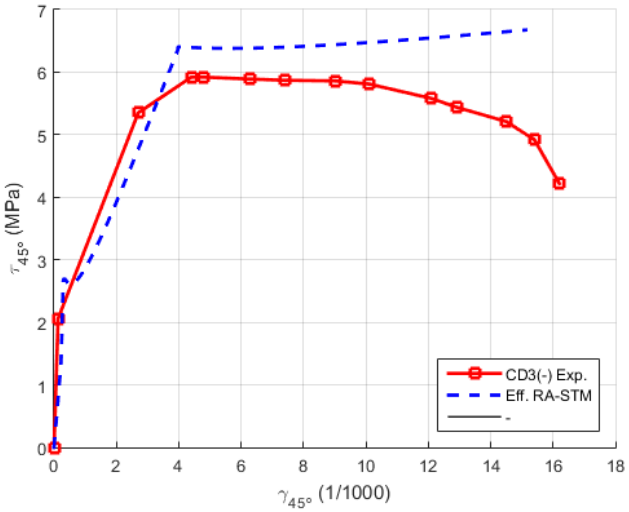

Curve $\tau_{45^\circ} - \gamma_{45^\circ}$

Panel CD4 (Mansour and Hsu, 2005) - Positive loading

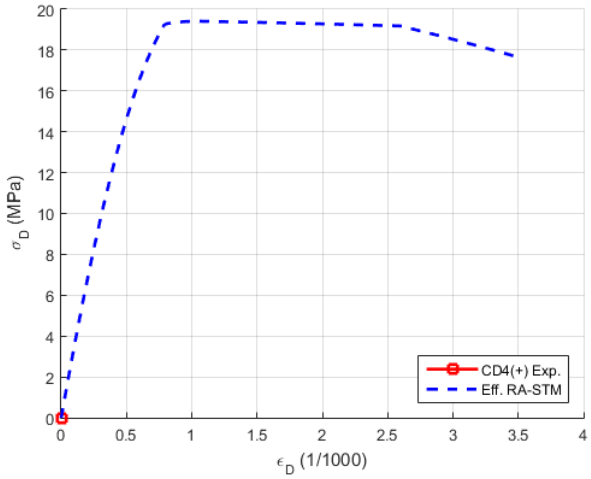

Curva $\sigma_D - \varepsilon_D$

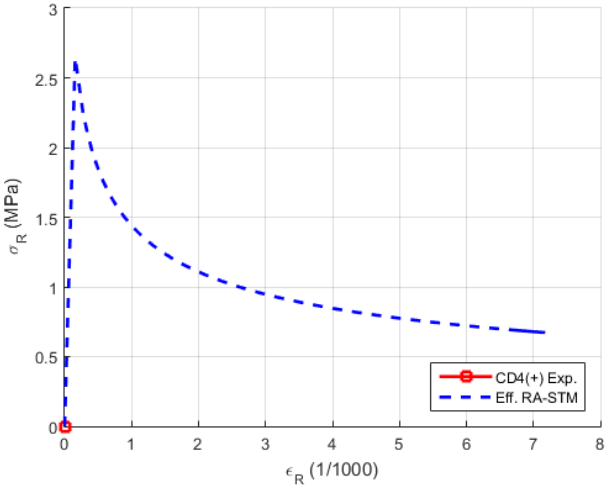

Curva $\sigma_R - \varepsilon_R$

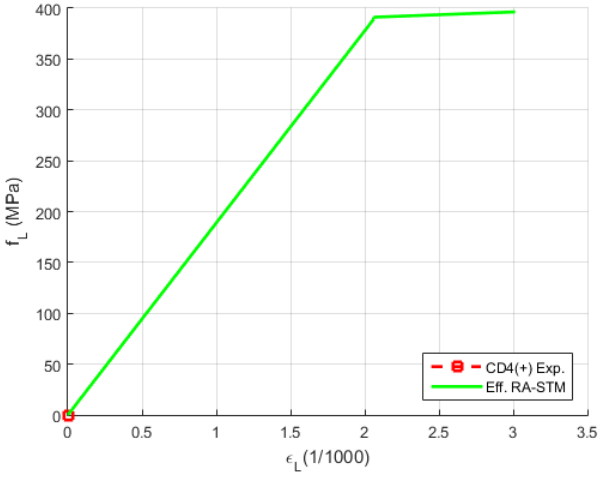

Curva $f_L - \varepsilon_L$

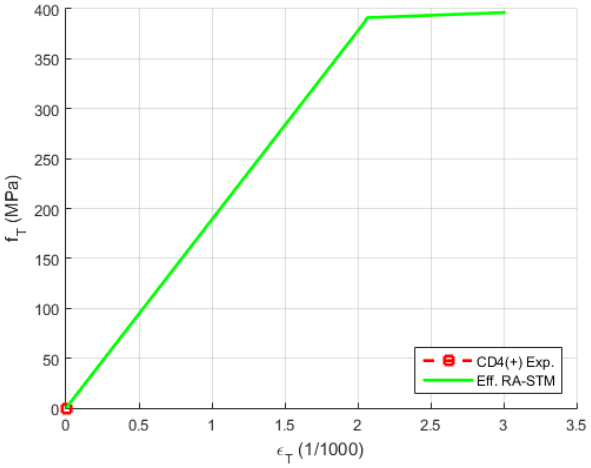

Curva $f_T - \varepsilon_T$

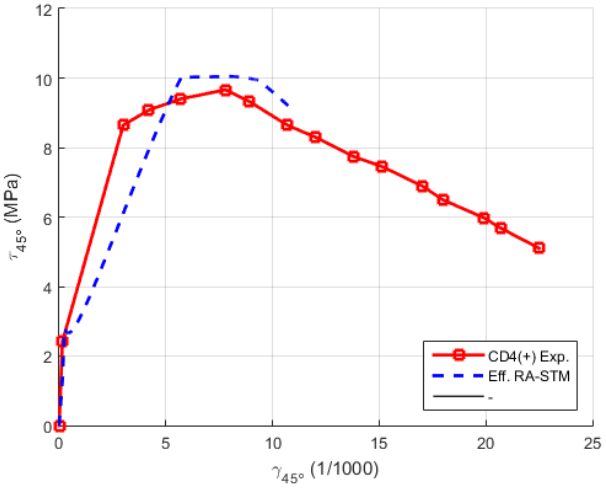

Curve $\tau_{45^\circ} - \gamma_{45^\circ}$

Panel CD4 (Mansour and Hsu, 2005) - Negative loading (1)

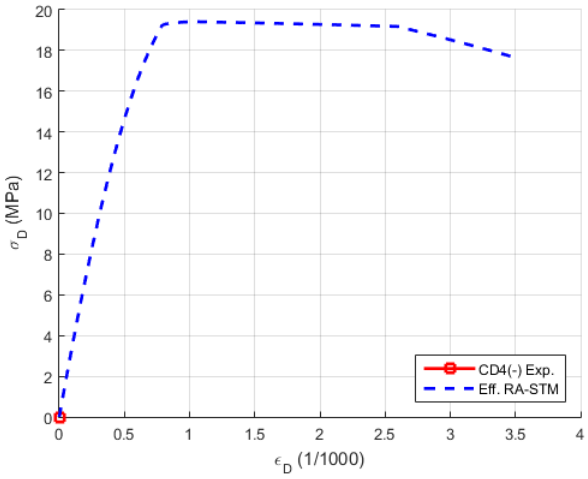

Curva $\sigma_D - \varepsilon_D$

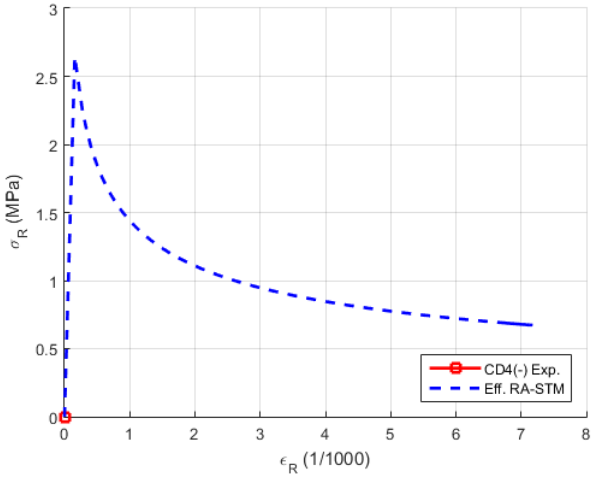

Curva $\sigma_R - \varepsilon_R$

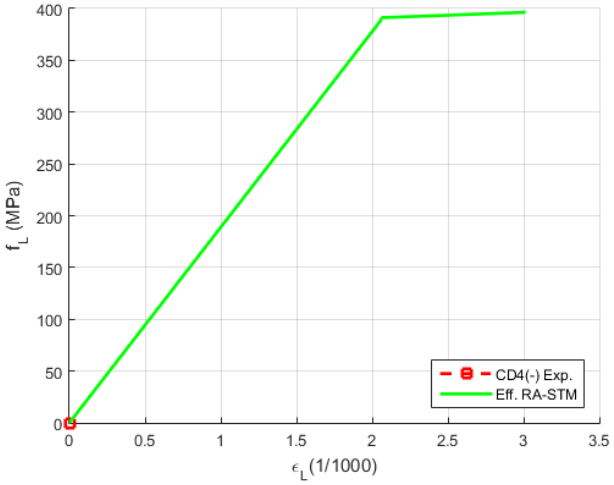

Curva $f_L - \varepsilon_L$

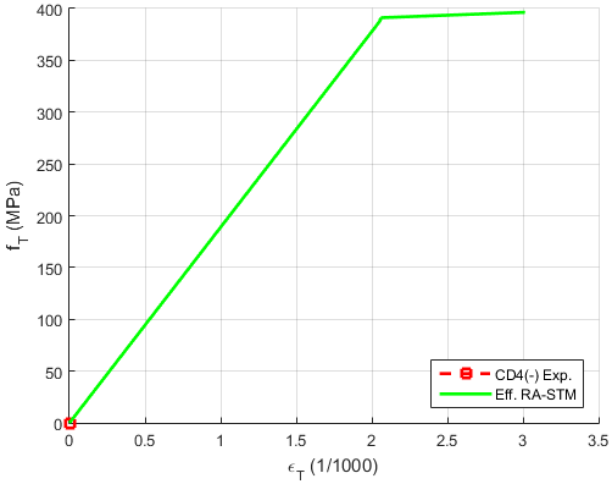

Curva $f_T - \varepsilon_T$

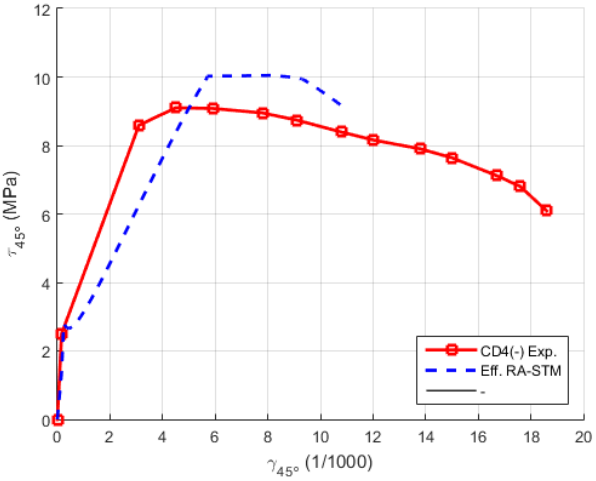

Curve $\tau_{45°} - \gamma_{45°}$

Panel CE2 (Mansour and Hsu, 2005) - Positive loading

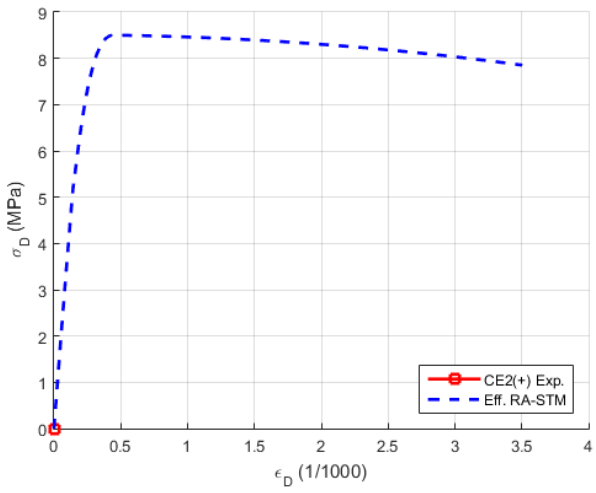

Curva $\sigma_D - \varepsilon_D$

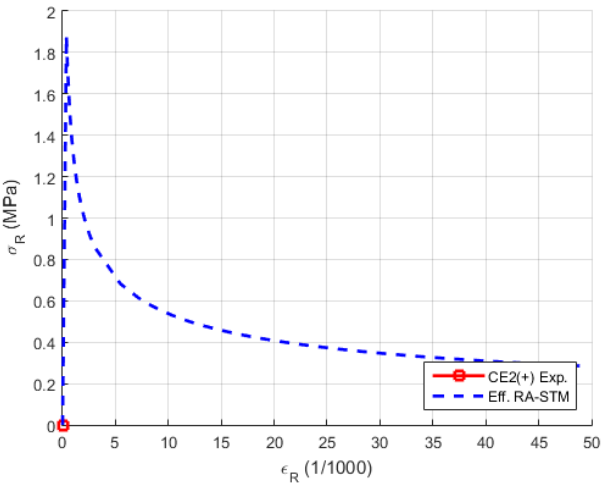

Curva $\sigma_R - \varepsilon_R$

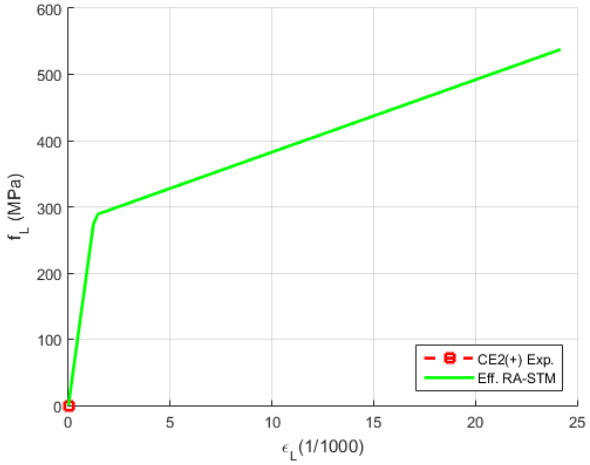

Curva $f_L - \varepsilon_L$

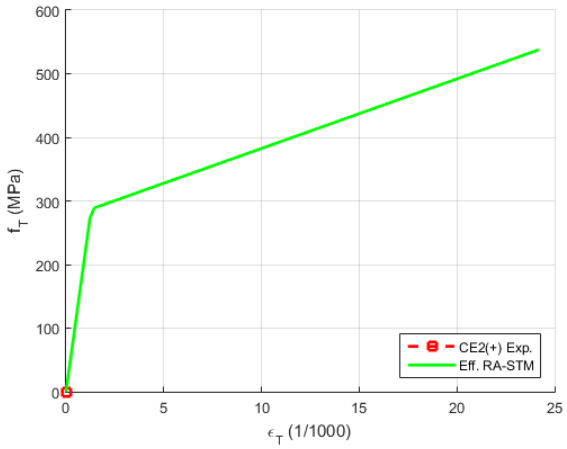

Curva $f_T - \varepsilon_T$

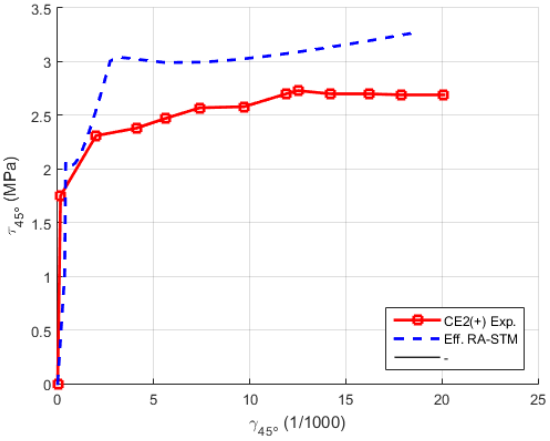

Curve $\tau_{45°} - \gamma_{45°}$

Panel CE2 (Mansour and Hsu, 2005) - Negative loading (1)

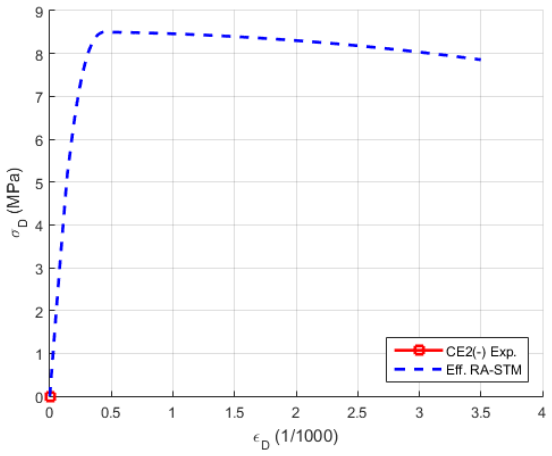

Curva $\sigma_D - \varepsilon_D$

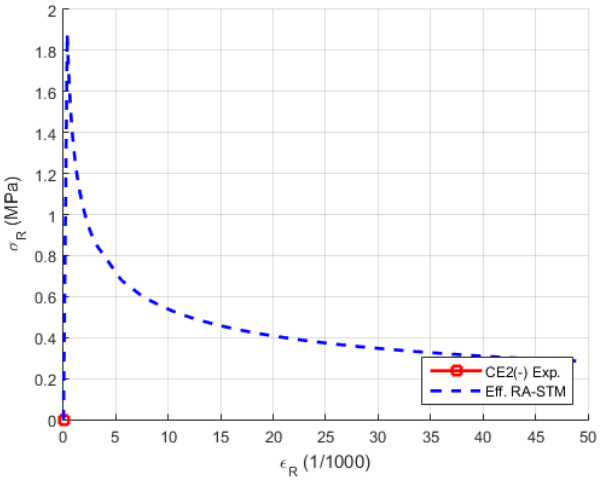

Curva $\sigma_R - \varepsilon_R$

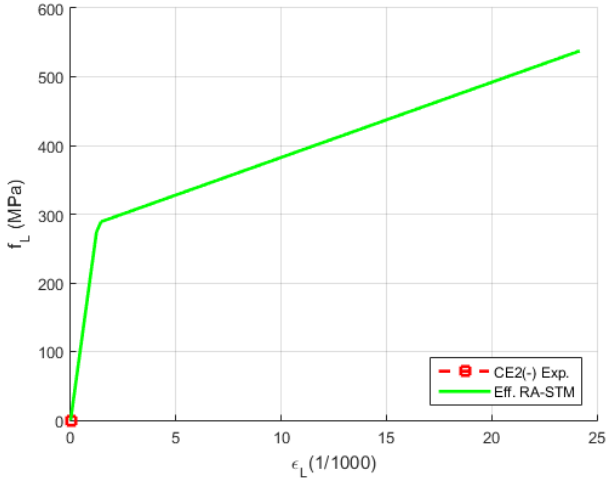

Curva $f_L - \varepsilon_L$

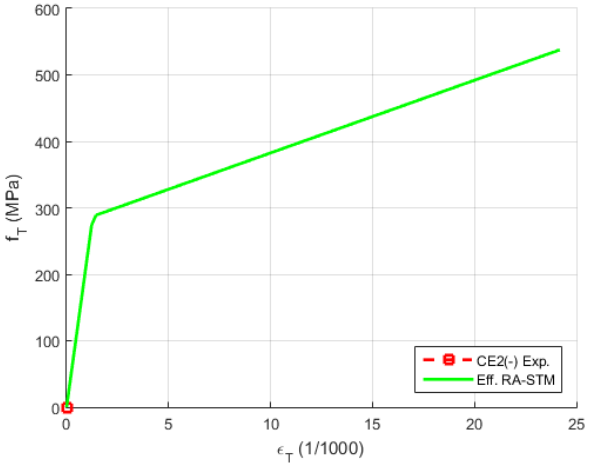

Curva $f_T - \varepsilon_T$

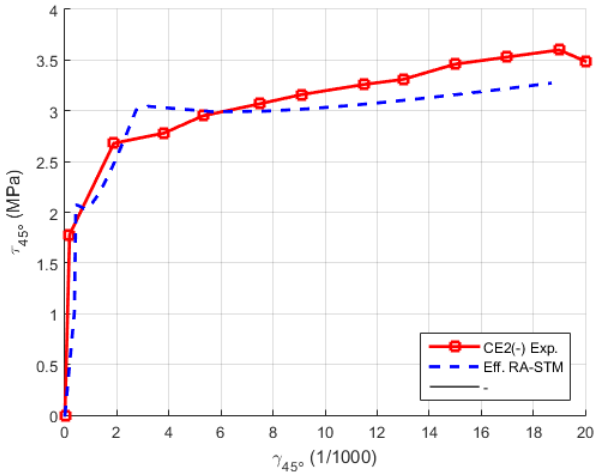

Curve $\tau_{45°} - \gamma_{45°}$

Panel CE3 (Mansour and Hsu, 2005) - Positive loading

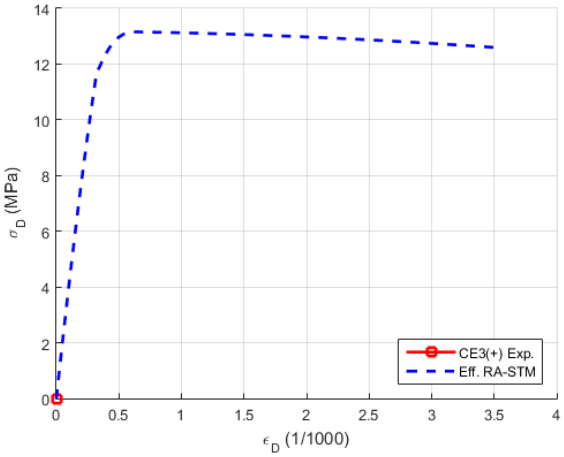

Curva $\sigma_D - \varepsilon_D$

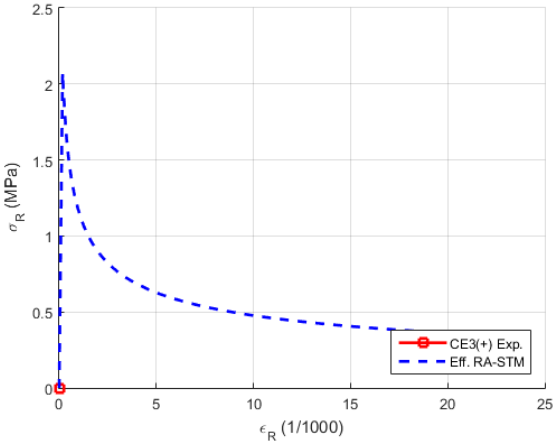

Curva $\sigma_R - \varepsilon_R$

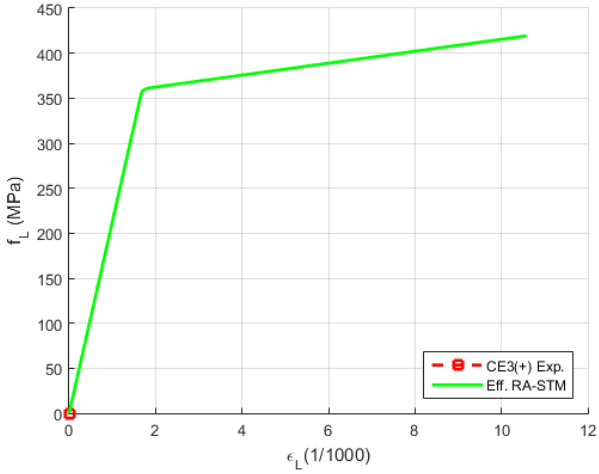

Curva $f_L - \varepsilon_L$

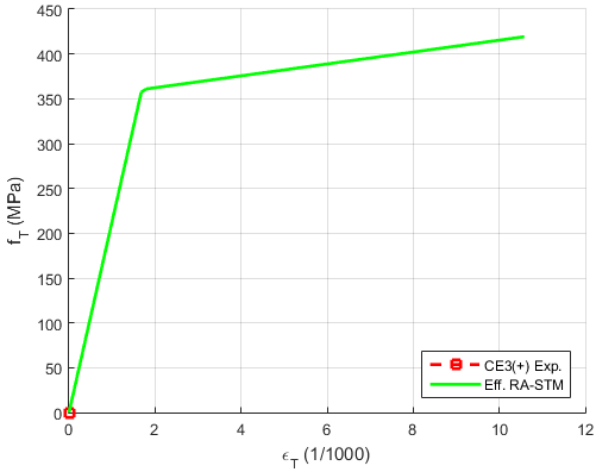

Curva $f_T - \varepsilon_T$

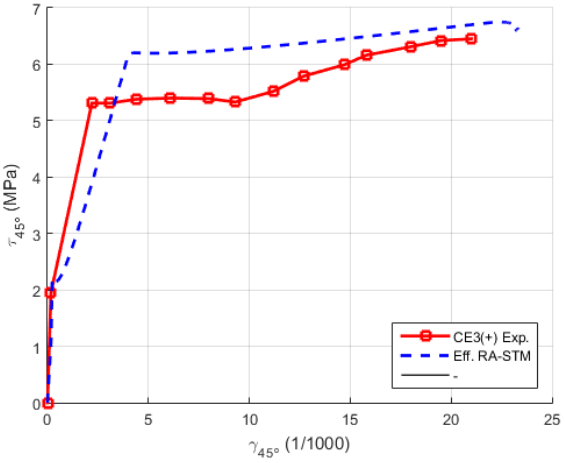

Curve $\tau_{45°} - \gamma_{45°}$

Panel CE3 (Mansour and Hsu, 2005) - Negative loading (1)

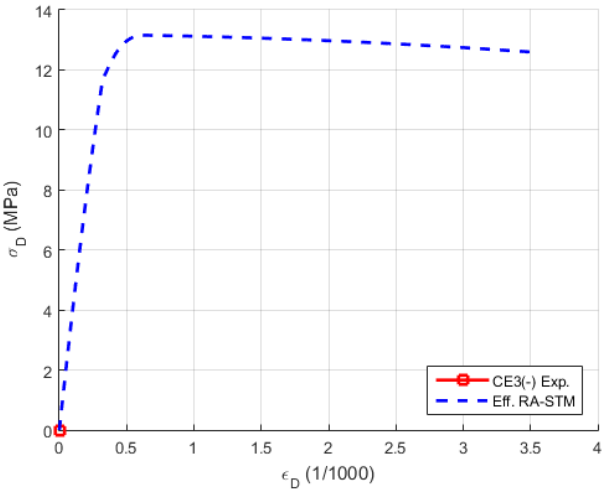

Curva $\sigma_D - \varepsilon_D$

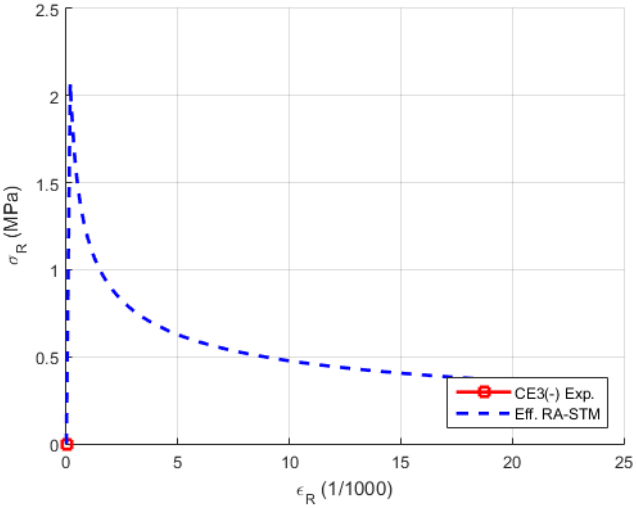

Curva $\sigma_R - \varepsilon_R$

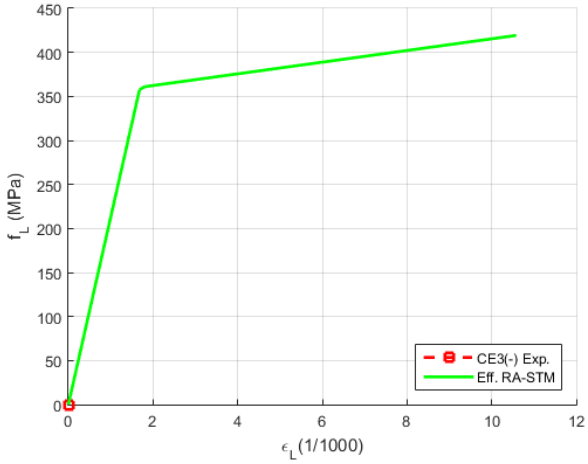

Curva $f_L - \varepsilon_L$

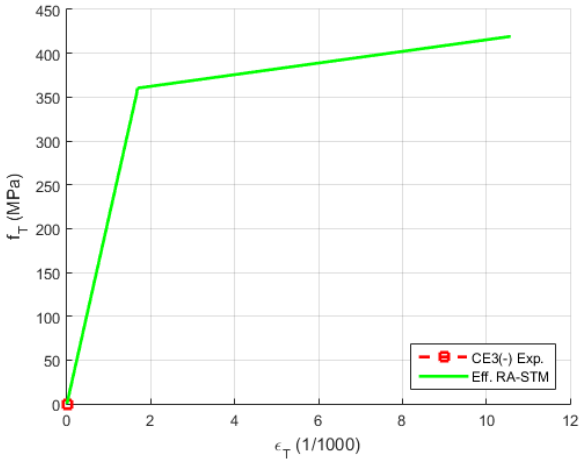

Curva $f_T - \varepsilon_T$

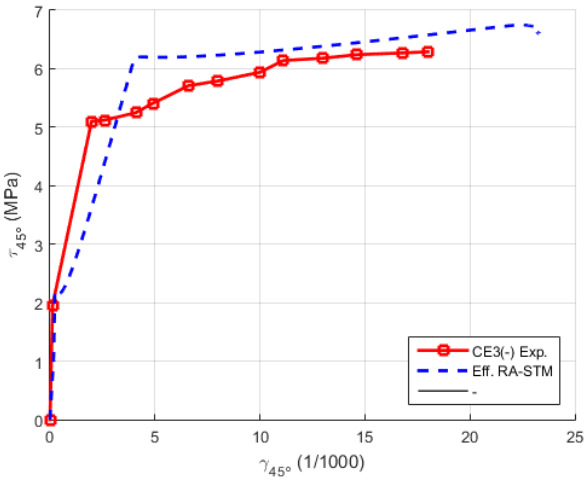

Curve $\tau_{45°} - \gamma_{45°}$

Panel CE4 (Mansour and Hsu, 2005) - Positive loading

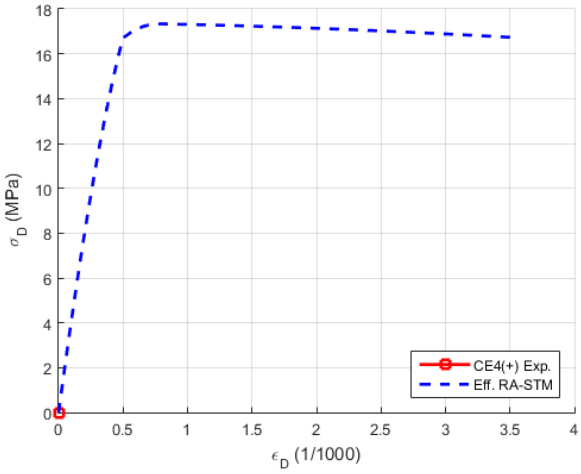

Curva $\sigma_D - \varepsilon_D$

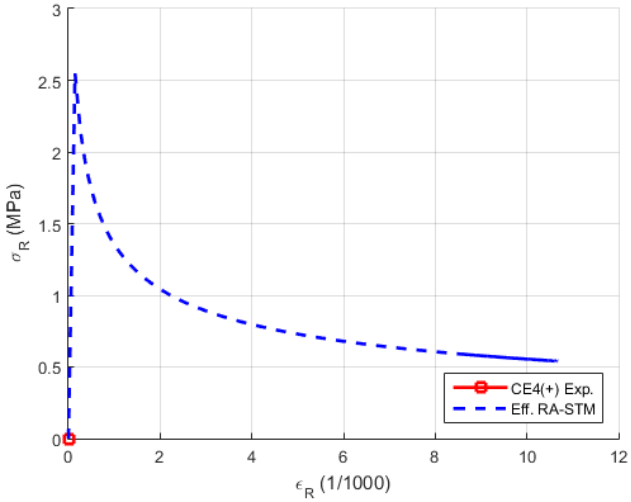

Curva $\sigma_R - \varepsilon_R$

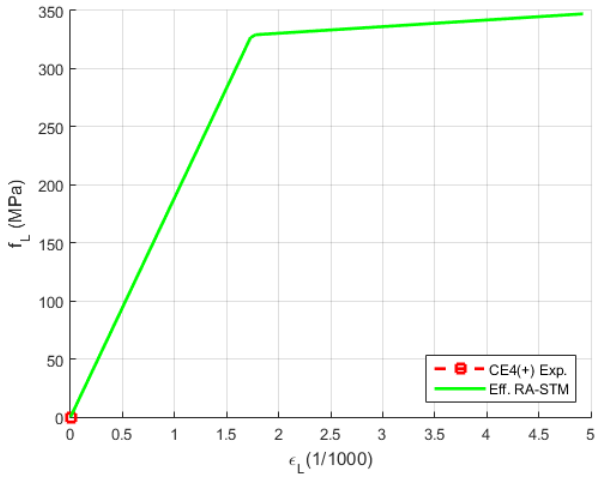

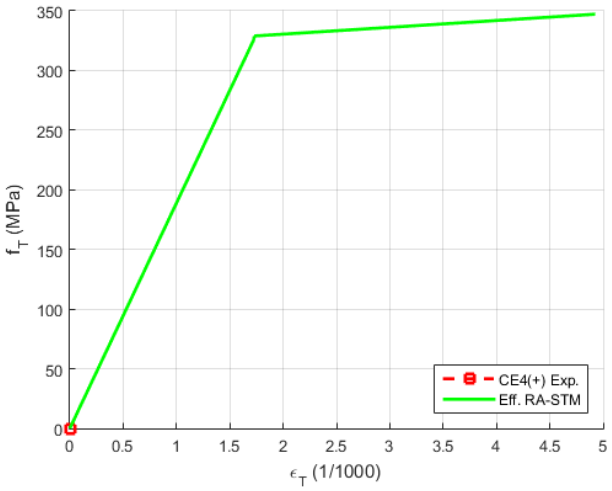

Curva $f_L - \varepsilon_L$

Curva $f_T - \varepsilon_T$

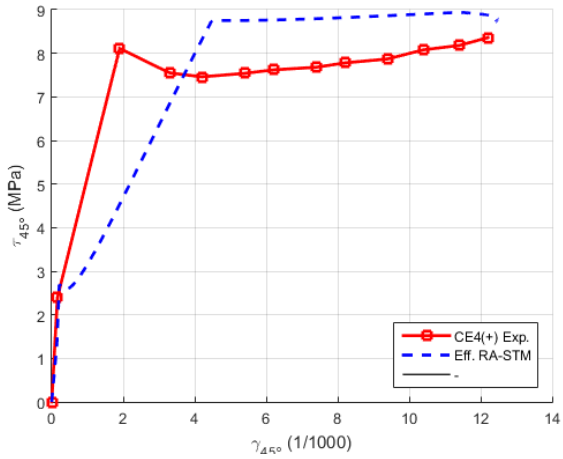

Curve $\tau_{45°} - \gamma_{45°}$

Panel CE4 (Mansour and Hsu, 2005) - Negative loading (1)

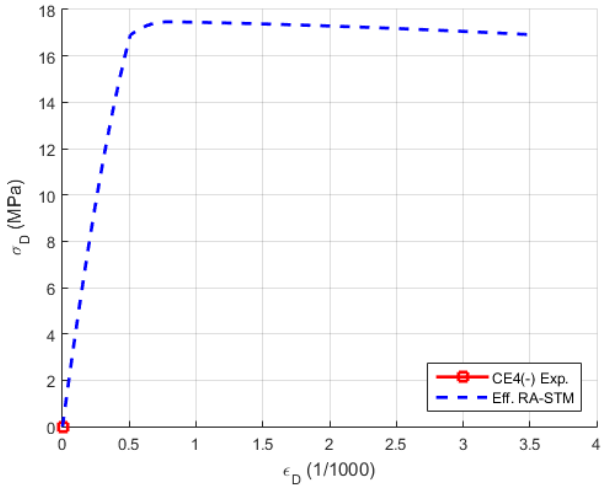

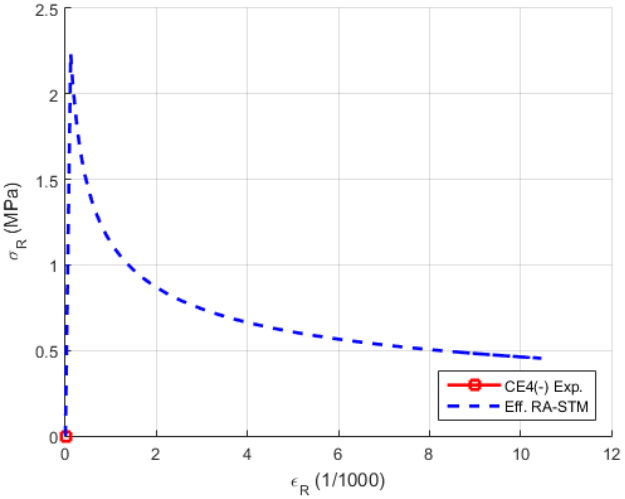

Curva $\sigma_D - \varepsilon_D$

Curva $\sigma_R - \varepsilon_R$

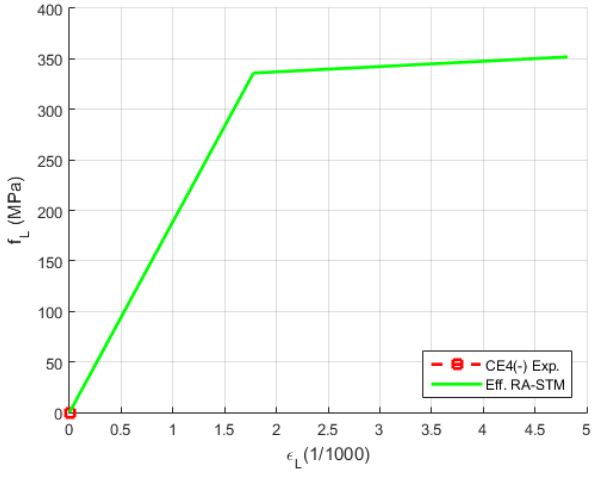

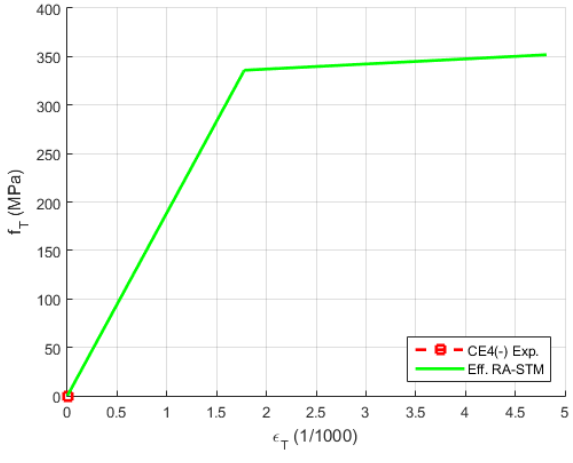

Curva $f_L - \varepsilon_L$

Curva $f_T - \varepsilon_T$

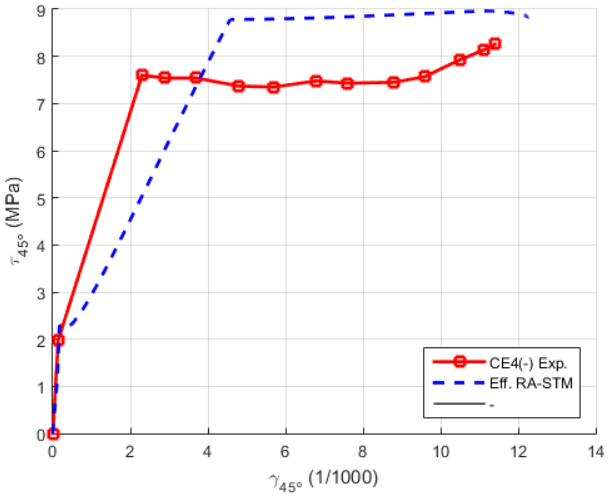

Curve $\tau_{45°} - \gamma_{45°}$

Panel CF2 (Mansour and Hsu, 2005) - Positive loading

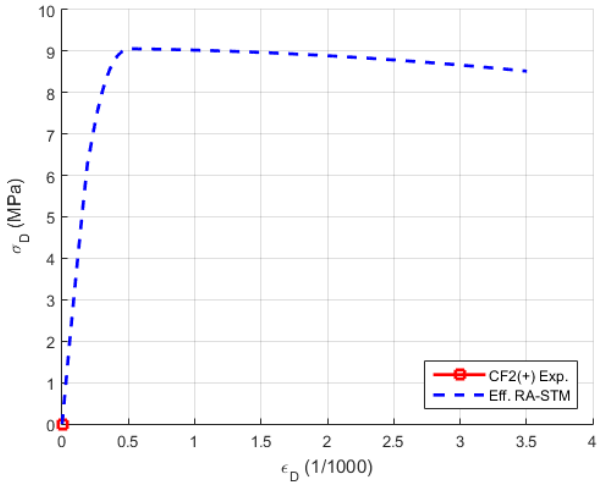

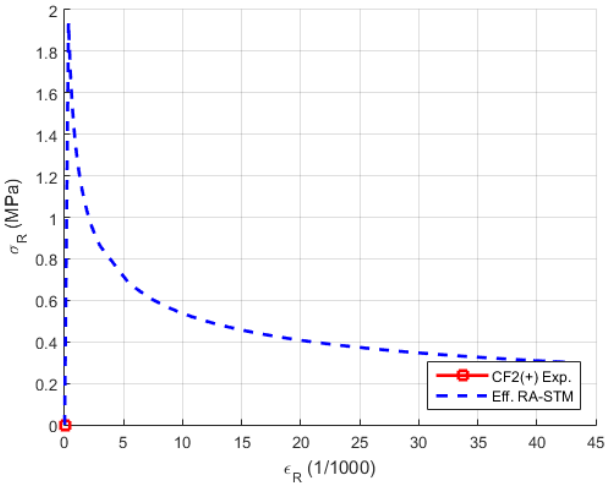

Curva $\sigma_D - \varepsilon_D$

Curva $\sigma_R - \varepsilon_R$

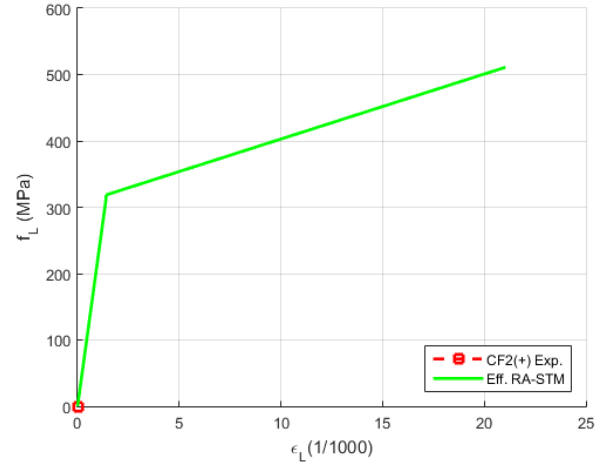

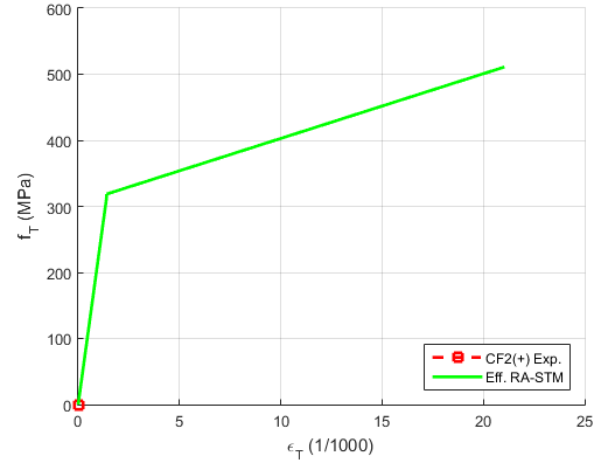

Curva $f_L - \varepsilon_L$

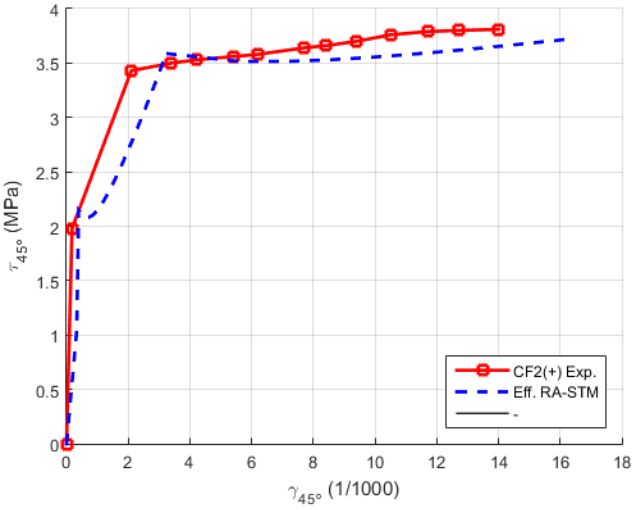

Curve $\tau_{45°} - \gamma_{45°}$

Curva $f_T - \varepsilon_T$

Panel CF2 (Mansour and Hsu, 2005) - Negative loading (1)

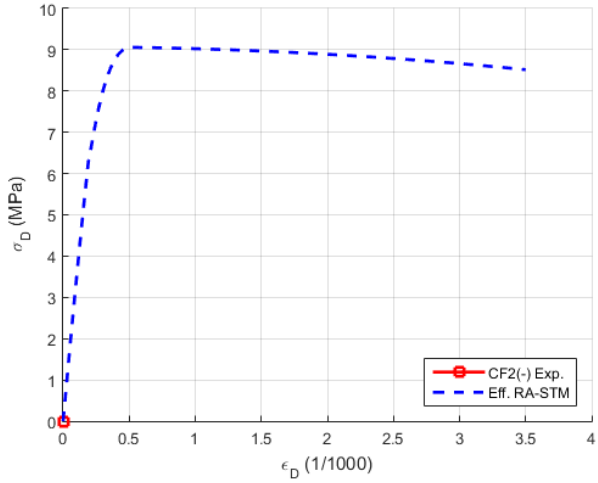

Curva $\sigma_D - \varepsilon_D$

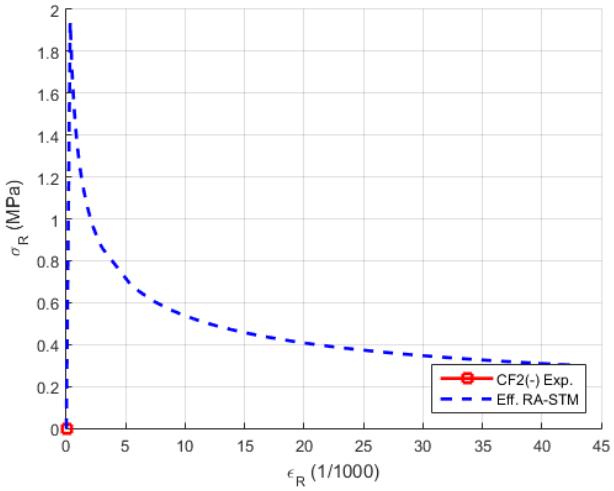

Curva $\sigma_R - \varepsilon_R$

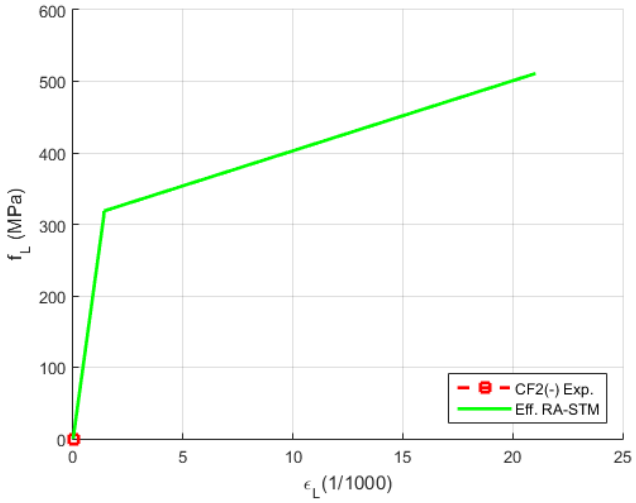

Curva $f_L - \varepsilon_L$

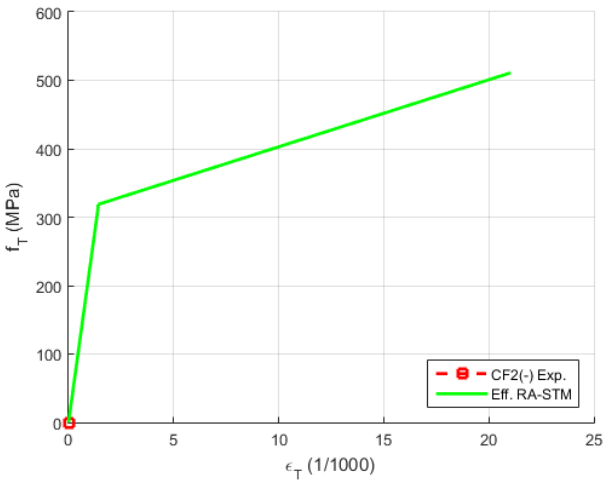

Curva $f_T - \varepsilon_T$

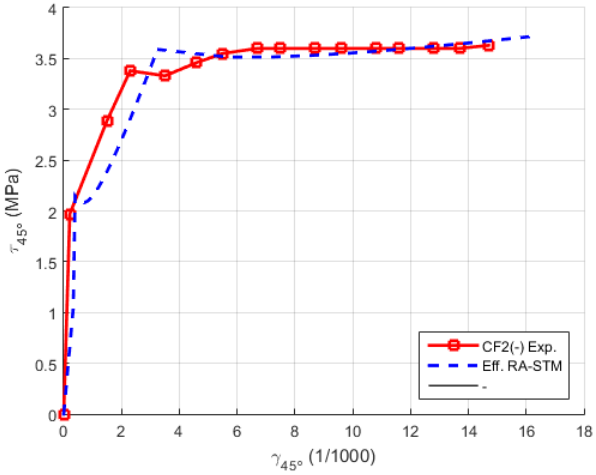

Curve $\tau_{45°} - \gamma_{45°}$

Appendix III

Computing equivalent reinforcement ratios

Only ρ_l:

$\rho_t = 0$

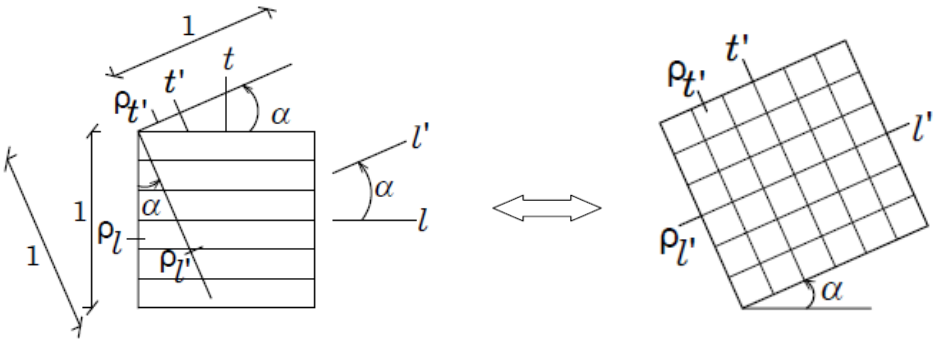

$\rho_l, \rho_t \rightarrow$ analogy with stresses σ_l, σ_t

Results:

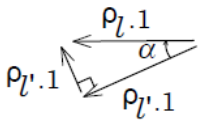

$$\cos\alpha = \frac{\rho'_l}{\rho_l} \leftrightarrow \rho'_l = cos\alpha.\rho_l$$

$$\sin\alpha = \frac{\rho'_t}{\rho_l} \leftrightarrow \rho'_t = sin\alpha.\rho_l$$

Verification:

- $\alpha = 0^\circ$

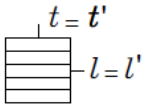

$\rho'_l = \rho_l$

$\rho'_t = 0$

- $\alpha = 90^\circ$

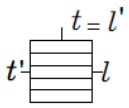

$\rho'_l = 0$

$\rho'_t = \rho_l$

Only ρ_t:

$\rho_l = 0$

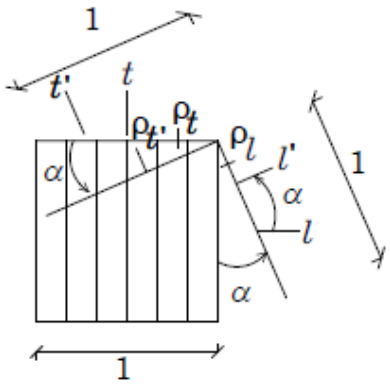

Results:

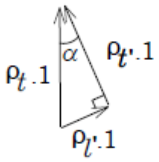

$$\sin\alpha = \frac{\rho'_l}{\rho_t} \leftrightarrow \rho'_l = sin\alpha.\rho_t$$

$$\cos\alpha = \frac{\rho'_t}{\rho_t} \leftrightarrow \rho'_t = cos\alpha.\rho_l$$

Verification:

- $\alpha = 0^\circ$

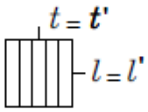

$\rho'_l = 0$

$\rho'_t = \rho_t$

- $\alpha = 90^\circ$

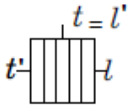

$\rho'_l = \rho_t$

$\rho'_t = 0$

Conclusion $\rho_l + \rho_t$:

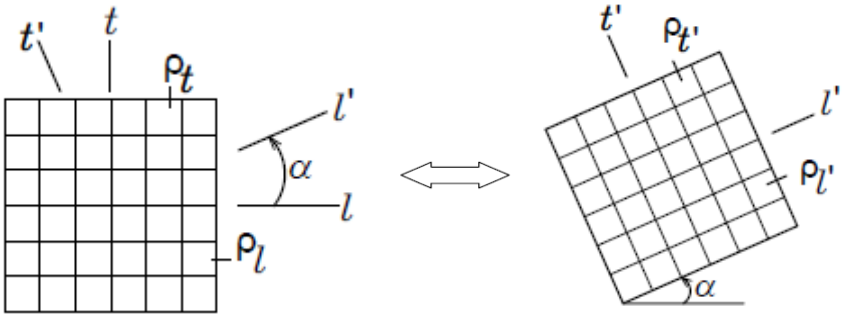

$\rho'_l = cos\alpha . \rho_l + sin\alpha . \rho_t$

$\rho'_t = sin\alpha . \rho_l + cos\alpha . \rho_t$

Verification:

- $\alpha = 0^\circ$

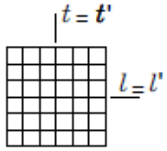

$\rho'_l = \rho_l$

$\rho'_t = \rho_t$

- $\alpha = 90^\circ$

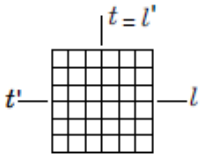

$\rho'_l = \rho_t$

$\rho'_t = \rho_l$

- $\alpha = 45^\circ$

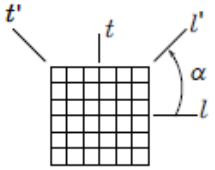

$\rho'_l = \frac{\sqrt{2}}{2}(\rho_l + \rho_t)$

$\rho'_t = \frac{\sqrt{2}}{2}(\rho_l + \rho_t)$